



HAL
open science

Design and Implementation of a CMOS imager with active column for SPR-based sensors

Arnoldo Salazar Soto

► **To cite this version:**

Arnoldo Salazar Soto. Design and Implementation of a CMOS imager with active column for SPR-based sensors. Micro and nanotechnologies/Microelectronics. Université de Grenoble; Instituto tecnológico y de estudios superiores (Monterrey, Mexique), 2013. English. NNT : 2013GRENT063 . tel-00932309v2

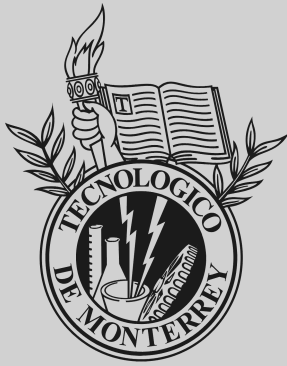
HAL Id: tel-00932309

<https://theses.hal.science/tel-00932309v2>

Submitted on 9 Sep 2014

HAL is a multi-disciplinary open access archive for the deposit and dissemination of scientific research documents, whether they are published or not. The documents may come from teaching and research institutions in France or abroad, or from public or private research centers.

L'archive ouverte pluridisciplinaire **HAL**, est destinée au dépôt et à la diffusion de documents scientifiques de niveau recherche, publiés ou non, émanant des établissements d'enseignement et de recherche français ou étrangers, des laboratoires publics ou privés.



UNIVERSITÉ DE GRENOBLE

THÈSE

Pour obtenir le grade de

DOCTEUR DE L'UNIVERSITÉ DE GRENOBLE

Spécialité : **Nano-Electronique et Nano-Technologies**

Arrêté ministériel : 7 août 2006

Et de :

DOCTEUR DE L'INSTITUTO TECNOLÓGICO Y DE ESTUDIOS SUPERIORES DE MONTERREY

Spécialité : **Technologies de l'Information et Communications**

Présentée par

Arnoldo SALAZAR

Thèse dirigée par **Olivier ROSSETTO** et **Sergio O. MARTÍNEZ-CHAPA**

préparée au sein du **Laboratoire de Physique Subatomique et de Cosmologie** dans **L'École Doctorale d'Electronique, Electrotechnique, Automatique et Traitement du Signal** et du **Département de Génie Electrique et Informatique** dans **L'Instituto Tecnológico y de Estudios Superiores de Monterrey**

Conception d'un Imageur CMOS à Colonne Active pour un Biocapteur Optique SPR

Thèse soutenue publiquement le **30 Octobre 2013**,
devant le jury composé de :

M. Salvador MIR

Directeur de recherche, Laboratoire TIMA, Président

M. Michel PAINDAVOINE

Chercheur et Professeur, Université de Bourgogne, Rapporteur

M. Heriberto MÁRQUEZ-BECERRA

Chercheur et Professeur, CICESE, Rapporteur

M. Sergio CAMACHO-LEÓN

Chercheur et Professeur, Tecnológico de Monterrey, Campus Monterrey ,
Examinateur

M. Olivier ROSSETTO

Maître de conférences à l'Université de Grenoble, LPSC, Directeur de Thèse

M. Sergio O. MARTÍNEZ-CHAPA

Chercheur et Professeur, Tecnológico de Monterrey, Campus Monterrey, Di-
recteur de Thèse



*A mis padres Arnoldo y Conchita por todo su apoyo a lo largo de mi carrera.
A la memoria de mis abuelas Esther y Guadalupe.*

Acknowledgements

First of all, I would like to express my sincere gratitude to both of my thesis advisors Dr. Sergio O. Martinez Chapa from the BioMEMS research group at Tecnologico de Monterrey in Monterrey, Mexico and Dr. Olivier Rossetto at the Laboratoire de Physique Subatomique et Cosmologie (LPSC) in Grenoble, France for their support and guidance in the realization of this thesis.

I want to thank the members of my thesis committee Dr. Salvador Mir, Dr. Michel Paindavoine, Dr. Sergio Camacho León and Dr. Heriberto Márquez for their valuable comments and suggestions in order to improve the quality of this work.

I would also like the members of the Electronic Services department at LPSC, Galdric Marcotte, Joel Bouvier, Nicolas Ponchant, Laurent Gallin-Martel and Jean-Pierre Scordilis for their help during my stay in Grenoble, France during the test card development.

Thanks also to the Tecnologico de Monterrey Optics Center for the facilities provided during the optical characterization of the CMOS imager.

Thanks to my friends at the BioMEMS research group at Tecnologico de Monterrey, Victor Hugo Perez, Manuel Rodriguez and Adrian Rendón.

Thanks to CONACYT for their economic support through the scholarship number 34234.

Finally I also thank my sister Ana Lucia, aunt Maria Esther, grandfather Francisco Soto and my whole family.

Conception d'un Imageur CMOS à Colonne Active pour un Biocapteur Optique SPR

par
Arnoldo Salazar Soto

Résumé

Cette thèse présente la conception et le développement d'un imageur CMOS pour biocapteurs optiques basé sur la résonance plasmonique de surface ou SPR (de l'anglais Surface Plasmon Resonance). Premièrement, les conditions optimales pour la résonance de plasmon dans une interface compatible avec un processus CMOS/Post-CMOS sont obtenus par modélisation avec le logiciel COMSOL. Deuxièmement, un imageur CMOS à Colonne Active de 32x32 pixels est réalisé en technologie CMOS 0,35 μm .

Dans une interface or-eau avec excitation du prisme et une longueur d'onde de 633 nm, on constate que pour des prismes avec des indices de réfraction de 1,55 et 1,46, le couplage SPR optimal se produit à des angles d'incidence de 68,45° et 79,05° avec les épaisseurs des couches d'or de 50 nm et 45 nm respectivement. Dans ces conditions, environ 99,19% et 99,99% de l'énergie de la lumière incidente sera transféré au plasmon de surface. Nous montrons aussi qu'un changement de 10^{-4} RIU dans l'indice de réfraction du milieu diélectrique, produit un changement de 0,01° dans l'angle de résonance de plasmonique, pour un schéma de modulation d'intensité lumineuse ce changement correspond à une variation de 0,08% dans l'énergie de la lumière réfléchie vu par le photodétecteur.

Pour l'imageur CMOS conçu, une photodiode caisson-N/substrat-P est choisie en raison de sa faible capacité de jonction, qui se traduit par un rendement quantique élevé et un gain de conversion élevé. Les simulations sur ordinateur avec Cadence et Silvaco donnent une capacité de jonction de 31 fF et un rendement quantique maximum de 82%. Le pixel de l'imageur est basé sur une configuration à trois transistors (3T) et a un facteur de remplissage de 61%. Le circuit de lecture utilise une technique de Colonne Active (ACS) pour réduire le bruit spatial (FPN) associés aux capteurs à pixels actifs traditionnels (APS). En outre pour compléter la réduction du bruit, un Double Echantillonnage Non-Corrélé (NCDS) et un Double Echantillonnage Delta (DDS) sont utilisés. Un montage optique expérimental est utilisé pour caractériser les performances de l'imageur, les résultats obtenus sont une gain de conversion de 7.3 V/e-, une photodiode avec une capacité de jonction de 21.9 fF, un bruit de lecture de 324,5 μV , équivalant approximativement à 45 électrons, et une gamme dynamique de 62,2 dB. Les avantages de l'ACS et NCDS-DDS sont observés dans les bas niveaux de FPN de pixel et colonne de 0,09% et 0,06% respectivement.

Le travail présenté dans cette thèse est une première étape vers le but de développer une plateforme de biocapteur entièrement intégrée basée sur SPR, incorporant la source de lumière, l'interface SPR, le canal microfluidique, les éléments optiques et l'imageur CMOS.

Diseño e implementación de un sensor de imagen CMOS de Columna Activa para biosensores basados en SPR

por

Arnoldo Salazar Soto

Resumen

Esta disertación presenta el diseño e implementación de un sensor de imagen CMOS para ser usado en un biosensor basado en resonancia de plasmones de superficie o SPR (de las siglas en inglés Surface Plasmon Resonance). En primer lugar, las condiciones óptimas para obtener resonancia de plasmones en una interface compatible con el proceso CMOS/Post-CMOS son obtenidas por medio del software COMSOL. En segundo lugar, un sensor de imagen CMOS de Columna Activa (CMOS-ACS) es implementado en tecnología estándar CMOS de 0.35 μm .

Para una interface de oro-agua, con excitación de prisma y longitud de onda de 633 nm, se encontró que para prismas con índices de refracción de 1.55 y 1.46, el acoplamiento óptimo ocurre a ángulos de incidencia de 68.45° y 79.05° , para espesores en la capa de oro de 50 nm y 45 nm respectivamente. Bajo estas condiciones, 99.19% y 99.99% de la energía incidente se transfiere al plasmon superficial. Adicionalmente, se encontró que para cambios de 10^{-4} RIU en el índice de refracción del medio dieléctrico se produce un cambio de 0.01° en el ángulo al que se produce SPR, que para un esquema de modulación de intensidad se traduce en un cambio de 0.08% en la intensidad de la luz reflejada al fotodetector.

Para el sensor de imagen CMOS, un fotodiodo de pozo-n/substrato-p es seleccionado debido a su capacitancia de unión mas baja, que se traduce en eficiencia cuántica y ganancia de conversión mas altas. Por medio de simulaciones computacionales hechas con Silvaco y Cadence se estima una capacitancia de unión de 31 fF y una eficiencia cuántica mxima de 82%. El pixel está basado en una arquitectura de tres transistores (3T) y tiene un factor de llenado de 61%. Los circuitos de lectura utilizan una configuración de Columna Activa (ACS) con el propósito de reducir el ruido espacial (FPN) asociado a los sensores de imagen activos tradicionales (APS). Adicionalmente, complementando los circuitos de reduccion de ruido se utiliza una lectura de Doble Muestreo No-Correlacionado (NCDS) y Muestreo Doble Delta (DDS). Un arreglo óptico experimental es usado para caracterizar el desempeño del sensor de imagen CMOS, obteniéndose una ganancia de conversión de 7.3 V/e-, una capacitancia de unión del fotodiodo de 21.9 fF, un ruido de lectura de 324.5 μV equivalente a 45 electrones, y un rango dinámico de 62.2 dB. Los beneficios de ACS y NCDS-DDS son observados en los bajos niveles de FPN de pixel y columna estimados en 0.09% y 0.06% respectivamente.

El trabajo presentado en esta tesis es un primer paso hacia el objetivo de desarrollar un biosensor basado en SPR totalmente integrado, incorporando fuente de luz, interface SPR, canales microfluídicos, elementos ópticos y sensor de imagen CMOS.

Design and Implementation of a CMOS Imager with Active Column for SPR-based Sensors

by

Arnoldo Salazar Soto

Abstract

This dissertation presents the design and implementation of a CMOS imager for use in integrated biosensors based on Surface Plasmon Resonance. First, the optimal conditions for plasmon resonance in a CMOS/Post-CMOS compatible interface are obtained by COMSOL modelling. Second, a 32×32 -pixel CMOS-Active Column Sensor (CMOS-ACS) is implemented in a $0.35 \mu\text{m}$ CMOS technology.

In a gold-water interface with prism excitation and wavelength of 633 nm, it is found that for prisms with refractive indexes of 1.55 and 1.46, the optimal plasmon coupling occurs at incidence angles of 68.45° and 79.05° and gold layer thicknesses of 50 nm and 45 nm, respectively. Under these conditions, approximately 99.19% and 99.99% of the incident light energy is transferred to the surface plasmon. It is also obtained that a change of 10^{-4} RIU in the refractive index of the dielectric medium, produces a change of 0.01° in the plasmon resonance angle, which under a light intensity modulation scheme represents a change of 0.08% in the reflected light's energy reaching the photodetector.

Concerning the CMOS imager, a n-well/p-substrate photodiode is selected as the photosensing element, due to its low junction capacitance, which results in high efficiency and high conversion gain. Computer simulations with Cadence and Silvaco produced a junction capacitance of 31 fF and a maximum quantum efficiency of 82%. The imager's pixel is based on a three-transistor (3T) configuration and shows a fill factor of 61%. The readout circuitry employs an Active Column Sensor (ACS) technique to reduce the Fixed Pattern Noise (FPN) associated with traditional Active Pixel Sensors (APS). Additionally, Non-Correlated Double Sampling (NCDS) and Delta Double Sampling (DDS) are used as noise reduction techniques. An experimental optical setup is used to characterize the performance of the imager, obtaining a conversion gain of $7.3 \mu\text{V}/e^-$, a photodiode junction capacitance of 21.9 fF, a read noise of $324.5 \mu\text{V}$, equivalent to $\sim 45e^-$, and a dynamic range of 62.2 dB. The benefits of ACS and NCDS-DDS are observed in the low pixel and column FPN of 0.09% and 0.06% respectively.

The work presented in this thesis is a first step towards the goal of developing a fully integrated SPR-biosensing platform incorporating light source, SPR interface, microfluidic channel, optical elements and CMOS imager.

List of Figures

1.1	Commercial SPR-based biosensing platform, Biacore T200,	3
2.1	Schematic of a SPR-biosensor	5
2.2	Schematic of SPR surface with bioreceptors immobilized using a few nanometre thick SAM and Ti/Cr prism adhesion layer.	7
2.3	Typical reflected light's profile at SPR interface.	8
2.4	Different modulation techniques in SPR biosensors. (a) wavelength, (b) angle and (c) intensity. ([12])	9
2.5	Schematic diagram of SPR imaging, The contrast of the SPR image is based on the reflectivity differences in the surface.	11
2.6	Transient SPR signal (sensorgram) of the interactions of the analyte with the spots on the surface.	11
2.7	Excitation of surface plasmons in Kretschmann's prism configuration. (a) diagram, (b) wave vector and material layers	13
2.8	Dispersion relation for surface plasmons. Curves I and II represent the SP dispersion for the interfaces prism-metal and metal-dielectric. Lines 1 and 2 are the dispersion relations for incident light with and without the prism respectively. Line 3 can be obtained by changing n_p [15]. . . .	14
3.1	Photons illuminating a reverse biased p-n junction [22].	17
3.2	I-V characteristic curve of a photodiode [23].	18
3.3	p-n junction, where x_j is the junction's position from the surface. The length of the depletion region in the n and p-type material is x_n and x_p respectively. The width of the depletion region is $W = x_n + x_p$. L_n and L_p are the diffusion lengths.	19
3.4	Responsivity and quantum efficiency of a Si photodiode	20
3.5	Cross-section view of a CMOS wafer.	22
3.6	CMOS photodiodes. (a) n-diff/p-sub, (b) n-well/p-sub, (c) p-diff/n-well/p-sub.	23
3.7	Photodiode voltage as a function of time for different illumination levels.	24
3.8	3T-Pixel configuration. (a) Schematic. (b) Timing	26
3.9	4T-Pixel configuration. (a) Schematic. (b) Timing	27
3.10	FPN on CIS. (a) Pixel-level, (b) Column-level, (c) Total-FPN. [31]	29
3.11	Correlated Double Sampling Principle (CDS) [29].	31
3.12	Non-Correlated Double Sampling (NCDS) principle [29].	31
3.13	Delta Double Sampling circuit [29].	32
3.14	Basic schematic Active Column Sensor	33

4.1	Excitation of surface plasmons in the Kretschmann configuration. (a) diagram, (b) wave vector and material layers implemented on COMSOL.	39
4.2	Reflectivity for different thickness of gold film layer, prism $n_p = 1.55$.	42
4.3	Reflectivity for different thickness of gold film layer, prism $n_p = 1.46$.	43
4.4	FWHM variation with gold layer thickness.	44
4.5	Minimum in reflectivity for different Au metal thickness.	44
4.6	Change in SPR angle and reflectivity for $\Delta n_d = 10^{-4}$ RIU at $\lambda = 633$ nm. $n_p = 1.55$.	45
4.7	Change in SPR angle and reflectivity for $\Delta n_d = 10^{-4}$ RIU at $\lambda = 633$ nm. $n_p = 1.46$.	46
4.8	Reflectivity change for different Ti layer thickness, Au 50 nm, $\lambda = 633$ nm. Prism $n_p = 1.55$.	47
4.9	Reflectivity change for different Ti layer thickness, Au 45 nm, $\lambda = 633$ nm. Prism $n_p = 1.46$.	48
5.1	Block diagram of CMOS imager with ACS and test card.	51
5.2	SILVACO structure of CMOS photodiodes. (a) n-diff/p-sub, (b) n-well/p-sub.	52
5.3	Estimated dark current density for n-diff/p-sub and n-well/p-sub.	54
5.4	Simulated currents, n-diff/p-sub photodiode.	55
5.5	Simulated currents, n-well/p-sub photodiode.	56
5.6	Quantum efficiency. (a) n-diff/p-sub; (b) n-well/p-sub.	56
5.7	Cadence electrical simulation results. N-well/p-sub (solid) and n-diff/p-sub (dashed) junction capacitance vs. applied voltage.	57
5.8	Virtuoso Cadence Pixel's layouts. The extracted view (right) gives the photodiode's area and perimeter (a) n-diff/p-sub, (b) n-well/p-sub.	58
5.9	Schematic of Active Column Sensor circuit.	59
5.10	ACS simulated frequency response Active Column Sensor.	63
5.11	ACS simulated Input Common Mode Range (ICMR).	64
5.12	ACS simulated positive and negative slew rate.	64
5.13	ACS simulated power supply rejection ratio.	65
5.14	ACS simulated common mode rejection ratio.	65
5.15	Virtuoso cadence ACS circuit Layout.	66
5.16	Simplified electrical model of a photodiode.	67
5.17	Pixel's output for APS and ACS. Integration time 30 ms. $V_{PD} - V_{outACS} = 1.9mV$ and $V_{PD} - V_{outACS} = 0.69V \approx V_{TH}$.	67
5.18	Difference between photodiode voltage and Pixel ACS output. 500 sample Monte Carlo simulation.	68
5.19	Simple CMOS sample and hold circuit.	69
5.20	Sample-and-Hold circuit using a CMOS transmission gate.	69
5.21	Schematic of NCDS-DDS Column circuit.	70
5.22	Virtuoso Cadence Layout of NCDS-DDS Column circuit.	70
5.23	Schematic of CMOS-ACS shared output stage circuit.	71
5.24	Virtuoso Cadence layout of global output stage.	71
5.25	Proposed CMOS-ACS timing sequence diagram.	72

5.26	Variation of output with and without NCDS for a constant photocurrent. 500 sample Monte Carlo simulation	75
5.27	Schematic of output amplifiers (Reset and signal voltages)	76
5.28	Simulated frequency response of output op-amps	77
5.29	Simulated Input Common Mode Range (ICMR) of output op-amps	77
5.30	Simulated positive and negative slew rate of output op-amps	78
5.31	Simulated power supply rejection ratio of output op-amps	78
5.32	Simulated common mode rejection ratio of output op-amps	79
5.33	Simulated 4×4 pixel array	80
5.34	Differential output dependency on the photocurrent.	81
5.35	Schematic of CMOS-ACS with NCDS-DDS	82
5.36	CMOS-ACS chip. AMS 0.35μm CMOS 3.3V. Total chip area 2 mm × 2.25 mm	83
6.1	Test Card Circuit	85
6.2	Test Card block diagram	85
6.3	FIFO memory address format	87
6.4	Optical test setup	88
6.5	Conversion gain measurement. Slope of fit $7.3 \mu\text{V}/e^-$	89
6.6	Measurement of dark voltages for different integration times.	90
6.7	Measurement of sensitivity of CMOS-ACS.	91
6.8	Output Frame for dark illumination conditions. Single signal output and differential output with NCDS	93
6.9	Output Frame for 50% of full-well saturation illumination conditions. Single signal output and differential output with NCDS	93
6.10	Histogram of measured single pixel output under dark conditions and short integration time.	94
6.11	Measured SNR variation with differential output	95
7.1	Proposed biosensing platform to perform SPR angular modulation.	100
7.2	Proposed biosensing platform to perform SPR imaging.	101
A.1	Geometry of planar waveguide	109
B.1	32×32 CMOS-ACS pinout.	113

List of Tables

3.1	Examples of CMOS Image Sensors used in optical biosensing applications.	34
4.1	SPR interface and excitation prism optical characteristics.	40
4.2	Minimum reflectivity and SPR angles with prism $n_p = 1.55$.	41
4.3	Minimum reflectivity and SPR angles with prism $n_p = 1.46$.	41
4.4	Minimum reflectivity and SPR angles for different refractive index in the dielectric medium. Prisms of $n_p = 1.55$ and $n_p = 1.46$.	45
4.5	Minimum reflectivity and SPR angles for different titanium adhesion layers for $n_p = 1.55$ (Au thickness 50 nm) and $n_p = 1.46$ (Au thickness 45 nm).	47
5.1	Recombination rates and currents for n-diff/p-sub and n-well/p-sub photodiodes	53
5.2	Diffusion currents at T=300 K for n-diff/p-sub and n-well/p-sub photodiodes	54
5.3	Extracted view geometrical characteristics and junction capacitances for n-diff/p-sub and n-well/p-sub photodiodes.	58
5.4	Specifications of the ACS amplifier	60
5.5	First approximation ACS amplifier	62
5.6	Dependence of op-amp characteristics	62
5.7	Final ACS op-amp parameters	63
5.8	Final ACS op-amp performance characteristics	66
5.9	Specifications of the Output amplifier	76
5.10	Output op-amp transistor ratios	76
5.11	Final ACS op-amp performance characteristics	79
6.1	Measured CMOS-ACS performance characteristics	96
B.1	CMOS-ACS pin description	114

Contents

Résumé	iii
Resumen	iv
Abstract	v
List of Figures	viii
List of Tables	ix
1 Introduction	1
1.1 Label-free optical biosensors	1
1.2 CMOS Image Sensors	2
1.3 Motivation	2
1.4 Thesis organization	3
2 Theoretical Background SPR Biosensors	4
2.1 Components of a SPR biosensor	4
2.1.1 SPR Optics	5
2.1.2 Sample Handling System	5
2.1.3 Surface Plasmon Resonance Interface	6
2.1.4 Signal Processing for SPR Sensors	6
2.2 SPR based biosensors	7
2.2.1 Surface Plasmon Resonance Imaging (SPRi)	10
2.3 Surface Plasmon Resonance theory	11
2.3.1 Prism excitation of SPR	12
2.4 Conclusions	14
3 Theoretical Background on CMOS Imagers	16
3.1 Basics of photodetection	16
3.1.1 P-N photodiode	17
3.1.2 Responsivity and quantum efficiency on Photodiodes	19
3.1.3 Noise in photodiodes	20
3.1.4 Dark current on photodiodes	21
3.2 CMOS photodiodes	21
3.2.1 Charge collection and transfer	23
3.3 Pixel configurations	24
3.3.1 Active Pixel Sensors	25
3.3.1.1 3T-APS	25
3.3.1.2 4T-APS	26
3.3.1.3 Other Pixels configurations	27
3.4 Noise on CMOS imagers	28
3.5 Readout Circuits	29
3.5.1 Addressing	29
3.5.2 Source Follower	30
3.5.3 Noise reduction circuits	30
3.5.3.1 Correlated Double Sampling (CDS)	30

3.5.3.2	Non-Correlated Double Sampling (NCDS)	31
3.5.3.3	Delta Double Sampling (DDS)	32
3.5.4	Output Stage	32
3.6	Active Column Sensor readout	33
3.7	State-of-the-art applications of CMOS Imagers in Biosensing	34
3.8	Conclusions	36
4	Determination of optimal SPR conditions	38
4.1	COMSOL simulation	38
4.1.1	Simulated geometry	38
4.1.2	Materials optical characteristics	39
4.2	Metal layer thickness	40
4.3	Sensitivity	44
4.4	Titanium adhesion layer	46
4.5	Conclusions	48
5	CMOS Imager for SPR-Biosensors	50
5.1	CMOS Image Sensor Prototype	50
5.2	CMOS Photodiode modeling	51
5.2.1	Dark current estimation	53
5.2.2	Spectral response estimation	55
5.2.3	Quantum efficiency	56
5.2.4	Photodiode's junction capacitance	57
5.3	Active Column Sensor	59
5.3.1	APS vs ACS	67
5.4	Column Readout circuits	68
5.4.1	Output amplifier	75
5.4.2	CMOS-ACS 4x4 cadence simulation	80
5.5	Complete CMOS-ACS chip	81
5.6	Conclusions	83
6	Characterization of CMOS-ACS	84
6.1	Introduction	84
6.2	Test Card	84
6.2.1	CMOS-ACS digital control signals	86
6.2.2	Analog to Digital conversion and 2048x16 FIFO	86
6.2.3	Interface with NI-LabView	87
6.3	CMOS-ACS prototype characterization	87
6.3.1	Conversion Gain	88
6.3.2	Dark current	89
6.3.3	Sensitivity	90
6.3.4	Fixed Pattern Noise	91
6.3.5	Read Noise	93
6.3.6	Dynamic range	94
6.3.7	Signal-to-noise-ratio	95
6.3.8	CMOS-ACS performance characteristics summary	95
6.4	CMOS-ACS in SPR biosensing platform	96
6.5	Conclusions	97
7	Conclusions	98
7.1	Future work	99
7.1.1	Experimental set-up	99
7.1.2	Improvement to the CMOS-Imager	101
	Bibliography	107
A	Appendix A	108
A.1	Analysis of propagation of surface plasmons with Maxwell's equations	108

B Appendix B	112
B.1 32x32 CMOS-ACS pinout	113
Vita	115

Chapter 1

Introduction

1.1 Label-free optical biosensors

The diagnosis of diseases, discovery of new medicaments, drug delivery systems and detection of pollutants involve the analysis of biological agents such as DNA, proteins, antibodies, enzymes and viruses. These analyses are performed by devices known as *biosensors*. According to their transduction principle, biosensors can be classified as mechanical, chemical, electrical and optical. Optical biosensors in turn can be divided into *labeled* and *label-free*.

Labeled biosensors are based on immobilizing probes or bioreceptors to a substrate and the attachment of fluorescent tags to the analyte (substance under analysis). During the probe-analyte interaction, the fluorescent labels are stimulated and the light emitted provides information about these interactions. This method is widely used due to its high sensitivity, however it has three main disadvantages: (1) the tags can interfere with the analyte binding, (2) the real-time monitoring of the binding interaction is not possible, (3) the extra step involved in labeling is time consuming and requires specialized personnel which increases costs. Label-free biodetection methods aim to solve some of the problems of labeled biodetection.

Label-free biosensing techniques depend on the measurement, without external labelling, of an inherent property of the system under examination, such as mass, dielectric constant, or refraction index [1]. In this kind of sensor, a probe is attached to a substrate and a surface property of the system recorded as reference. Then the target molecules are introduced, and the binding interactions between the surface's probes and the analyte produce changes in the property under observation. Avoiding the labelling process represents costs and time savings. Additionally, this technique avoids damaging the samples by not introducing additional external agents to the system.

Surface Plasmon Resonance (SPR) biosensors are label-free optical biosensors where biospecific interactions are detected in real time by monitoring changes of the refractive index in a dielectric medium immediate to a functionalized metallic surface [2–4]. Since the conditions at which SPR occurs are very specific, slight changes in them due

to biological interactions can be correlated to information such as concentration levels and binding kinetic's parameters. SPR has been applied to the detection of bacteria, viruses, single nucleotide polymorphisms, gene-related diseases and food toxins among others [5–7].

1.2 CMOS Image Sensors

Optical biosensors include a detection stage where a property of the light (intensity, polarization, wavelength) is monitored and processed. For SPR-based biosensors, Charge-Coupled Devices (CCDs) have been the preferred photodetector due to their low noise and high sensitivity, commonly required in biosensing applications. However, there is an increased interest in the use of CMOS Image Sensors (CIS), where recent advances have shorten the gap in terms of noise and sensitivity performance with respect to CCDs [8, 9]. Furthermore, CMOS imagers have particular advantages such as: lower bias voltages than CCDs, which is especially important if developing portable devices, where low power consumption is a concern; windowing capabilities, with the ability to select a particular region of interest in the photodetector array; and higher processing speed [10].

In addition, perhaps the main advantage of CMOS imagers is their compatibility with the standard CMOS fabrication process and thus a better capacity for integration with signal processing and application-specific circuitry. This characteristics make CMOS imagers an attractive and viable option in the development of *Lab-on-a-chip* (LOC) devices, where the functions performed in conventional laboratory equipment are integrated in a single chip. The design and fabrication of LOCs takes on microfabrication techniques based on the CMOS process, where besides electronic circuitry it also incorporates mechanical nanostructures, biological, microfluidic and microoptical elements [11].

1.3 Motivation

Commercial SPR biosensing instruments, such as the one shown on figure 1.1 are used in applications like the characterization of antibody–antigen interactions. These devices can range in price from \$30,000.00 to \$300,000.00, and have sizes of a desktop computer.

The main motivation of this work is contributing toward the development of a miniaturized and fully integrated CMOS-based, SPR biosensing platform taking advantage of the great potential that application-specific CMOS circuitry represents in the development of LOCs devices. This work is divided in two parts. First, the optimal conditions for plasmon resonance in a CMOS/Post-CMOS compatible interface are obtained by COMSOL modeling. Second, a 32×32 -pixel CMOS-Active Column Sensor (CMOS-ACS) imager is implemented in a $0.35 \mu\text{m}$ technology and including noise reduction features.



Figure 1.1: Commercial SPR-based biosensing platform, Biacore T200, .

The results obtained from COMSOL modeling establish some design requirements for the CMOS imager and are also required for the eventual implementation of the biosensing platform, where by knowing beforehand the parameters needed to obtain the better performance for the SPR-platform, the sensitivity of the devices is expected to increase. The imager is based on an Active Column Sensor (ACS) configuration that has a true unity gain amplifier and noise reduction circuitry. These features are aimed at improving the quality of the output signal, considering that in biosensing applications often the illumination levels are low, due to the need to work with low power optical excitation in order to not damage the biological samples. Furthermore, the implemented CMOS imager is controlled through external signals provided by a FPGA, giving the flexibility to optimize the integration time and readout of the output signal, and providing the capability to select any sub-window within the photosensing array.

1.4 Thesis organization

The rest of this document is organized as follows: Chapter 2 presents the theoretical background on the Surface Plasmon Resonance phenomenon, focusing on the application of this phenomenon to biosensors. Chapter 3 shows the theoretical background on CMOS image sensors, presenting the basics of photodetection, the CMOS photodiodes and the main pixel architectures. Chapter 4 presents the modeling of a CMOS/Post-CMOS interface in COMSOL, where the optimal coupling conditions are obtained. Chapter 5 presents the design of the 32×32 pixel imager in a $0.35\mu\text{m}$ CMOS technology. Chapter 6 shows the experimental characterization of the imager. Finally, chapter 7 presents the conclusion and future work.

Chapter 2

Theoretical Background on Surface Plasmon Resonance Biosensors

In this chapter, the fundamental concepts of SPR-biosensors are described. The parts that comprise a SPR-based biosensors are presented in sections 2.1. The principle of operation is then described on section 2.2, where the metrics that describe its performance are also introduced. In order to have a better understanding of the phenomenon, in section 2.3 the electromagnetic basis of SPR are described, focusing on the most commonly method of plasmon excitation, Kretschmann's Configuration, based on the use of prisms.

2.1 Components of a SPR biosensor

A surface plasmon can be defined as a charge density wave occurring at an interface where free electrons are present, usually a metal-dielectric. These waves will exist at this interface with the electric field decaying exponentially in both media. The use of SPR in biodetection has been widely reported and continues to be subject of research in the field of biomedics [2-4].

Figure 2.1 show the basic components of a SPR-biosensors, which are described in the following sections.

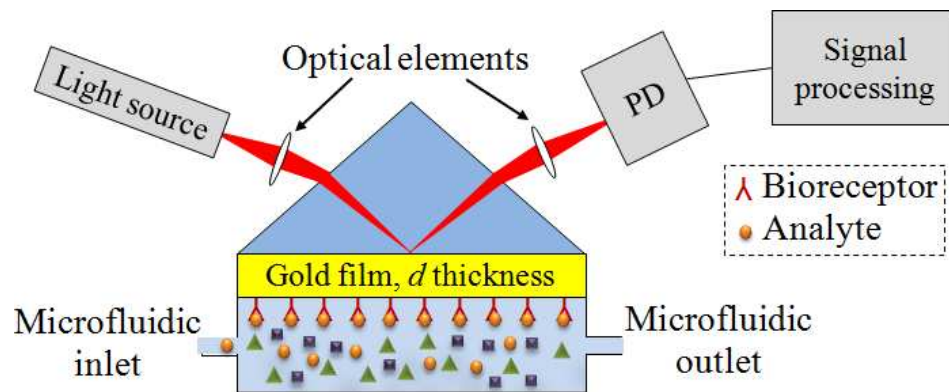


Figure 2.1: Schematic of a SPR-biosensor

2.1.1 SPR Optics

In general, the optical system of SPR biosensors is composed of the following elements [12]:

- *Light source*: Provides the excitation source to the system. If using wavelength modulation a polychromatic light source is required. On the other hand, a monochromatic light source, such as a laser, is used for both angle and intensity modulation, as it will be described in next section.
- *Photodetector*: This device is used to monitor the reflected light from the SPR interface. Depending of the light property being detected this device can be a spectrometer, photodiode array, CCD or CMOS Image Sensor among others.
- *Excitation optics*: Its function is to couple the incident light with the surface plasmon in order to achieve resonance. Some methods to achieve this excitation are: prism, gratings and waveguides.
- *Other optical elements*: Elements such as lenses, mirrors, objectives, polarizers, filters etc. are included in this category. Their purpose is to direct, focus, collimate, filter or change the polarization state of the light, according to the system's needs.

2.1.2 Sample Handling System

This sub-system of the SPR biosensing platform has the task of manipulating the liquid solution in the biosensor. Focusing on LOCs, in recent years microfluidic systems have taken an important role as a research subject. Microfluidic devices are based on the manipulation of quantities of liquids in the nano/micro range, representing important advantages such as: low reactive consumption, thus avoiding the collection and use of larger quantities of samples; due to the short distances travelled in the microscopic

channels, the response time of this systems is greatly reduced; the non-turbulent flow inherent to this systems will facilitate the sample manipulation [13]. The use of microfluidics in SPR biosensors has been previously reported as described in [14], where by using soft lithography techniques an array of addressable microfluidic chambers are bonded to a gold patterned glass slide, intended for high-throughput SPRi-based detection.

2.1.3 Surface Plasmon Resonance Interface

The interface is the core of the SPR-sensor since it is where the surface plasmon wave propagates. With the dielectric medium represented by the solution introduced through the microfluidic channels, the biggest challenge in this area is the immobilization of the ligands or probes to the metal's surface. A successful direct, label-free measurement of specific binding events is facilitated by the best possible activity of the immobilized bioreceptor. Special care must be taken in order to keep all non-specific binding interactions in the surface as low as possible, in order to prevent irrelevant signals to interfere with the interpretation of the specific interaction. Since SPR detection can be applied to a great variety of analytical applications, there are an equally large number of methods for immobilization, with no technique being prevalent and selected according to the particular needs of the application [12].

Regarding the metal surface, even when silver results in a better SPR sensitivity, gold is the prevalent material used since chemically is more inert than silver, thus better suitable to serve as a substrate where the chemical reactions take place [15].

For the surface immobilization of biorecognition elements on a gold surface, self-assembled monolayers (SAMs) of alkanethiolates are often used [15]. The purpose of this layer is to minimize the non-specific adsorption and introduce reactive groups for specific immobilization. Monolayer formation is driven by a strong coordination of sulphur with the metal, accompanied by Van der Waals interactive forces between the alkyl chains. With a sufficient chain length, the resulting monolayer forms a densely packed and very stable structure that is oriented more or less along the normal direction to the metal surface. SAMs are relatively easy to introduce and they are fabricated from commercially available substances. In addition, if using prism SPR excitation, the deposition of gold films over the glass prism includes a thin adhesion layer of either titanium or chromium, in order to prevent the gold from being removed during manipulation [16]. Figure 2.2 shows a scheme of the basic layers involved in the construction of a SPR-interface.

2.1.4 Signal Processing for SPR Sensors

Once the signal is translated by the photodetector, it must be processed to obtain useful results. For wavelength or angular modulation, the light reflected from the metal surface is dispersed over the detector array, illuminating each pixel with light of a slightly different intensity according to the profile produced by the presence or not of plasmon resonance. From here, the signal is digitized periodically, by continuously acquiring frames. The first step in the data processing stage is to average the incident

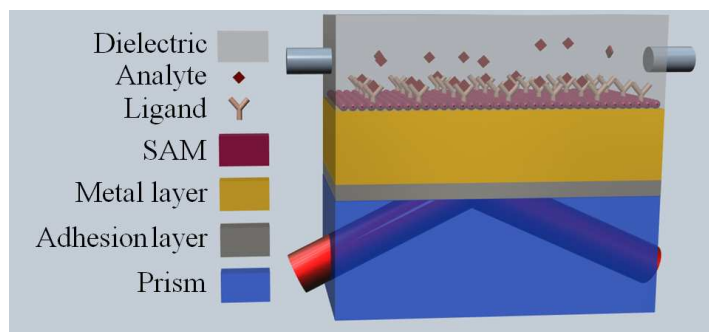


Figure 2.2: Schematic of SPR surface with bioreceptors immobilized using a few nanometre thick SAM and Ti/Cr prism adhesion layer.

intensities and normalize them, the averaging can be done in the time domain in a single detector or in the space domain by using a 2D detector array. Normalization involves the subtraction of the dark level. Then the resulting signal is divided by a reference signal to compensate for uneven distribution of illumination. It is common to use a TE-polarized light as reference [17], since as it will be discussed later this type of polarization doesn't produce SPR. From the resulting data, the next step is to obtain the position of the SPR angle. A number of algorithms are used with this purpose, with the technique known as centroid being the most commonly used [12], where the center of mass of a portion of the SPR curve that falls below certain intensity level is calculated. In SPR sensors with intensity modulation, the intensity value can be detected by a 2D detector such as a CCD or CMOS imager, and the resulting set of intensities are averaged in time and space, leading directly to the sensor output. The technique known as SPR imaging, based on intensity modulation, uses this type of data processing.

2.2 SPR based biosensors

SPR biosensors are based on the fact that the conditions for resonance are very well defined and depend mainly on the optical properties of the materials (metal-dielectric interface) and the characteristics of the light source. This strong dependency causes that even slight changes in the conditions surrounding the SPR-interface, produce a change in the conditions at which resonance is encountered.

The basic principle under which this type of biosensor operate is as follows: suppose that biological probes or receptors (protein, enzymes, DNA, etc.) are immobilized to a metal surface in contact with a dielectric material (figure 2.2) and the initial conditions, such as incident light's wavelength and angle at which SPR occurs are recorded. Then suppose that a solution containing the molecule under analysis (ligand) is introduced to the system, causing molecular binding interactions to take place between corresponding receptors-ligands, according to their binding affinity. This process in turn alters the surface's refractive index immediate to the metal-dielectric interface. The change in the surrounding conditions will finally be observed as a change in the position at which SPR

takes place. The high sensitivity of SPR to changes in the refractive index allows to correlate the change in angle, wavelength or intensity at which SPR is produced with sample concentration levels and binding kinetics measurements [12, 18]. The fact that SPR-biosensors are based on these binding interactions is often emphasized by referring to these biosensors as *SPR affinity biosensors*.

At the optical photodetection stage, the presence of SPR is observed as a decrease in the reflectivity curve incident on the photodetector, as seen on figure 2.3. Taking the solid line as the initial state (before sample introduction) most of the light incident at the interface is reflected to the photodetector. At position x_1 , the SPR conditions are met and plasmon resonance achieved causing the wave's energy to now propagate through the metal-dielectric interface in the form of an evanescent wave known as surface plasmon, this process is explained with more detail in section 2.3. Then, once the sample solution is put in contact with the SPR-interface, binding interactions will cause the position of the resonance condition to change to x_2 , as seen on figure 2.3.

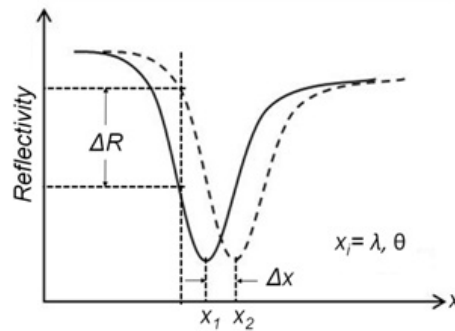


Figure 2.3: Typical reflected light's profile at SPR interface.

Depending on the property of the light being monitored, SPR biosensors can be classified by the type of modulation they use [12], as shown on figure 2.4:

- *Wavelength modulation*: SPR-biosensors based on this method work by keeping the light incident angle constant, and observing the change in wavelength at which SPR is experienced as the refractive index at the interface changes. The incident field in this case is collimated beam of polychromatic light, and the excitation of surface plasmons observed with a spectrometer in order to separate the wavelength components of the reflected light (figure 2.4a).
- *Angular modulation*: Monochromatic light is used as the excitation source. An incidence angle sweep is made and the decrease in the reflected light observed in the photodetector at each angle. Then, as binding interactions take place a change in the SPR angle will be observed (figure 2.4b).
- *Intensity modulation*: This type of SPR sensor is based on measuring the strength of the coupling between the light and the surface plasmon by observing the change in the light intensity as the refractive index changes. This analysis is performed at a fixed incidence angle and wavelength (figure 2.4c). For example, SPR imaging

(SPRi) is a technique based on intensity modulation that expands on normal SPR by providing spatial information over the entire biochip and will be explained in more detail later.

- *Phase modulation*: The phase shift of the light wave coupled to the surface plasmon is measured at a single angle of incidence and wavelength. This method is less used than the previous three modulation techniques.

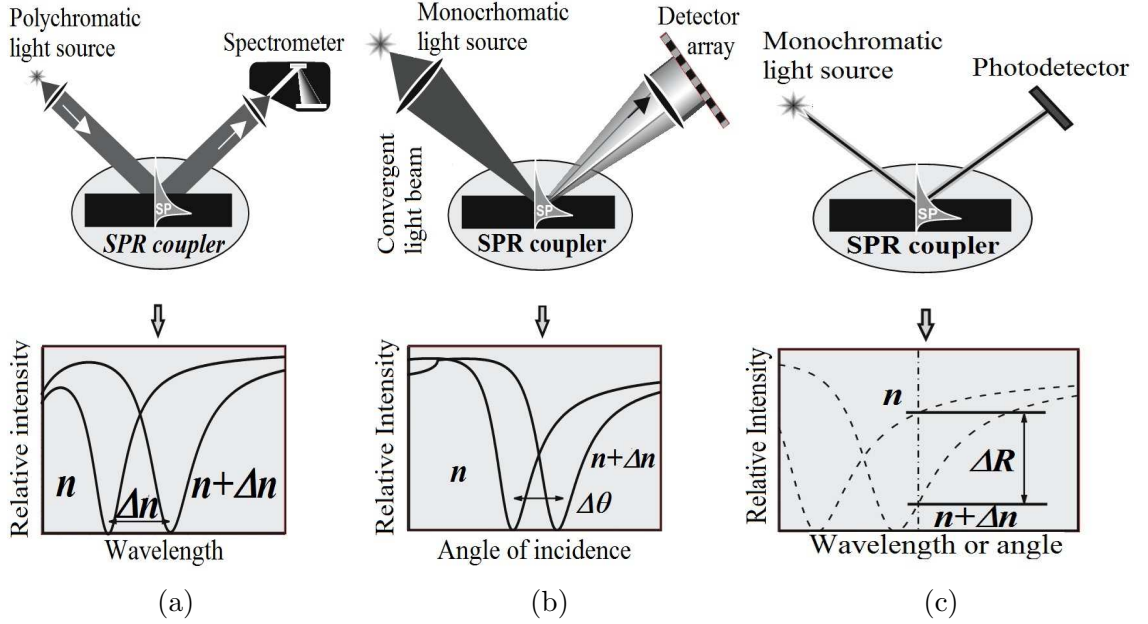


Figure 2.4: Different modulation techniques in SPR biosensors. (a) wavelength, (b) angle and (c) intensity. ([12])

The performance of the SPR biosensor is determined by its sensitivity and resolution. The sensitivity is the ratio of change in sensor output (Y) to change in the refractive index (n_d) [12].

$$S_n = \frac{\partial Y}{\partial n_d} \quad (2.1)$$

In turn, equation 2.1 is composed of two main contributing factors: The sensitivity of the output to the effective refractive index change (S_1) and the effective refractive index change caused by a change in the dielectric refractive index (S_2).

$$S_n = S_1 S_2 = \frac{\partial Y}{\partial n_{eff}} \frac{\partial n_{eff}}{\partial n_d}. \quad (2.2)$$

The term S_1 depends on the modulation scheme selected and is usually known as the instrumental sensitivity of the SPR-sensor.

A second important performance characteristic of the SPR biosensor is the resolution, defined as the smallest change in the refractive index that produces a detectable change in the sensor output. It depends on noise level at the output, which has its origin in the optical system and readout electronics. On the optical system the main source of noise are: fluctuations in intensity emitted by the light source, shot noise due to the statistical properties of the light and the noise in the light conversion at the photodetector. At the light source, this noise is represented by $\sigma_L = I \cdot \sigma_L^{rel}$, proportional to the intensity (I) and σ_L^{rel} represent the standard deviation independent of the intensity. The shot noise, $\sigma_S = \sqrt{I} \cdot \sigma_S^{rel}$, is due to the random arrival of photons at the photodetector and obeys Poisson statistics, its standard deviation is proportional to the square root of the light intensity, where σ_S^{rel} is the standard deviation independent of the intensity. The detector's noise is represented by σ_D , and the total noise of the measured light will be given by [12]:

$$\sigma_I(I) = \sqrt{\sigma_L^2 + \sigma_S^2 + \sigma_D^2}, \quad (2.3)$$

2.2.1 Surface Plasmon Resonance Imaging (SPRi)

SPRi is an example of the use of intensity modulation, this technique has two main advances over conventional SPR: 1) the ability to visualise the entire biochip surface in real time; and 2) being able to monitor hundreds of molecular interactions continuously. This is done by immobilizing multiple receptors on the surface and monitoring the kinetic parameters of biospecific interactions simultaneously [19]. In an array such as the one on figure 2.5, less light is reflected at an angle of incidence θ_i for the points in the surface where the probes are immobilized and more light is reflected for the areas of the gold surface free of bioreceptors, thus the lighter background on the detail in the figure [19]. Furthermore, an additional shift in the SPR curve is experienced when binding interactions occur between analytes and ligands in certain spots on the metal surface.

In general, SPRi is done by expanding and collimating the incident beam to cover the region of interest (ROI) on the surface, the measurements are done by selecting and fixing the incident angle where the surface plasmon coupling is stronger for that particular ROI, and a reference image is taken. As the analytes begin to be introduced to the system, binding interactions are monitored in real-time, this information is displayed on plots known as sensograms, where the reflectivity changes (or wavelength or angle) due to these binding interactions are plotted against time, according to the image taken by the photodetector array (figure 2.6). In a sensorgram the reflectivity is at a base level, then when the sample begins to be introduced, the association stage starts as bindings interactions take place at a certain rate, changing the reflectivity level at which plasmon resonance occurs, at some point all the ligand-analyte reactions will finish reaching a constant level. Finally, the system flushes and disassociation and regeneration will take the system to the initial stage to commence the study again [19].

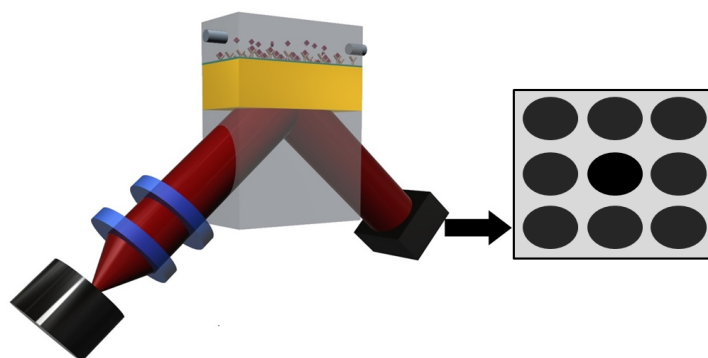


Figure 2.5: Schematic diagram of SPR imaging, The contrast of the SPR image is based on the reflectivity differences in the surface.

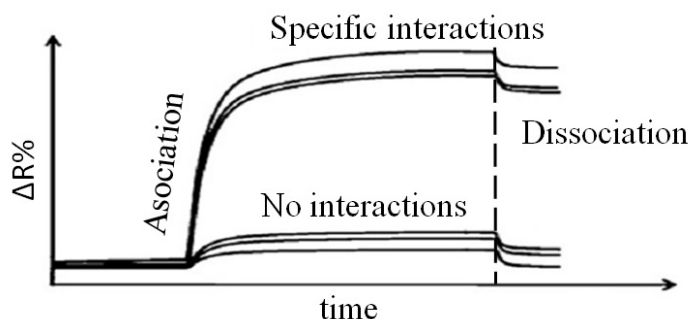


Figure 2.6: Transient SPR signal (sensorgram) of the interactions of the analyte with the spots on the surface.

2.3 Surface Plasmon Resonance theory

A complete understanding of SPR requires an analysis that incorporates quantum mechanics, however a good explanation of this phenomenon can be done through an analysis based on the interaction between electromagnetic fields at conducting surfaces. The propagation of surface plasmons in a metal-dielectric interface is described in terms of Maxwell's equations by Maier [20] and presented in appendix A. From this analysis it is found that for SPR to take place, and the plasmon to propagate along the interface in the form of an evanescent wave, it is necessary for the incident field to be a TM-wave or p-polarization. In this type of polarization the electric field is parallel to the incidence plane, and thus the magnetic field perpendicular to it, as illustrated in figure 2.7b where only the components E_x , E_y and H_z are not zero. Furthermore, the continuity conditions establish that in order for the evanescent waves to exist, it is required for the two materials in the interface to have dielectric functions of opposite signs. A metal-dielectric interface satisfy this condition, since metals have a large negative real part of its dielectric function, while for dielectric materials this property is positive.

Solving the wave equation for TM-waves incident at a metal-dielectric interface

leads to the fundamental SPR equation, relating the material's properties with the frequency/wavelength of the light (dispersion relation):

$$k_{SPR} = k_0 \sqrt{\frac{\varepsilon_d \varepsilon_m}{\varepsilon_d + \varepsilon_m}} = k_0 (n_{eff} - i\gamma_i). \quad (2.4)$$

Where k_{SPR} is the plasmon's surface propagation constant along the interface (x -axis), k_0 is the wave number given by $k_0 = 2\pi/\lambda$, ε_d is the permittivity of the dielectric medium and ε_m the permittivity of the metal, n_{eff} is the effective refractive index and γ_i the plasmon's attenuation coefficient as defined by [21].

2.3.1 Prism excitation of SPR

Incident light cannot be directly coupled with the surface plasmon to produce resonance, it is necessary to match the propagation constants of the incident light and the surface plasmon through an excitation scheme. The most common excitation method is Kretschmann's configuration, which makes uses of a prism as shown on figure 2.7. Based on attenuated total reflection (ATR), its effect can be explained observing figure 2.7b and figure 2.8. Without the prism, the dispersion relation of the incident light, propagating through air, is represented by line 1), and given by the x -component of the wave vector $k_{ix} = k_0 \sin \theta_i$. On the other hand, for the metal-dielectric interface the dispersion relation is given by equation 2.4 and graphically represented by line I). As observed, these lines don't intersect at any point, thus the incident light at no point is able to excite surface plasmon resonance. When a prism is added, the wave will now arrive at the interface propagating through a prism, this is represented by line 2), and given by $k_{ix} = k_0 n_p \sin \theta_i$ where n_p is the refractive index of the prism. Finally, the dispersion relation of the prism-metal interface is represented by line II), where part of the incident light is reflected at an angle given by Snell's law and part will propagate in the metal in the form of an evanescent wave, thus the wave will decay exponentially in a direction perpendicular to the interface. If the metal is thin enough, usually < 100 nm [12], the wave will reach the metal-dielectric interface. As seen in figure 2.8, line 2) intersects line I), at this point the x -component of the incident wave vector and the surface plasmon match, thus arriving at the resonance condition. The propagation constant of the incident light in the prism can be modified by changing the refractive index of the prism, and any light with a dispersion relation falling between lines 1) and line 2), such as line 3), has the possibility of exciting SPR. Thus, in order for SPR to be excited with Kretschmann's configuration the following relation must be meet:

$$k_{ix} = k_{SPR} = \frac{2\pi n_p}{\lambda} \sin \theta_i = \Re \left(k_0 \sqrt{\frac{\varepsilon_1 \varepsilon_2}{\varepsilon_1 + \varepsilon_2}} \right) \quad (2.5)$$

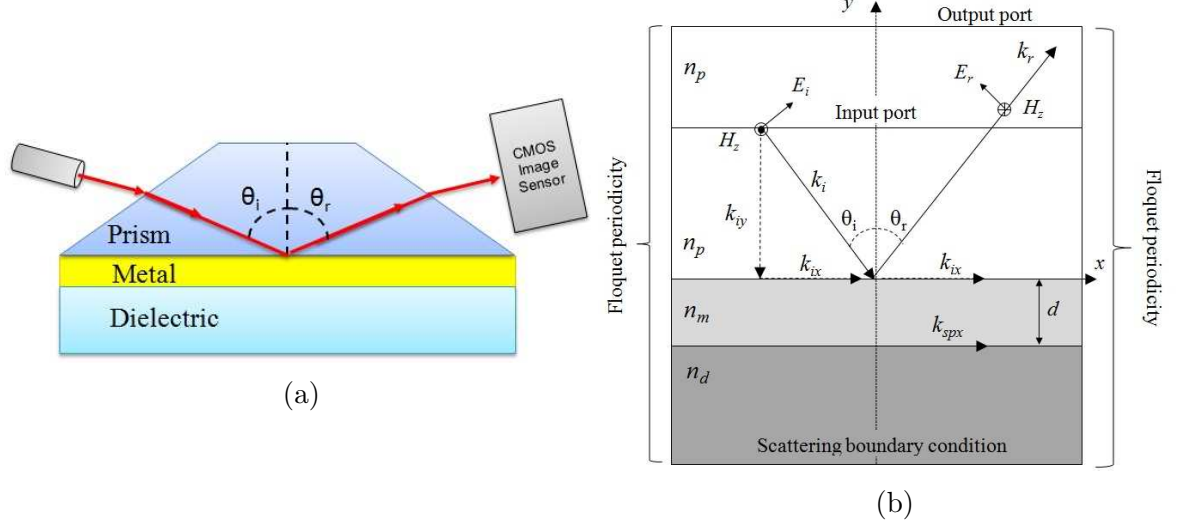


Figure 2.7: Excitation of surface plasmons in Kretschmann's prism configuration. (a) diagram, (b) wave vector and material layers

In addition, since $k_0 = 2\pi/\lambda$ the curve can also be modified by changing the wavelength λ . The amplitude of the reflected light, A_r , arriving at the photodetector can be estimated using Fresnel's equations for a three layer system [12].

$$A_r = r_{p,m,d}A_I = |r_{p,m,d}| \exp(j\phi)A_I, \quad (2.6)$$

where A_I is the amplitude of the incident light, ϕ is the phase shift, and $r_{p,m,d}$ is the reflection coefficient given by:

$$r_{p,m,d} = \frac{r_{p,m} + r_{m,d} \exp(j2k_{y,m}d)}{1 + r_{p,m}r_{m,d} \exp(j2k_{y,m}d)} \quad (2.7)$$

where,

$$r_{p,m} = \frac{k_{y,p}\varepsilon_m - k_{y,m}\varepsilon_p}{k_{y,p}\varepsilon_m + k_{y,m}\varepsilon_p}, \quad (2.8a)$$

$$r_{m,d} = \frac{k_{y,m}\varepsilon_d - k_{y,d}\varepsilon_m}{k_{y,m}\varepsilon_d + k_{y,d}\varepsilon_m}, \quad (2.8b)$$

and,

$$k_{y,p} = \frac{2\pi}{\lambda} n_p \cos \theta_i \quad (2.9a)$$

$$k_{y,m,d} = \sqrt{\varepsilon_{m,d} \left(\frac{2\pi}{\lambda} \right)^2 - k_x^2}. \quad (2.9b)$$

The fraction of the power of the incident light that is reflected, represented by the reflectivity is given by,

$$R = |r_{p,m,d}|^2 \quad (2.10)$$

Going back to figure 2.3, a steep decrease or "dip" in the curve is observed at a certain value of x where SPR takes place. Thus, while no SPR condition has been achieved, light is reflected to the photodetector with intensity given by equation 2.10, ideally all of the light from the source is reflected to the photodetector, in reality some losses are present at the air-prism, prism-metal, interfaces. When the SPR conditions are met, ideally all the wave energy travels through the interface in the form of a surface plasmon, thus in this case no light reaches the photodetector. In practice, the strength of the match between incident light and surface plasmon will determine how much of the light reflected to the photodetector when no light is expected, reason for which achieving a good match, by accurately approaching the resonance conditions (angle, wavelength) is of great importance in the performance of a SPR biosensor.

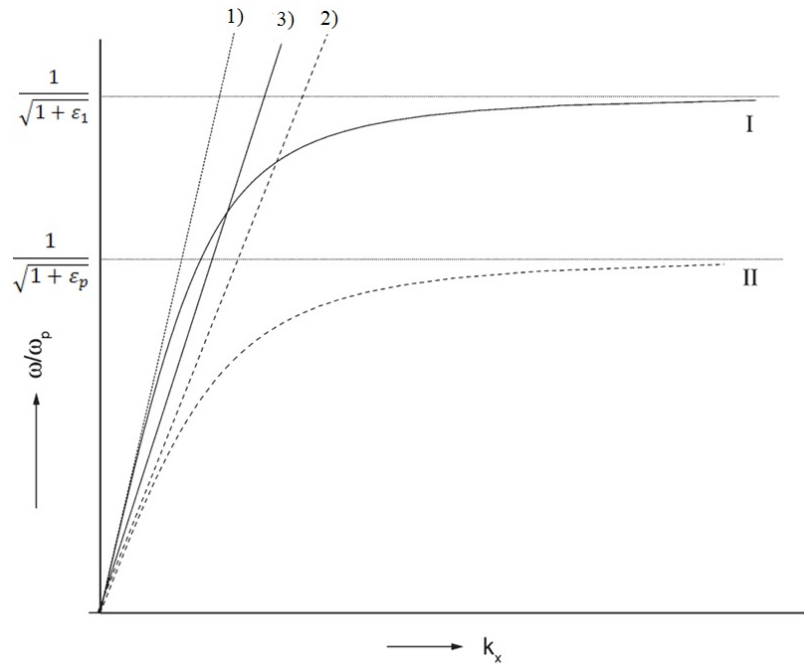


Figure 2.8: Dispersion relation for surface plasmons. Curves I and II represent the SP dispersion for the interfaces prism-metal and metal-dielectric. Lines 1 and 2 are the dispersion relations for incident light with and without the prism respectively. Line 3 can be obtained by changing n_p [15].

2.4 Conclusions

In this chapter, the fundamental concepts in Surface Plasmon Resonance were presented. An emphasis was given to SPR-based biosensors, its principle of operation and the elements that comprise them were described. The electromagnetic basis of SPR are mentioned, presenting the main conditions for achieving SPR: incident light with TM-wave polarization; a metal-dielectric interface is selected due it opposing sign permittivity; and an excitation scheme such as Kretschmann's prism configuration is

needed.

The presence of SPR is monitored with the use of a photodetector, this element being the main focus of this work with the design of a CMOS imager intended to be incorporated in a SPR sensing platform. The correct performance of the system depends among other things in achieving a good coupling between the excitation source and the surface plasmon, which in turn will be seen as changes in the intensity of the detected light at the photosensor. The determination of the optimal conditions under which a good SPR response is expected is one of the main goals of this work and will be discussed with more detail in chapter 4.

Chapter 3

Theoretical Background on CMOS Imagers

In this chapter, the introductory concepts to the subject of CMOS Image Sensors (CIS) are presented. Starting in section 3.1 with the basics of photodetection, where photodiodes as light sensing elements are described. Photodiodes based on CMOS technology, which constitute the core of the pixels in CMOS imagers are presented in section 3.2. The basic pixel's configurations are described in section 3.3. The complementing circuitry on the CMOS image sensor, such as column readout circuitry and noise reduction circuits are briefly described in section 3.5. The Active Column Sensor readout configuration aimed at improvement of the imager is described in section 3.6. Finally in section 3.7 some of the state-of-the-art research of CMOS imagers in biosensors are presented.

3.1 Basics of photodetection

A solid-state image sensor is a semiconductor device that converts an optical image formed by an imaging lens into electronic signals. This device can detect light within a wide spectral range by tuning its photosensing structures and by selecting materials that are sensitive to the wavelength region of interest, particularly the range from 380 to 780 nm that corresponds to the spectral response of the human eye. Silicon is the most widely used material on image sensors because its band gap energy matches the energy of visible wavelength. To reproduce an image with acceptable resolution, a sufficient number pixels must be arranged in rows and columns. These pixels convert the incoming light into a signal charge (electrons or holes).

Photo-conversion takes place when photons arrive at a semiconductor's surface, where part of the incident light is reflected, and the rest is absorbed producing electron-hole pairs (photo-generated carriers). Photon absorption requires that its energy $E_{photon} = hc/\lambda$ exceeds the semiconductor's band gap (E_g), where $h = 6.626069 \times 10^{-34}$ J·s is Planck's constant, c is the speed of light and λ is the light wavelength.

3.1.1 P-N photodiode

CMOS image sensors can use photogates, phototransistors or photodiodes as photo-sensing elements, the latter being the most widely used. A p-n junction photodiode is a device whose reverse current increases when it absorbs photons. Every time a photon is absorbed an electron-hole pair is created, and if an electric field E is applied, the charge carrier can be transported. There are three regions where the electron-hole pairs can be generated, as shown on figure 3.1 [22].

1. *Region 1 (depletion region)*: Electron-holes generated here quickly drift in the opposite direction under the influence of an electric field. Since the electric field points in the n-p direction electrons move to the n side and holes to the p side. This results in a photocurrent created in the external circuit which flows from the n to the p region. Recombination does not take place in the depleted region.
2. *Region 2*: In this region the electron-hole pairs are generated just outside the depletion region and have the possibility of entering the depleted zone by random diffusion. An electron from the p side is quickly transported across the junction and can contribute a charge q to the external circuit. A hole coming from the n side experiences a similar effect.
3. *Region 3*: In the region farther away from the depleted region, the electron and holes generated can't be transported due to the absence of an electric field. Thus they wander randomly until they recombine and consequently they don't contribute to the generated photocurrent.

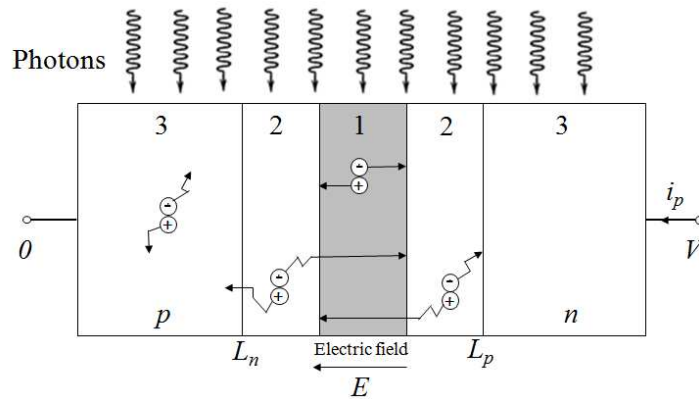


Figure 3.1: Photons illuminating a reverse biased p-n junction [22].

The total reverse current of the pn-junction photodiode is given by:

$$I_L = I_{ph} - I_s \left[\exp \left(\frac{qV}{nK_B T} \right) - 1 \right]. \quad (3.1)$$

Where n is an ideal factor, V the applied voltage, q the electron charge, K_B Boltzmann's constant, T the temperature and the saturation or diffusion current I_s is given by:

$$I_s = qA \left(\frac{D_n}{L_n} n_{po} + \frac{D_p}{L_p} p_{po} \right). \quad (3.2)$$

Where $D_{n,p}$ are the diffusion coefficients; n_{po} and p_{po} are the minority carrier concentrations in the n-type and p-type regions; A is the cross-section area of the diode; and L_n and L_p are the diffusion lengths, representing the average distances at which electrons and holes diffuse before recombining, and are defined as $L_{n,p} = \sqrt{D_{n,p}\tau_{n,p}}$, where $\tau_{n,p}$ are the electron and holes recombination lifetimes.

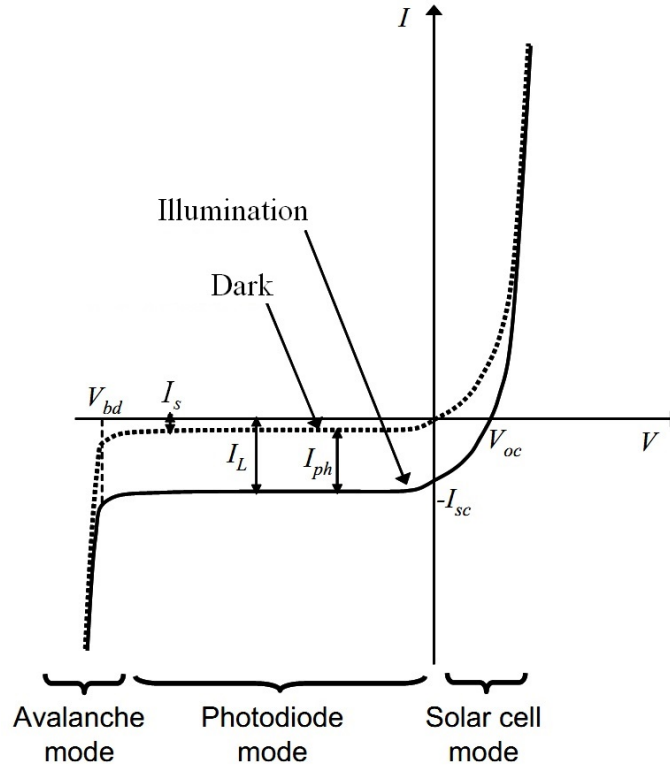


Figure 3.2: I-V characteristic curve of a photodiode [23].

Figure 3.2 shows the three modes of operation for a photodiode depending on how the bias voltage is applied: solar cell, photodiode, and avalanche mode [23].

- *Solar mode*: In this mode, no bias is applied and under illumination, the photodiode acts as a generator, producing a voltage across the p-n junction. In figure 3.2 V_{oc} is the open circuit voltage. In open circuit, this voltage is by obtained making $I_L = 0$ in equation 3.1:

$$V_{oc} = \frac{K_B T}{q} \ln \left(\frac{I_{ph}}{I_s} + 1 \right) \quad (3.3)$$

- *Photodiode*: If a reverse bias is applied across the junction, the exponential term on equation 3.1 can be neglected, thus the total photocurrent current is given by,

$$I_L \approx I_{ph} + I_s, \quad (3.4)$$

in this mode of operation the photocurrent lineally increases according to the input light intensity.

- *Avalanche mode*: When the photodiode is strongly reverse biased, the photocurrent increases as shown in figure 3.2. This phenomena is called an avalanche, where impact ionization of electrons and holes occurs and the carriers are multiplied. The voltage where this happens is the breakdown voltage V_{bd} . This principle is the basis of avalanche photodiodes detectors (APD).

3.1.2 Responsivity and quantum efficiency on Photodiodes

The quantum efficiency of a photodiode, η_Q , is defined as the ratio of the number of generated photocarriers to the number of the incident photons, given by:

$$\eta_Q = R_{ph} \frac{hc}{q\lambda} \quad (3.5)$$

Where $R_{ph} = I_{ph}/P_0$ is the responsivity, defined as the amount of photocurrent produced (I_{ph}) when an unit of light power is incident on the material (P_0). The quantum efficiency depends on the absorption coefficient $\alpha(\lambda)$, the depletion region width W and the distance from the surface to the edge of the depletion region L_p , as shown on figure 3.3 and is expressed as [23]:

$$\eta_Q = [1 - \exp(-\alpha(\lambda)W)] \exp(-\alpha(\lambda)L_p). \quad (3.6)$$

The responsivity for the photodiode is then given by:

$$R_{ph} = \frac{q\lambda}{hc} [1 - \exp(-\alpha(\lambda)W)] \exp(-\alpha(\lambda)L_p) \quad (3.7)$$

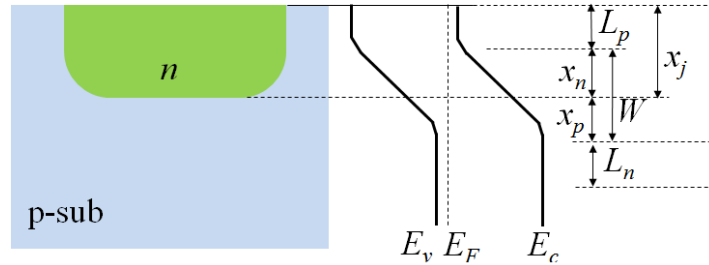


Figure 3.3: p-n junction, where x_j is the junction's position from the surface. The length of the depletion region in the n and p-type material is x_n and x_p respectively. The width of the depletion region is $W = x_n + x_p$. L_n and L_p are the diffusion lengths.

The sensitivity spectrum of silicon to the incident light's wavelength is shown on figure 3.4, with the solid line representing the responsivity and the dashed line is the quantum efficiency. This curve is dependent on the n-type and p-type impurity profiles and the position of the p-n junction x_j , with only the photo-generated carriers in the depletion region accounted for. In practice, the photodiode on an image sensor is coated with SiO_2 and Si_3N_4 , and thus the quantum efficiency is reduced.

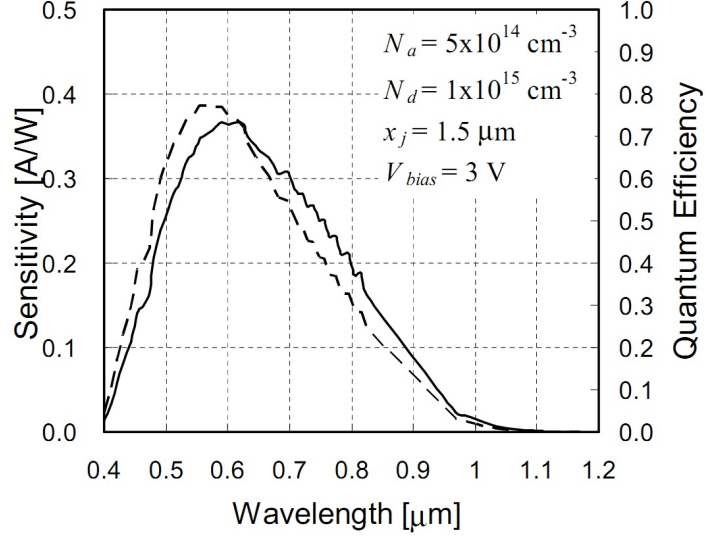


Figure 3.4: Responsivity and quantum efficiency of a Si photodiode

3.1.3 Noise in photodiodes

A photodiode experiences shot noise and thermal noise. The source of the first one are fluctuations in the number N of electrons and photons, plus a contribution from the dark current of the device. The total shot noise is inherent to the photodiode and is given by:

$$i_{sh,rms} = \sqrt{2q\bar{I}\Delta f}. \quad (3.8)$$

Where \bar{I} is the average photodiode's current and Δf is the bandwidth. The signal-to-noise ratio (SNR) for shot noise of a photodiode is expressed:

$$SNR = \frac{\sqrt{\bar{I}}}{\sqrt{2q\Delta f}}. \quad (3.9)$$

Where it is observed that as the amount of current decreases, the SNR associated with shot noise decreases.

The thermal noise, is a white noise due to the distribution of the electron's energy. When considering the parasitic resistances (R), present when accessing the pixel's transistors, the thermal noise can be expressed as:

$$i_{t,rms} = \sqrt{\frac{4K_B T \Delta f}{R}} \quad (3.10)$$

In CMOS image sensors the thermal noise presents itself mainly as reset noise, discussed in section 3.4 [23].

3.1.4 Dark current on photodiodes

The dark current or current under no-light conditions on photodiodes is produced by several sources [23].

- *Saturation current*: It depends on the diode area (A), the density of states in the conduction (N_c) and valence (N_v) bands, the bandgap (E_g), the diffusion coefficients (D_n, D_p) and diffusion lengths (L_n, L_p). Shown on figure 3.2, this current can also be obtained by:

$$I_S = qA \left(\frac{D_n}{L_n N_A} + \frac{D_p}{L_p N_D} \right) N_c N_v \exp \left(-\frac{E_g}{K_B T} \right) \quad (3.11)$$

- *Tunnel current*: Consists of band-to-band tunnelling (BTBT) and trap-assisted tunnelling (TAT), which has an exponential dependence on the bias voltage but little dependence on the temperature. This type of current is important when doping is large and thus the depletion width becomes thin, leading to tunnelling.
- *Generation-recombination current*: Occurs when in the depletion region the carrier concentration is reduced, producing carrier generation instead of recombination.
- *Impact ionization current*: This current increases the dark current as the bias voltage increases. The bias dependence on the dark current by impact ionization arises from the voltage dependence of the ionization coefficients of electrons and holes, α_n and α_p . These coefficients exponentially increase as the bias voltage increases.
- *Frankel-Poole current*: Originates from the emission of trapped electrons into the conduction band and strongly depends on the bias voltage, which is the same as the tunnelling current.
- *Surface leak current*: Dependent on the intrinsic carrier concentration, surface recombination rate, and surface area of the photodiode

3.2 CMOS photodiodes

An integrated circuit is made up of multiple layers according to the steps defined by the CMOS fabrication process [24], with each layer defined using a photomask and a photolithographic process, i.e. CMOS structures are created by superimposing several layers of different materials. Figure 3.5 shows a cross-sectional view of the layers involved in the formation of NMOS and PMOS transistors, such as n-diffusion, p-diffusion, polysilicon gate, metal layers, among others.

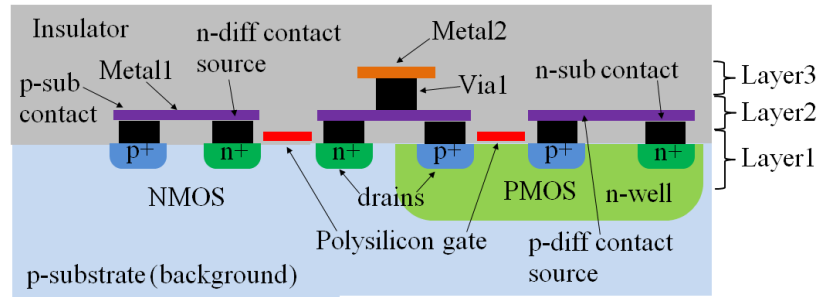


Figure 3.5: Cross-section view of a CMOS wafer.

For a pixel with a photodiode light sensitive element, three types of diodes are available, according to the structure formed with the standard CMOS process (figure 3.6) [25]:

1. **n-diffusion/p-substrate (n-diff/p-sub):** This type of CMOS photodiode has the simplest structure (figure 3.6a). Similar to NMOS devices, where heavily doped n-diff regions (drain or source) are formed within a lightly doped p-substrate. In a CMOS photodiode, the drain (or source) is the cathode and a heavily doped p region will be the anode. Because of the high doping (donor) concentration, the width of the depletion region is small, resulting in a large junction capacitance and thus a lower charge to voltage conversion, ultimately leading to lower quantum efficiency.
2. **n-well/p-substrate (n-well/p-sub):** In this type of photodiode (figure 3.6b), a n-region or n-well is implanted in a p-substrate. Similar to the structure of the PMOS devices, where p-diffusion regions are implanted in the n-well. For a CMOS photodiode, the lower donor concentration increases the depletion region width and decreases the junction capacitance, thus this photodiodes can achieve a higher efficiency. Additionally, the n-well implant and thus the junction are deeper, which improves the collection efficiency of long wavelength photons. The layout design rules require larger minimum spacing and widths for this photodiode than for the n-diff/p-sub, resulting in lower fill factors.
3. **p-diffusion/n-well/p-substrate (p-diff/n-well/ p-sub):** This photodiode is similar to the n-well/p-sub photodiode with the addition of a p-diffusion at the top of the n-well (figure 3.6c). These device has then two junctions, the p-diff/n-well and n-well/p-sub. As a results these photodiodes have a larger depletion region than the previous photodiodes. In theory they are expected to have a better collection efficiency. However, the depletion capacitances of both junctions add in parallel lowering the charge to voltage conversion. An advantage of this photodiode is that since the p-diff layer has a high hole concentration, it has a lower dark current than the other photodiodes.

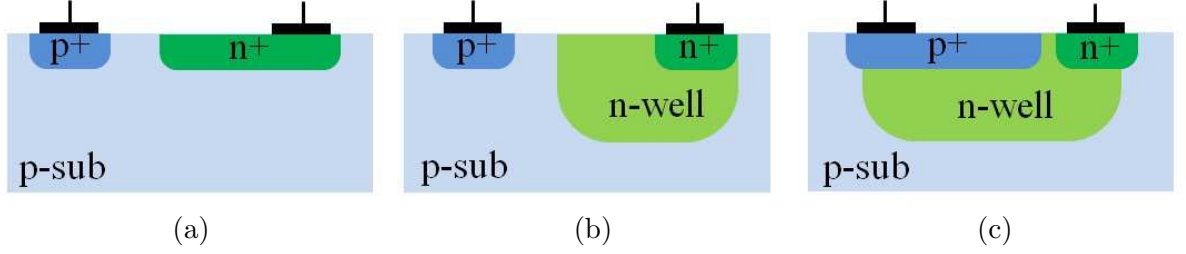


Figure 3.6: CMOS photodiodes. (a) n-diff/p-sub, (b) n-well/p-sub, (c) p-diff/n-well/p-sub.

3.2.1 Charge collection and transfer

In order to measure the incident light's intensity, the photo-generated charges need to be measured. This can be done by integrating the accumulated electrons (or holes) in a capacitor and then read them at given time intervals. Subsequently, the capacitor is taken to a know level and the process started again. Most imagers, including CMOS image sensors are based on this technique [26]. The integration capacitor is dominated by the junction capacitance of the photodiode itself and is given by [24]:

$$C_{PD} = C_J + C_{JSW}. \quad (3.12)$$

Where C_J is the bottom junction capacitance and C_{JSW} is the sidewall junction capacitance, given by:

$$C_J = \frac{A \cdot C_{J0}}{\left(1 + \frac{V_{PD}}{\Phi_0}\right)^{mj}}, \quad (3.13)$$

$$C_{JSW} = \frac{P \cdot C_{J0SW}}{\left(1 + \frac{V_{PD}}{\Phi_{0SW}}\right)^{mjsw}}. \quad (3.14)$$

Where A is the area, C_{J0} is the zero bias area junction capacitance, Φ_0 is the built-in potential (junction), V_{PD} is the applied voltage (reverse bias), mj the area grading coefficient, P the side-wall perimeter, C_{J0SW} the zero bias side-wall junction capacitance, Φ_{0SW} the side-wall built-in potential, $mjsw$ the side-wall grading coefficient. These parameters can be obtained from the technology process parameters of the selected foundry. In order to obtain the photodiode voltage at a certain time, the following relation is used:

$$C_{PD}(V) \frac{dV}{dt} + I_{ph} + I_d = 0. \quad (3.15)$$

Where I_d is the dark current. Solving 3.15:

$$V_{PD}(t) = (V_{PD,0} + \Phi_0) \left[1 - \frac{(I_{ph} + I_d)(1 - m_j)}{C_{PD,0}(V_{PD,0} + \Phi_0)} t \right]^{(1-m_j)^{-1}} - \Phi_0. \quad (3.16)$$

Where $V_{PD,0}$ is the initial photodiode voltage and $C_{PD,0}$ the initial capacitance value. From equation 3.16 we observe an almost lineal decrease in time of the diode's voltage. As we can observe on figure 3.7, the larger the illumination the larger the discharge on the photodiode's voltage for a given integration time, in the case of the figure 30 fps ($t_{int} = 33$ ms).

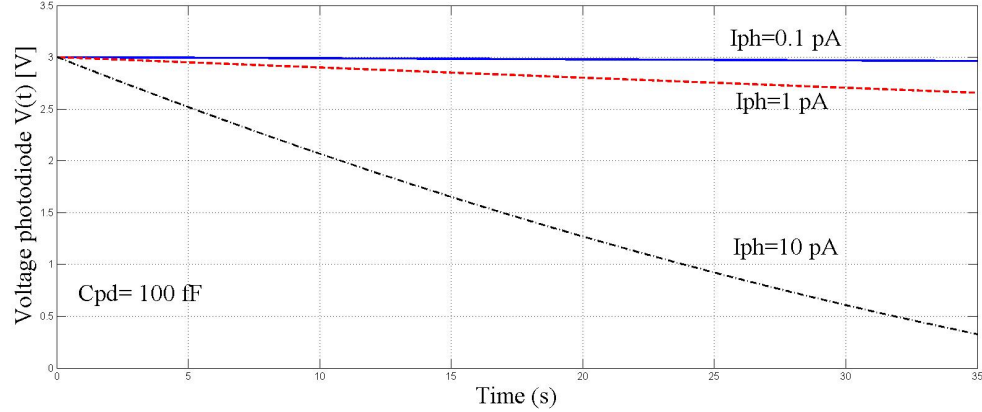


Figure 3.7: Photodiode voltage as a function of time for different illumination levels.

The light intensity can be estimated by obtaining I_{ph} and measuring the output voltage at a certain integration time t_{int} , given by:

$$I_{ph} = \frac{C_{PD,0}(V_{PD,0} + \Phi_0)}{(1 - m_j)t_{int}} \left[1 - \frac{V_{out} + \Phi_0}{V_{PD,0} + \Phi_0} \right]^{(1-m_j)} - I_d. \quad (3.17)$$

3.3 Pixel configurations

A pixel can be described by the following specifications [26]:

- *Fill factor (FF)*: Defined as the ratio of sensing area (photodiode) to total area of the pixel, which ultimately impacts the sensitivity of the imager.
- *Conversion Gain (CG)*: Is defined as the voltage change when one charge (electron or hole) is accumulated in the pixel's floating diffusion node (photodiode). It depends on the photodiode junction's capacitance according to the relation $CG = q/C_{PD}$ expressed in $\mu\text{V}/q^-$ and where q is the electron charge.
- *Full Well Capacity*: Is the maximum number of charges that can be accumulated on the photodiode. This parameter is limited by the size of the photodetection site and by the readout circuits. Dividing the CG with the saturation voltage of the pixel give us the full well capacity, expressed in number of electrons:

$$N_{sat} = \frac{V_{sat}}{CG}. \quad (3.18)$$

- *Dynamic range*: Is the ratio of the maximum output signal that can be imaged by the pixel (saturation) and the noise level or minimum detectable signal value:

$$DR = 20 \log \left(\frac{V_{Max}}{V_{Min}} \right). \quad (3.19)$$

The first pixel structure developed for CMOS image sensors was the passive pixel sensor (PPS). It is composed only of a one photodiode and one switching transistor, similar to a DRAM. The main advantage of PPS, beside its simplicity, is its larger fill factor. However, on PPS a larger noise level is present [23]. This type of pixel configuration has been replaced by imagers based on Active Pixel Sensors (APS) that contain an active element which amplifies the signal at each pixel.

3.3.1 Active Pixel Sensors

3.3.1.1 3T-APS

The simplest APS configuration is the three transistor pixel (3T-APS), presented on figure 3.8, its operation is as follows:

1. The cycle starts when the row select transistor (M3) is turned on (selecting all of the pixels of a same row of the matrix). If implementing a noise reduction circuit, such as double sampling, it is required to access the pixel before reset, thus ROW_SEL is activated slightly before M1 is turned on in order to read the signal at the end of integration time.
2. The reset transistor (M1) is then turned on to take the photodiode to a known voltage in order to begin integration. For the configuration of figure 3.8a this reference voltage is $V_{DD} - V_{th}$, where V_{DD} is the supply voltage and V_{th} is the MOSFET threshold voltage. Advance reset techniques looking to reduce the image lag and reset noise have been developed, such as active reset [27] and flushed reset [28] among others. The reset and select transistors if possible should have minimum dimensions in order to maximize the pixel's fill-factor.
3. Integration starts when the reset transistor is turned off. During this integration time, the photogenerated charge discharges the sensing capacitor. The drop in the voltage at the sensing node (V_{pix}) of the photodiode is proportional to the incident light as described by equation 3.16.
4. When the row select signal is active, the source-follower (SF) transistor M2 buffers the photodiode voltage to the pixel's output $V_{0,pix}$. The source-follower requires a current sink, usually shared per column. Since the SF is inside the pixel, if possible its size is kept at a minimum .

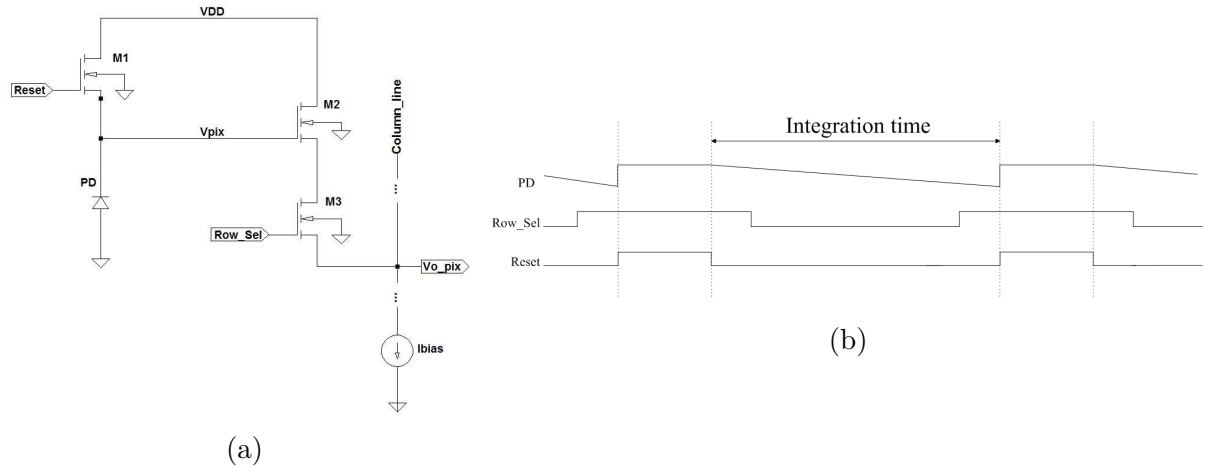


Figure 3.8: 3T-Pixel configuration. (a) Schematic. (b) Timing

The introduction of the SF (amplification) transistor on the APS accounts for the image quality improvement compared to the Passive Pixel Sensor. In PPS the accumulated signal charges are transferred directly to the pixel's output. In APS there is a conversion of the accumulated signal charges to a potential in the gate. In the configuration using SF, the voltage gain is less than one, while the charge gain is determined by the ratio of the accumulation node charge C_{PD} to a sample and the hold node charge C_{SH} which will be explained in later sections.

The main advantage of 3T-APS is a larger fill factor, due to the smaller number of transistors as opposed to the more advance pixel's configuration. However they present some disadvantages such as: difficulty to suppress reset noise and the photodiode acts simultaneously as photodetection and photoconversion region.

3.3.1.2 4T-APS

This configuration solves some of the issues with 3T-APS by separating the photodetection and photoconversion regions (figure 3.9). The accumulated charge is transferred to a separate node, known as floating diffusion (FD), where the carriers are converted to voltage. One extra transistor must be added to transfer the charge from the photodiode to the FD. Its operation is as follows:

1. Assuming initially no charge on the photodiode, slightly before the charge transfer the FD capacitance is reset through transistor M2.
2. The reset value is read and the select transistor (M4) activated.
3. After reset readout, the signal charge accumulated in the PD is transferred to the FD by turning on the TG signal on transistor M1, then this new signal is read.
4. This process is repeated periodically reading the signal charge and reset charge.

On this configuration the timing is essential for CDS operation and can be done by separating the charge accumulation region (PD) and the charge readout region (FD); this timing eliminates reset noise which cannot be completely done with the 3T-APS. Implementing a true-CDS, the 4T-APS achieves low noise operation and thus its performance is comparable to CCDs. On 4T-APS the PD must be drained of charge completely in the readout process. For this, a pinned photodiode (PPD) is required, which incorporates a surface p+ layer and the potential well is separated from the trap. This configuration also allows for global shutter mode of operation.

The 4T-APS performance is better than the 3T-APS in its lower noise level, however there are still some issues with this configuration, such as:

- The extra transistor (with respect to the 3T-APS) reduces the pixel's fill factor.
- Image lag may occur when the accumulated signal charge is completely transferred into the FD.
- Difficulty to establish fabrication process parameters for the PPD, transfer gate, FD, reset transistor, and other elements.
- More complex timing.

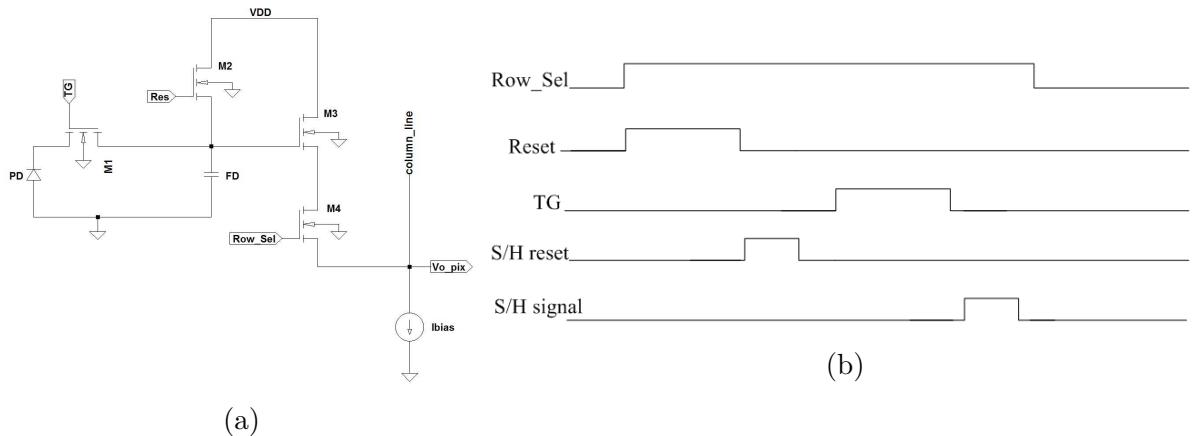


Figure 3.9: 4T-Pixel configuration. (a) Schematic. (b) Timing

3.3.1.3 Other Pixels configurations

Special functions can be included in the pixel, such as ADC per pixel, improved reset techniques, etc. However, the inclusion of such functions in the pixel leads to an increase in the number of transistors. Thus a trade-off between the benefits of these specialized pixels and the reduction in FF must be made. Furthermore, the structure of the pixel can differ from the traditional APS in order to implement different approaches such as current-mode APS and logarithmic pixels [23].

3.4 Noise on CMOS imagers

On CMOS image sensors two types of noise can be identified: temporal and spatial. The temporal noise is related to the difference between two successive samples on a same pixel under constant illumination, and it has its origin in the noise spectral densities of the different elements of the pixel, which are added to the offset variations during the readout process, the sources of temporal noise are [29]:

- *Electronic shot noise*: Due to the aleatory nature of the electrons and accounts for fluctuations in the currents present on the photodiode. Often can be neglected.
- *1/f noise*: Also known as flicker noise, is a dominant source of noise for long exposure times (low illumination) and it can be neglected as the frequency increases in shorter exposure times. It is due to conductance fluctuations caused by traps in the channel interface, the junctions and contacts in general.
- *Reset noise* or *$K_B T C$ noise*: It is the thermal noise in the CMOS image sensor, named as such since the reset operation is the main source of this kind of noise. It appears during this operation at the charge-detecting node, as a noise level given by $4K_B T R_{ON} \Delta f$. Where R_{ON} is the reset transistor's ON resistance [23]. Suppressing it depends on the implementation of reduction techniques in the pixel's configuration, such as active reset [27] or flushed reset [28].
- *Read noise* or *noise floor*: Is a noise that comes from the readout electronics, not including the noise generated from the photodetection. In CMOS image sensors, the noise floor is determined by the noise generated by readout electronics, including the amplifier inside the pixel. If an image sensor has additional circuits, such as a gain amplifier and FPN suppression circuit, the noise generated by them is included in this type of noise

On the other hand, the spatial noise or Fixed Pattern Noise (FPN) represents the circuit's spatial non-uniformities and it depends on the fabrication process. Variations in the threshold voltage of the pixel's source follower are one of the main contributors to this type of noise at the pixel level. On CMOS transistors these differences are more prevalent as the dimension decreases, if possible larger transistor sizes are used, thus a trade-off between noise and fill factor must be made. Inside the pixel two cases of FPN are distinguished [26]:

- *DSNU (Dark Signal Non-Uniformities)*: Present under dark conditions, it refers to an offset variation in the output signal due to variations in the dark current from pixel to pixel. DSNU can be thought as the distribution of dark voltages for each pixel. The dark voltage average refers to the average output observed under no illumination and is caused by the charges generated from mechanisms independent of the incident light.
- *PRNU (Photo Response Non-Uniformities)*: This type of spatial noise refers to variations in the output signal for each pixel when exposed to uniform illumination.

PRNU depends on the process (doping impurities, varying layer thickness), light source spectrum, pixel type, etc. It is given by:

$$PRNU = \frac{V_{MAX} - V_{MIN}}{2V_{AVG}}. \quad (3.20)$$

Where V_{MAX} is the maximum output value, V_{MIN} the minimum voltage and V_{AVG} is the average output voltage.

Mismatches in the column circuits also contribute to FPN, thus this type of spatial noise can be modelled as a zero mean, random variable, with a column FPN contribution, and a pixel FPN contribution [30]. Figure 3.10 shows examples of images for the different type of FPN on CIS.

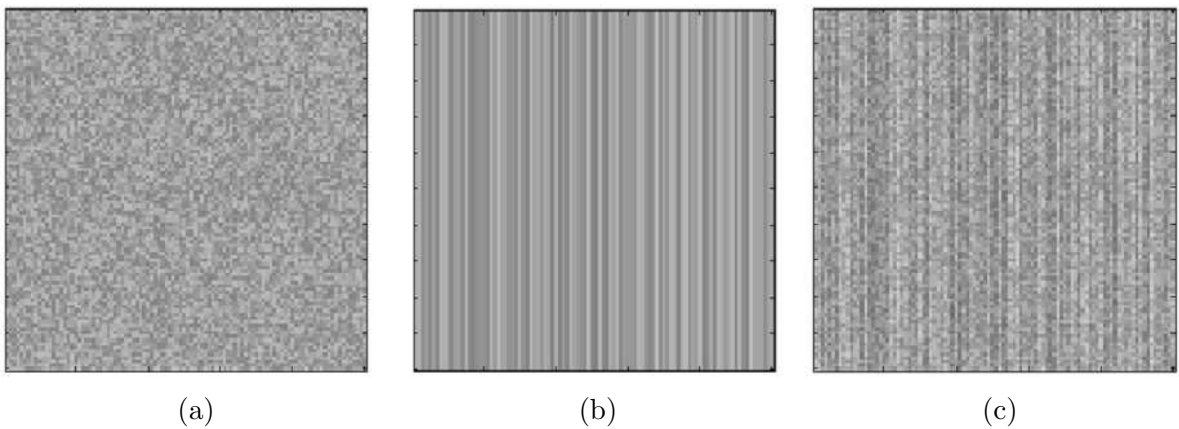


Figure 3.10: FPN on CIS. (a) Pixel-level, (b) Column-level, (c) Total-FPN. [31]

3.5 Readout Circuits

3.5.1 Addressing

The signal is obtained by scanning the pixel array vertically (columns) and horizontally (rows). The row scanning controls the row-select and reset signals for each pixel in a frame time. The column scanner access the columns during every row period. Two common scanning devices used in CMOS image sensors are the shift register and the decoder. The advantages of the shift register are its simple configuration and low flip noise generation. As for a decoder, this device allows greater scanning flexibility and window-of-interest readout. A decoder arbitrarily converts N input data to 2^N output data using customized random logic circuits.

3.5.2 Source Follower

CCD imagers transfer the photogenerated charges to an amplifier located at the end of the CCD register, thus all signals are read out through the same amplifier, therefore the amplifier's offset is constant. On the other hand, on CMOS-APS each pixel has an amplifier, often a source follower, to transfer the collected charges. Threshold voltage variations on the source follower transistor are the largest source of noise in CMOS imagers and usually fall in the range of several tens of millivolts [32].

As seen on figure 3.8 the select transistor M3 is placed between the SF transistor M2 and a current sink load (shared by all the pixels in a same column). This amplifier has a gain given by:

$$A_v = \frac{g_m}{g_m + g_{mb}}, \quad (3.21)$$

where g_m is the transconductance and g_{mb} the transconductance due to the bulk-source voltage. For a current load of $2 \mu\text{A}$ for example, and the parameters for the AMS $0.35\mu\text{m}$ CMOS process [33] the value of the gain is $A_v \approx 0.85$.

3.5.3 Noise reduction circuits

In order to reduce the noise present on CMOS imagers several methods can be implemented, such as double sampling, depending on the pixel configuration selected.

3.5.3.1 Correlated Double Sampling (CDS)

This technique works by making two successive readings on the same pixel during the same frame time. First, a reading is made of the reference level immediately after opening the reset transistor, this signal contains a level representing the amplifier's offset. Then a reading of the pixel's output at the end of integration is made, this signal also contains the amplifier's offset (figure 3.11). This technique is then based on the fact that the read noise is only present during the time the reset transistor is closed. This noise induces fluctuations around the nominal voltage V_{reset} . After the activation of the reset transistor the voltage has a medium value $V_{reset} - V_{offset}$. When the two samples are taken, the voltages are subtracted and the noise associated with the amplifier's offset eliminated [29]. However, it should be mentioned that offsets caused by dark current variations cannot be suppressed with this technique.

This technique is efficient, however it can only be used in few cases because of its complexity, since during the integration time the entire matrix is scanned, at the moment of the second reading the reset voltage of that pixel must be recovered. In addition, requires pixels of 4 or more transistors in order to be implemented, with the associated fill factor reduction costs. Besides 4T-pixels, another possible implementation of CDS is the use of a memory to store the reset voltages for each pixel [34], with the associated disadvantages of significantly increasing the chip's surface and complex timing control.

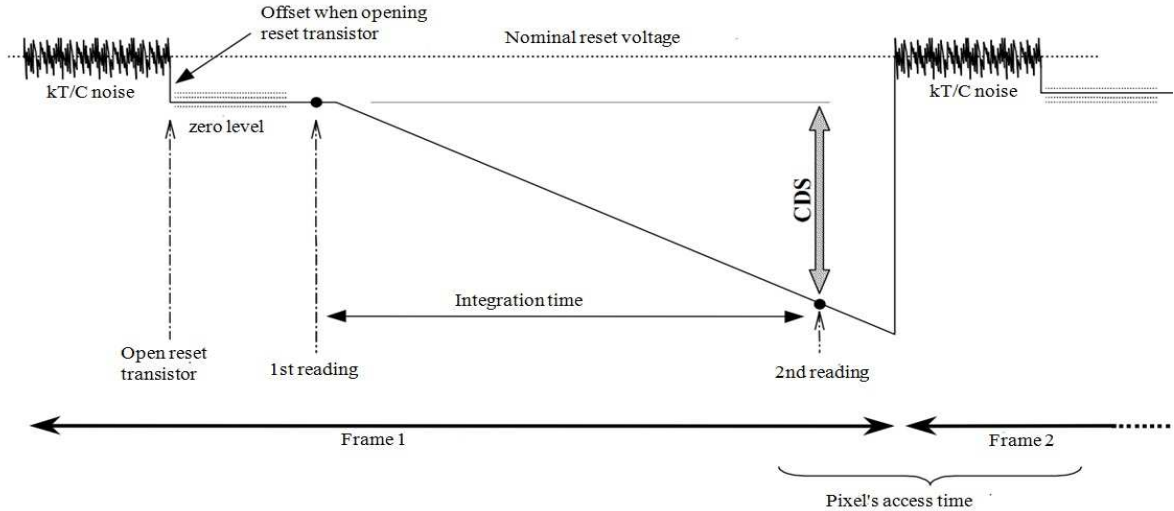


Figure 3.11: Correlated Double Sampling Principle (CDS) [29].

3.5.3.2 Non-Correlated Double Sampling (NCDS)

An alternative to some of the problems with CDS is to use Non-Correlated Double Sampling (NCDS), which is easily implemented on 3T-pixel imagers. This method consist of subtracting the voltage at the end of integration and the reset voltage of the same pixel, but on the next frame, as seen on figure 3.12. This technique will be only useful to eliminate the offset due to the opening of the reset transistor and the offsets associated to the acquisition chain, however it's recommended to use for low read noise levels.

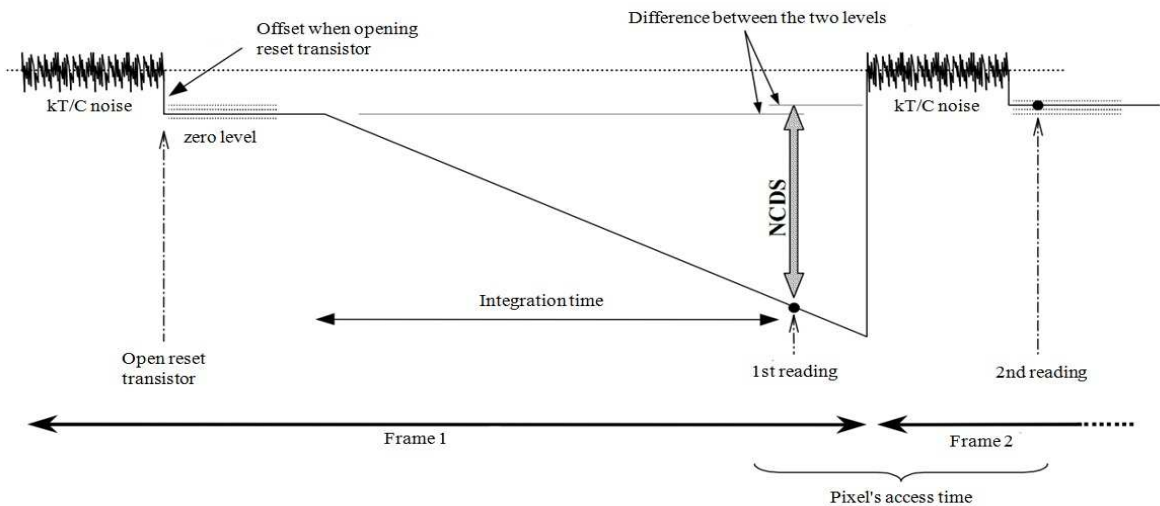


Figure 3.12: Non-Correlated Double Sampling (NCDS) principle [29].

3.5.3.3 Delta Double Sampling (DDS)

The differential delta sampling (DDS) noise suppression circuit was introduced to eliminate the characteristic mismatch between the two signal paths in a differential FPN suppression circuit. It consists of two identical structures that are treated the same way and measure the dispersion of the output signal. It is used to improve the correspondence between the column amplifiers and the pixels and improve the performance of CDS or NCDS. In fact, this technique cannot be implemented by itself without the use of some of these two techniques [29]. Figure 3.13 shows a FPN suppression column circuit with DDS. In it, the sample and hold (S/H) capacitors, C_{SHS} and C_{SHR} , sample the signals, V_{SHS} and V_{SHR} respectively. When the i -th column is selected, two parallel PMOS source follower circuits are activated and buffer the differential outputs that correspond to V_{sig} and V_{res} . When the two S/H capacitors are shorted by activating the DDS switch, the outputs change, depending on voltage differences between V_{sig} and V_{res} [32]. This circuit operation will be explained in more detail in chapter 5.

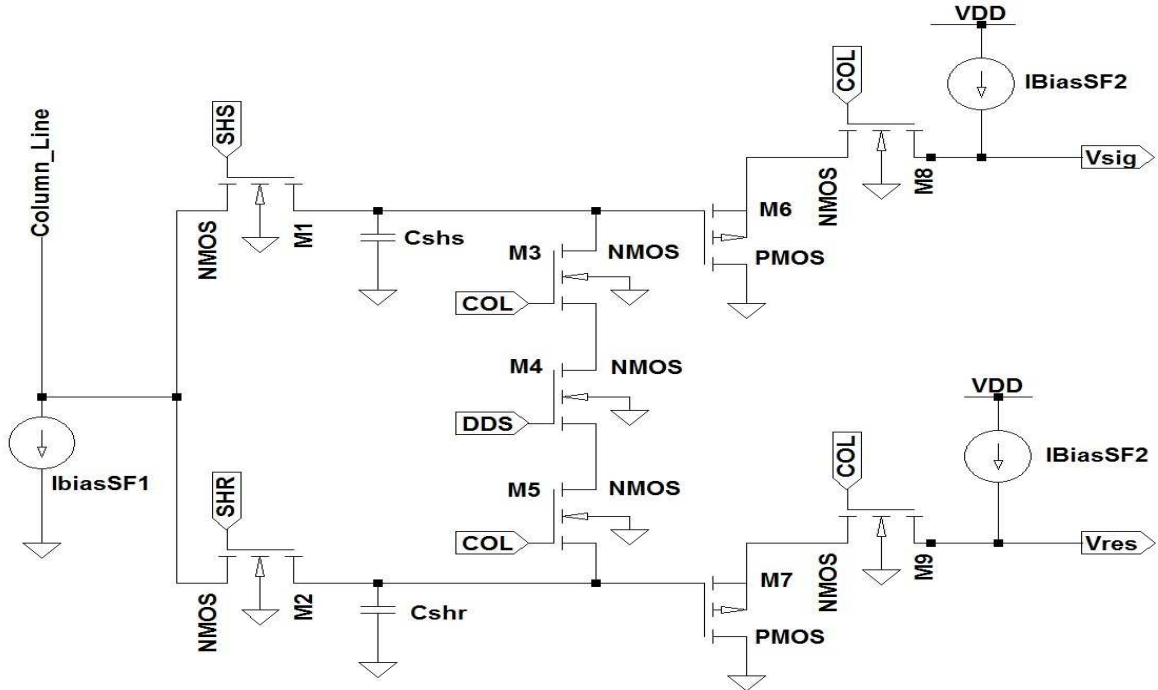


Figure 3.13: Delta Double Sampling circuit [29].

3.5.4 Output Stage

The three types of possible signal output are: analog, digital, and SOC (System on a chip) outputs. For analog output some variations exist, such as a single-ended output (with the on-chip FPN suppression) and differential dual-output (one corresponds to V_{sig} and the other for V_{res}). Digital output by an on-chip analog-to-digital converter (ADC) has become more and more popular for consumer applications because it can

make a camera-head design extremely simple by eliminating the analog interface from the image sensor and the analog-front-end circuit. In an SOC-type image sensor, a digital signal processor is implemented. Basic image processing, such as exposure control, gain control, white balance, and color interpolation, is implemented in the on-chip processor.

3.6 Active Column Sensor readout

With the technique known as Active Column Sensor (ACS), the pixel gain and offset variations in conventional 3T-APS are eliminated by substituting the pixel's source follower by a differential amplifier in unity gain configuration. ACS avoids the reduction of the pixel's fill factor by partitioning the differential input between the pixel and the column circuit. The basic architecture is shown on figure 3.14 for a given column i , where all the pixels in it share the same column readout. The operation of ACS is similar to a 3T-APS (section 3.3). For pixel $(0,i)$, transistor $M1$ connects to the row 0 reset signal, $M3$ is the row 0 selection signal, transistor $M2$ now represents the input to the amplifier, with the rest of the amplifier ($M9-M11$) implemented at the column level.

On a CMOS-ACS imager, the gain variations due to the use of a source follower are suppressed and PRNU reduced. Additionally, the negative level shift also associated with the use of a NMOS-SF, approximately equal to one threshold voltage, is eliminated resulting in a larger output swing. While useful to reduce FPN, the offsets from column-to-column is still be present, requiring the use of CDS/NCDS.

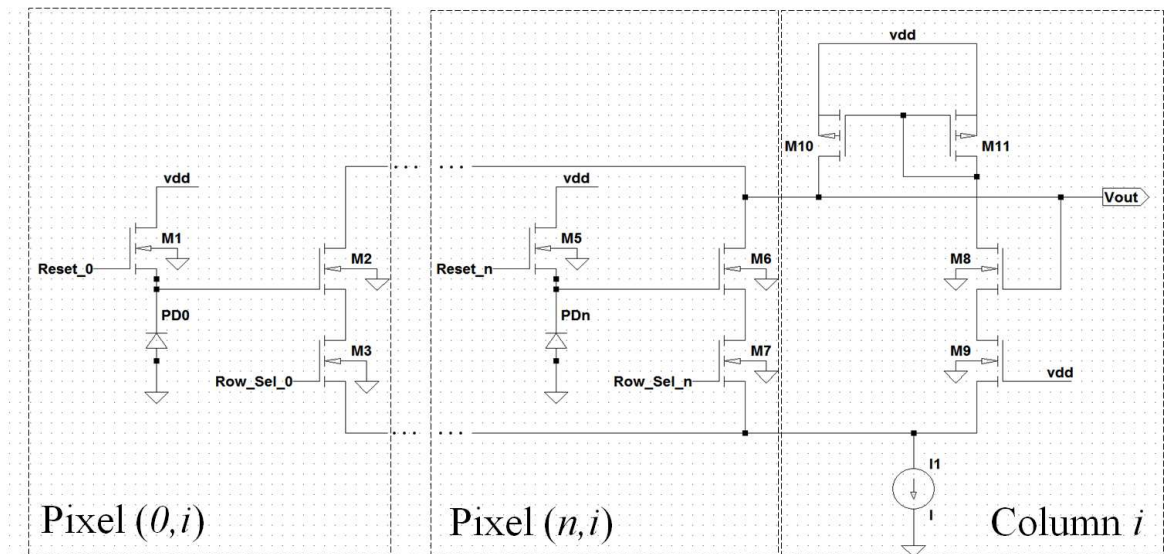


Figure 3.14: Basic schematic Active Column Sensor

3.7 State-of-the-art applications of CMOS Imagers in Biosensing

The research of optical biosensors using CMOS Image Sensors is widely reported, however the use of this type of imager in SPR-biosensors is scarce. Most of the reported works are related to the dominant fluorescence and luminescent techniques. Both custom-made and existing commercial CMOS imagers have been incorporated to optical biosensors. The advantages of custom-made devices are the ease of integration of the optoelectronic device with structures such as microfluidic channels; the ability to perform contact imaging that can reduce the need of optical elements; and the capability to perform specific signal processing. On the other hand, commercial CMOS imagers reduce the design time and provide good performance if integration is not one of the main priorities.

Table 3.1 synthesizes some of the most recent works on CMOS image sensors for optical biosensing. The table includes the main imager specifications as well as the intended application. References [35–40] present CMOS imagers used in fluorescence and luminescence biodetection systems. Depending of the particular application, a certain characteristic is emphasized, such as dynamic range and color detection in reference [36], a high speed acquisition in reference [37], integration with microfluidic channels in reference [38], and the use of pnp phototransistors as photosensing element to generate larger photocurrents than photodiodes in [39, 40]. References [41, 42] present two research projects applying CMOS image sensors to SPR biosensing. Reference [41] focus on improving the system’s performance by implementing a modulation scheme at the light source while using a commercial CMOS imager. Reference [42] evaluate the performance of several phase-sensitive, custom-made CMOS imagers applied to differential-SPR detection, which uses changes in the polarization of the light to detect the position of the SPR angle.

Table 3.1: Examples of CMOS Image Sensors used in optical biosensing applications.

Ref.	Function	Year	CMOS imager specifications
[35]	Lens-free holographic microscopy to analyze the polarity in RWPE1 prostate epithelial cells by observing the optical signature of 3D cellular objects Contact imaging is used by placing the imager directly above the biosensing slide, allowing the reduction of the optical system by avoiding the use of lenses. Three different commercial CMOS image sensors are evaluated.	2013	1. Aptina MT9P031 Color 2592x1944 pixels Dynamic range 70.1 dB SNR 38.1 dB Dark current 25e-/pix/s Read noise 2.6e- RMS Sensitivity 1.4 V/Lux·s 15 fps 2. Mightex BCN-B050-U Mono

			2592x1944 pixels Dynamic range 70 dB SNR 38 dB Sensitivity 1.4 V/Lux·s
			3. VFU-J003-MH-C Mono 3660 x 2748 pixels Dynamic range >65 dB
[36]	Fluorescence contact imaging with tunable color sensing. Quantum dots (QDs) are used as fluorescent markers allowing for multiple colors. The photodetection is done with a custom CMOS imager based on tunable-color photogates that detect light according to the emitted fluorescence wavelength	2013	0.35 μm technology 8x8 pixels FPN 0.38% SNR 46 dB Capacitance 250 fF Dynamic range 82 dB Well capacity 156 ke- Tunable-color photogates Asynchronous self-reset Digital output with on-pixel ADC
[37]	Capture small differences between physiological signal fluorescence to background fluorescence ($\Delta F/F$) in brain tissue. The custom-made CMOS imager is adapted to a microscope imaging system.	2012	32x32 pixels Pixel size 34x74 μm^2 Dynamic range 81 dB SNR 61dB Well capacity of 2.1 Me- Conv. gain 4.9 $\mu\text{V}/e^-$ high speed 900 fps low power <100 mW Weight <2g Detects 0.2% $\Delta F/F$
[38]	Chemiluminescence and electrochemiluminescence-based detection of luminol. The CMOS imager is integrated with a microelectrode array and microfluidic channels.	2012	0.35 μm technology 64x128 pixels Dynamic range 67.8 dB SNR 60.1 dB Well capacity 1.2 Me- Conv. gain 1.6 $\mu\text{V}/e^-$ Dark current 37.7 mV/s Fill factor 27%
[39, 40]	Luminescence optical sensor of gaseous oxygen. The system is integrated with xerogels microarrays and PDMS micro-lenses. The use of pnp phototransistors	2011	0.18 μm technology 32x32 pixels Pixel size 20x25 μm^2 pnp phototransistor Fill factor 56%

	generate photocurrents larger than photodiodes as required by this application.		Dark current 1.89 V/s Capacitance 65 fF CDS On-Chip Control
[41]	SPR compact size biosensor. A rotating mirror is used for light modulation, improving detection limit. A commercial CMOS image sensor is adapted for this application.	2010	0.3 megapixels USB interface Changes 2.5×10^{-6} RIU
[42]	Evaluation of several phase-sensitive custom-made CMOS imagers applied to the differential SPR technique (dSPR). Based on phase-modulation, dSPR uses the changes in the polarization state of the reflected light. The cameras include de-modulation stage tuned to the appropriate frequency	2010	0.35 μm technology 1. A64P 64 \times 64 pixels Pixel size 40x40 μm^2 Well capacity 700 Ke- Fill factor 26% SNR 58 dB 2. A64F 64 \times 64 pixels Pixel size 30x30 μm^2 Well capacity 1.2 Me- Fill factor 35% SNR 61 dB 3. A64x2LI 64 \times 64 pixels Pixel size 25x25 μm^2 Fill factor 56% Logarithmic pixel

3.8 Conclusions

In this chapter, the fundamental concepts of CMOS imagers, that will make the detection stage in an SPR biosensor were presented. The different components of CMOS imagers are described, starting from the core of the pixel, the photodiode. Additionally, different pixels configuration, based on the number of transistors are discussed. The noise affecting the sensor's output is classified as temporal and spatial, describing its sources and some techniques for its reduction, such as CDS, NCDS and DDS. Furthermore, the technique of Active Column Sensor (ACS) is presented. This configuration, by implementing an unity gain amplifier is expected to improve the FPN due the use

of a pixel's source follower. Additionally, ACS increases the output swing of the sensor, by eliminating the level shift associated to a NMOS source follower. The concepts presented in this chapter are used as basis for the design of the CMOS-ACS 32×32 prototype presented in chapter 5.

Chapter 4

Determination of optimal Surface Plasmon Resonance coupling conditions

In this chapter, the finite element analysis (FEA) software, COMSOL Multiphysics [43], is used to simulate the excitation of SPR at a Au-H₂O interface, using a Kretschmann configuration with two types of prisms based on different crystalline forms of silicon dioxide or silica (SiO₂). These materials are selected considering that they are CMOS/Post-CMOS compatible, with the objective of eventually being implemented on an integrated SPR-platform. First, in section 4.2 the gold thickness which results in the minimum reflectivity at the SPR angle is obtained, showing good agreement between the theoretical results and the software simulation. Then in section 4.3, by varying the refractive index of the dielectric medium (water), the minimum SPR angle that can be detected is estimated (resolution). Additionally, in section 4.4 the effects of the inclusion of a Ti adhesion layer are simulated, estimating the increment in the minimum reflectivity that is experienced at the resonance angle. The results achieved are aimed to the development of a miniaturized label-free biosensing platform with a CMOS image sensor photodetection stage. At the short-medium term, these results will provide valuable information in the experimental phase, by letting us known in advance the conditions under which the optimal SPR response is obtained. Furthermore, the flexibility of the COMSOL model will facilitate the introduction of different materials involved in the SPR interface and evaluate its SPR performance beforehand.

4.1 COMSOL simulation

4.1.1 Simulated geometry

The simulations were performed in COMSOL 3.5a, making a 2D analysis with the harmonic propagation RF-module [43]. Figure 4.1 shows the geometry implemented

on COMSOL to model the SPR response, where light from an HeNe laser at 633 nm propagates through the prism of $2 \mu\text{m} \times 2 \mu\text{m}$, an Au layer with thickness d and width $2 \mu\text{m}$, and a water (dielectric) layer of $2 \mu\text{m} \times 2 \mu\text{m}$.

The prism and dielectric layers heights were selected taken into consideration that for a variation in d from 30 to 65 nm, a $2 \mu\text{m}$ height is 30 times larger, thus behaving as a semi-infinite layer and not affecting the resulting excitation. Furthermore, $2 \mu\text{m}$ is an appropriate trade-off between prism's thickness and computational time for larger values. The width of the geometry, while defined as $2 \mu\text{m}$, behaves as if it were infinite, since the lateral boundary conditions are defined as Floquet periodic boundaries, where when the wave reaches the right edge, it is transposed to the left edge with the appropriate phase shift, thus not interfering with the results [44].

The simulation assumes that the incident light is already propagating in the prism, and does not take into consideration the reflection/refraction effects of the transitions from air-prism at the input and prism-air at the output. The incident field is defined at the virtual interface labelled input port by specifying the z -component of the magnetic field (TM-wave). This interface divides the prism in two parts, with the interface acting as a filter for the reflected light, thus at the prism's top layer the output is observed. The bottom boundary is defined as a scattering boundary condition, which perfectly absorbs a plane wave representing a semi-infinite dielectric layer.

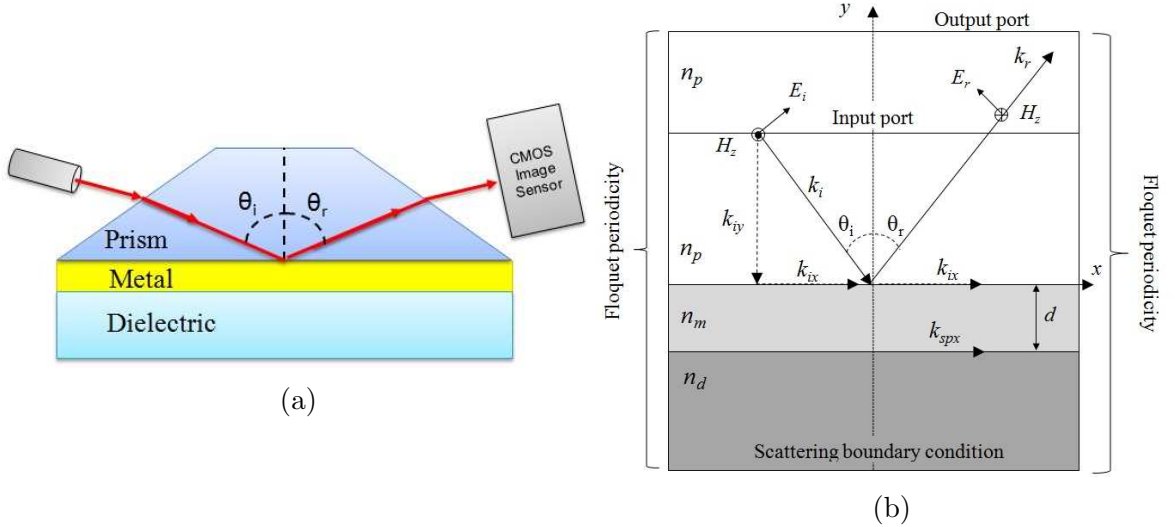


Figure 4.1: Excitation of surface plasmons in the Kretschmann configuration. (a) diagram, (b) wave vector and material layers implemented on COMSOL.

4.1.2 Materials optical characteristics

The optical characteristics of the materials are presented in table 4.1, with the dielectric function of the metal being complex and dependent on the frequency. For the glass prism, two refractive indexes are used, both of silicon dioxide (SiO_2), also known as quartz or silica. According to its crystalline structure, this material can take several

forms such as: quartz, fused silica, tridymite, cristobalite, coesite, among others. Crystal quartz is widely used in the fabrication of finished optics such as: laser beam splitters, polarizing optics, prisms, windows, lenses. The optical grade material has the highest transmittance in the range of 190 - 2900 nm, and has few bubbles and inclusions. In this form, quartz is a positive uniaxial crystal with a ordinary refractive index $n_o=1.54224$ and extraordinary refractive index of $n_e=1.55127$ [45], thus for the first prism an average value of $n=1.55$ is taken. For the second prism, fused silica is used, which is a high purity, amorphous version of quartz and its refractive index is 1.46 at 633 nm [46].

Furthermore, the materials are selected to be compatible with the CMOS/Post-CMOS microfabrication process, with the purpose of the eventual integration of the biosensor. The Post-CMOS process means the addition of nanostructures after the normal CMOS process, and requires a deposition that is kept at a temperature lower than 450 °C to prevent the melting of the CMOS aluminium metal layers and/or affecting the CMOS transistors [47].

Table 4.1: SPR interface and excitation prism optical characteristics.

Layer	Refractive index
SiO ₂ (prism)	1.55 [46]
Fused silica (prism)	1.46 [46]
Gold (at $\lambda=633$ nm)	$0.1856 + j3.4201$ [48]
Water (dielectric)	1.33

4.2 Metal layer thickness

To determine the optimal thickness of the Au film, COMSOL simulations were performed sweeping the incident angle from 60 to 90° with a step size of 0.05° and Au layer thickness ranging from 30-65 nm, with increments of 5 nm; a quad mesh of 6900 elements and 28072 degrees of freedom was considered. First, the simulation is performed for a SiO₂ prism with $n_p = 1.55$, the results are then compared to the theoretical response from equation 2.10, as shown on figure 4.2 and table 4.2. SPRi biosensors are based on measuring differences in the images taken before and after binding interactions that take place on the microarray, thus a more pronounced change in the reflectivity is desired, i.e. larger reflectivity differences represent the better image contrast.

A gold layer of 50 nm produces a better response by achieving a better coupling, as observed by the steep decrease in the reflected light, falling to a minimum of 0.81% at 68.45° in figure 4.2e. It can also be noticed how thinner layers (30, 45 nm) do not necessarily mean a smaller reflectivity level at the photodetector.

The same mesh parameters are used to performed a simulation for a fused silica prism with refractive index of 1.46. The results are presented in figure 4.3 and table 4.3. In them it is observed how the optimal performance is for a gold thickness of 45

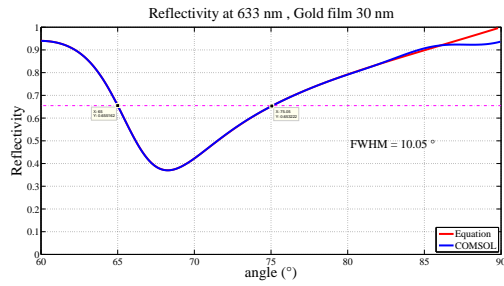
nm, with practically all the light coupled to the SPR interface and only 0.01% of the light being reflected to the imager at an angle of 79.05° .

Table 4.2: Minimum reflectivity and SPR angles with prism $n_p = 1.55$.

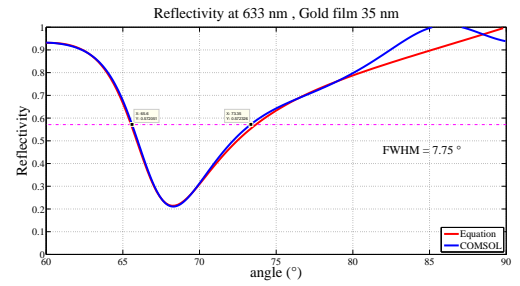
Thickness Au (nm)	R min (%) Eq. 2.10	SPR angle ($^\circ$) Eq. 2.5	R min (%) COMSOL	SPR angle ($^\circ$) COMSOL	Abs. error R (%)	Abs. error SPR angle ($^\circ$)
30	37.03	68.20	37.01	68.25	0.02	0.05
35	21.41	68.20	21.06	68.30	0.35	0.10
40	8.58	68.40	8.27	68.35	0.31	0.05
45	1.12	68.40	1.12	68.40	0.00	0.00
50	0.77	68.40	0.81	68.45	0.04	0.05
55	6.98	68.60	7.27	68.55	0.30	0.05
60	17.66	68.60	18.35	68.60	0.69	0.00
65	30.49	68.60	30.47	68.65	0.01	0.05

Table 4.3: Minimum reflectivity and SPR angles with prism $n_p = 1.46$.

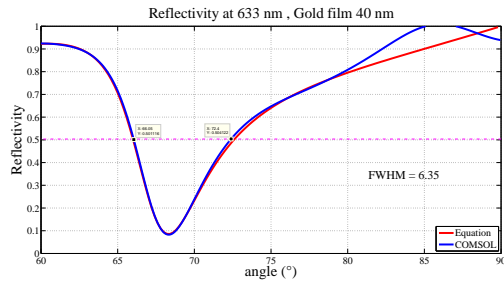
Thickness Au (nm)	R min (%) Eq. 2.10	SPR angle ($^\circ$) Eq. 2.5	R min (%) COMSOL	SPR angle ($^\circ$) COMSOL	Abs. error R (%)	Abs. error SPR angle ($^\circ$)
30	35.11	77.20	34.73	77.50	0.39	0.30
35	17.39	77.80	17.88	77.95	0.49	0.15
40	4.43	78.40	4.47	78.55	0.04	0.15
45	0.04	79.00	0.01	79.05	0.02	0.05
50	5.00	79.60	5.35	79.55	0.35	0.05
55	16.77	80.00	17.77	79.95	1.00	0.05
60	31.40	80.20	33.14	80.20	1.74	0.00
65	45.69	80.40	45.67	80.45	0.01	0.05



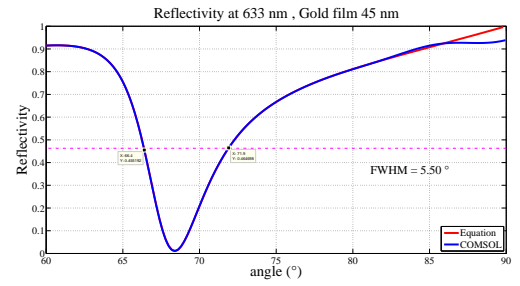
(a)



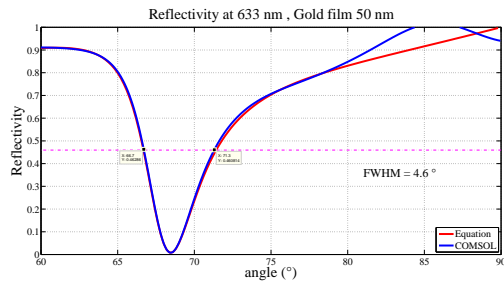
(b)



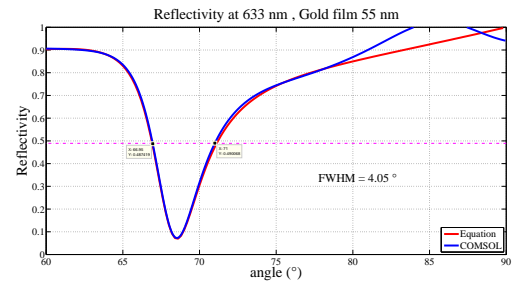
(c)



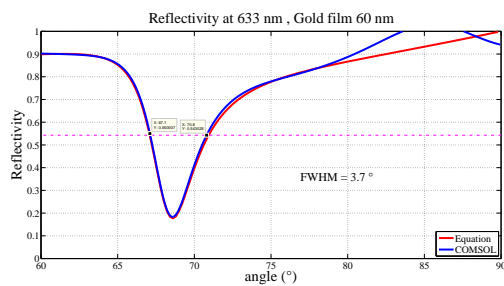
(d)



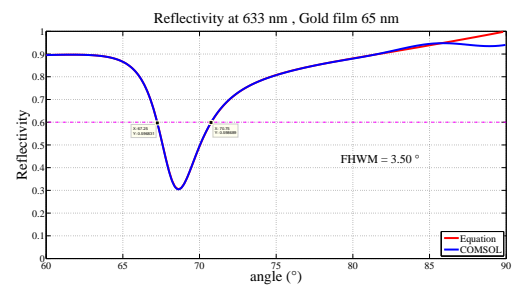
(e)



(f)



(g)



(h)

Figure 4.2: Reflectivity for different thickness of gold film layer, prism $n_p = 1.55$.

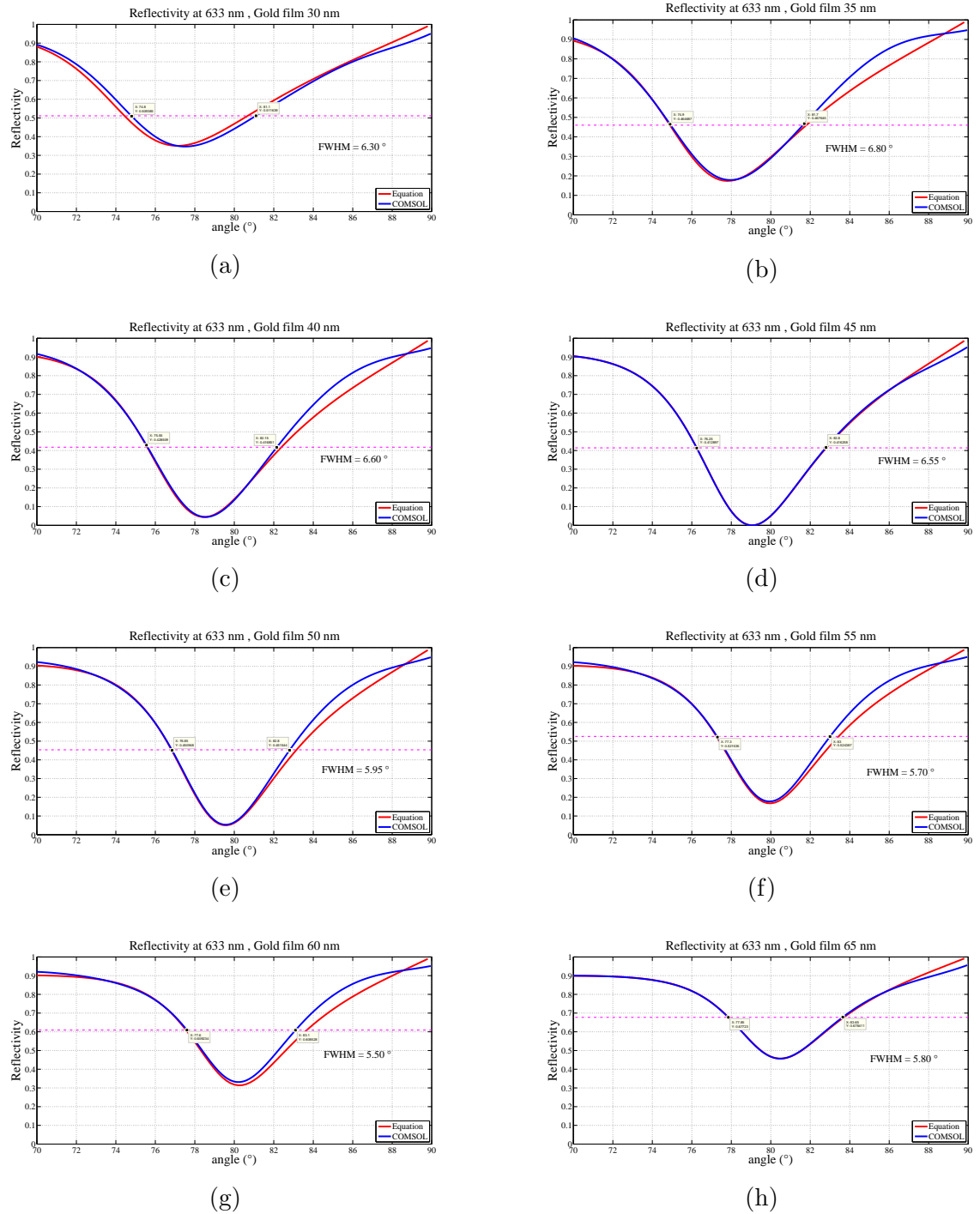


Figure 4.3: Reflectivity for different thickness of gold film layer, prism $n_p = 1.46$.

To obtain a maximum sensitivity in the sensor it is desired to have a steep SPR dip curve (minimum pulse width), since it allows for a more accurate determination of the angle of minimum reflectance. The width of the resonance curve is mainly determined by the metal's dielectric constant. A large negative real part and a small imaginary

part, results in narrow resonance curves. Figure 4.4 show the change in the width (Full Width Half Maximum) of the SPR curve as the thickness of the gold metal layer changes for both types of prism. As seen for both, the width decrease (or steepness increases) with the thickness, however as seen in figure 4.5 the reflectivity is at a minimum at 50 nm and 45 nm for $n_p = 1.55$ and $n_p = 1.46$ respectively, thus these dimensions are taken as the optimal deposition thickness for each interface.

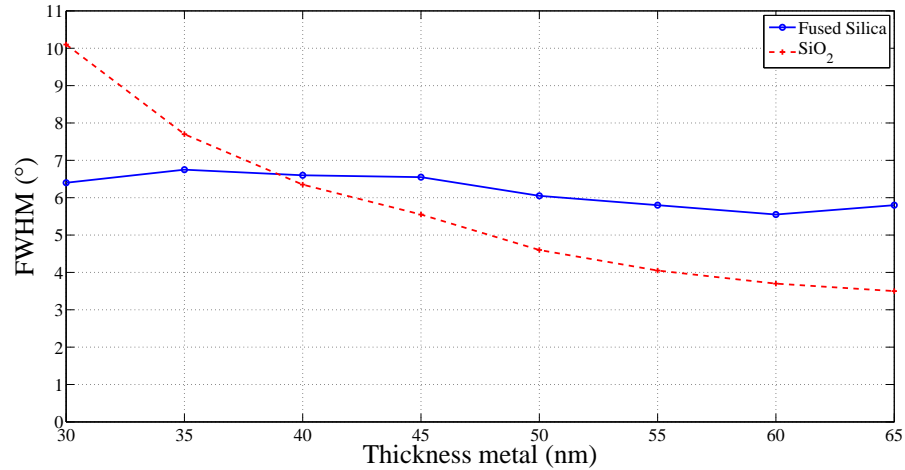


Figure 4.4: FWHM variation with gold layer thickness.

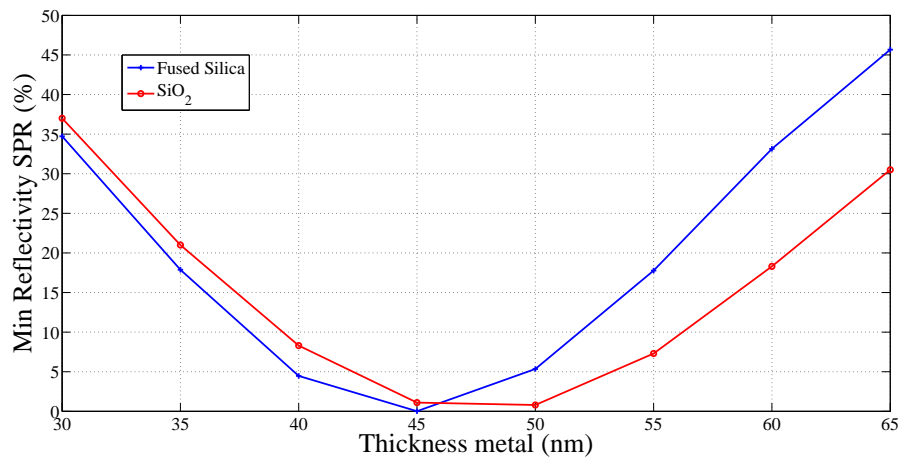


Figure 4.5: Minimum in reflectivity for different Au metal thickness.

4.3 Sensitivity

The minimum detectable change is related to the resolution of the SPR biosensor. For both types of prisms, this variation was simulated on COMSOL with a quad mesh of 6900 elements and 28072 degrees of freedom, where in order to detect the small angle

change a better angle resolution is needed. In this case, a sweep of 0.005° in the incidence angle was made, and with a change in the refractive index of dielectric medium of 10^{-4} RIU. The results are presented in table 4.4 and figures 4.6 and 4.7, where it is observed how from one value of the refractive index to the next, the change in the position of the SPR angle is approximately 0.01° , e.g. from $n_d = 1.3298$, where the position of the SPR angle is 68.435° for $n_p=1.55$, and 79.000° for $n_p=1.46$; to $n_d = 1.3299$, where the position of the SPR angle is now 68.445° for $n_p=1.55$, and 79.010° for $n_p=1.46$.

At the photodetector, Δn_d is observed as a change in the reflectivity, with $\Delta R = 0.08\%$. The sensitivity given by the term S_1 in equation 2.2 is equal to $\Delta R/\Delta n_{eff} \approx 8$ RIU $^{-1}$. Where n_{eff} is given by equation 2.4 using the gold refractive index from table 4.1 and the varying values of the dielectric's refractive index.

Table 4.4: Minimum reflectivity and SPR angles for different refractive index in the dielectric medium. Prisms of $n_p=1.55$ and $n_p=1.46$.

Dielectric refractive index	SPR angle ($^\circ$)	R min (%)	SPR angle ($^\circ$)	R min (%)
	$n_p=1.55$	$n_p=1.55$	$n_p=1.46$	$n_p=1.46$
1.3298	68.435	0.695	79.000	9.26E-05
1.3299	68.445	0.696	79.010	9.36E-05
1.3300	68.460	0.698	79.030	1.07E-04
1.3301	68.470	0.699	79.055	1.22E-04
1.3302	68.485	0.700	79.075	1.37E-04

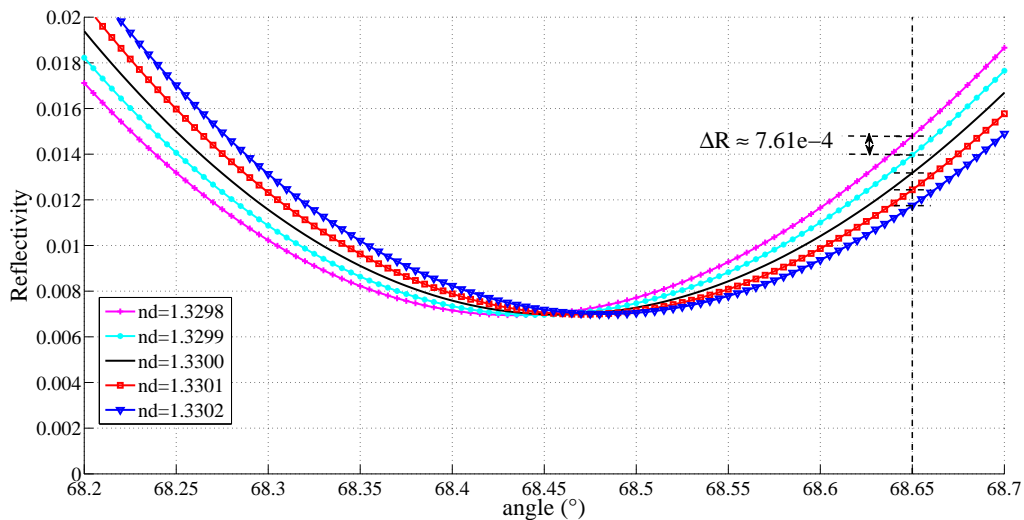


Figure 4.6: Change in SPR angle and reflectivity for $\Delta n_d = 10^{-4}$ RIU at $\lambda=633$ nm. $n_p=1.55$.

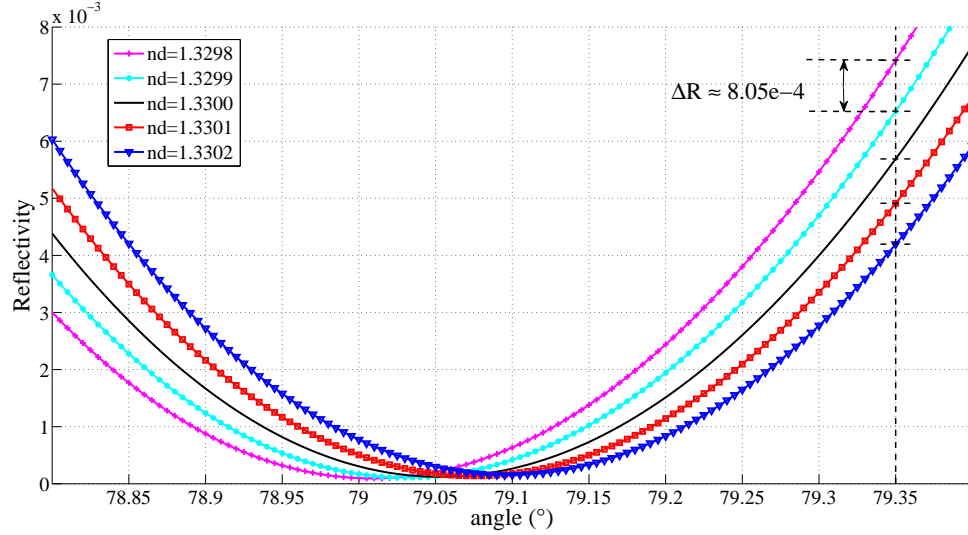


Figure 4.7: Change in SPR angle and reflectivity for $\Delta n_d = 10^{-4}$ RIU at $\lambda=633$ nm. $n_p=1.46$.

4.4 Titanium adhesion layer

The deposition of gold on a glass substrate is commonly done through an intermediate layer to improve adhesion. Titanium is preferred over other metals such as chromium, since the former is less absorbing and less prone to variations during deposition[16]. To observe the effect of the inclusion of the Ti layer, simulations were performed with a quad mesh of 6900 elements and 28072 degrees of freedom and angle resolution of 0.01° , the results for both prisms are shown on table 4.5, figure 4.8 and figure 4.9. As expected, no Ti layer results in a smaller reflectivity; i.e. higher coupling efficiency. Therefore, by increasing the thickness of the Ti layer, a larger minimum reflectivity is experienced at the photodetector, due to the addition of this extra layer. As seen in both figures, the thinner the adhesion layer, the coupling efficiency is higher, in addition an increase in the SPR angle position is experienced with increased Ti thickness. A tradeoff was made between the technical difficulties of depositing thinner metal films. A Ti layer of 5 nm thick is selected, where the minimum reflectivity at the SPR angle for the prism with $n_p = 1.55$ increases from 0.81% to 3.2% for and for the prism with $n_p = 1.46$ it increases from 0.01% to 2.8%.

Table 4.5: Minimum reflectivity and SPR angles for different titanium adhesion layers for $n_p = 1.55$ (Au thickness 50 nm) and $n_p = 1.46$ (Au thickness 45 nm).

Thickness Ti (nm)	SPR angle ($^\circ$)	R min (%)	SPR angle ($^\circ$)	R min (%)
	$n_p = 1.55$	$n_p = 1.55$	$n_p = 1.46$	$n_p = 1.55$
0	68.45	0.81	79.05	0.01
2	68.55	1.56	79.20	0.60
4	68.60	2.61	79.40	1.92
5	68.65	3.21	79.50	2.80
10	68.80	6.44	79.90	8.67
15	69.00	9.69	80.30	15.53

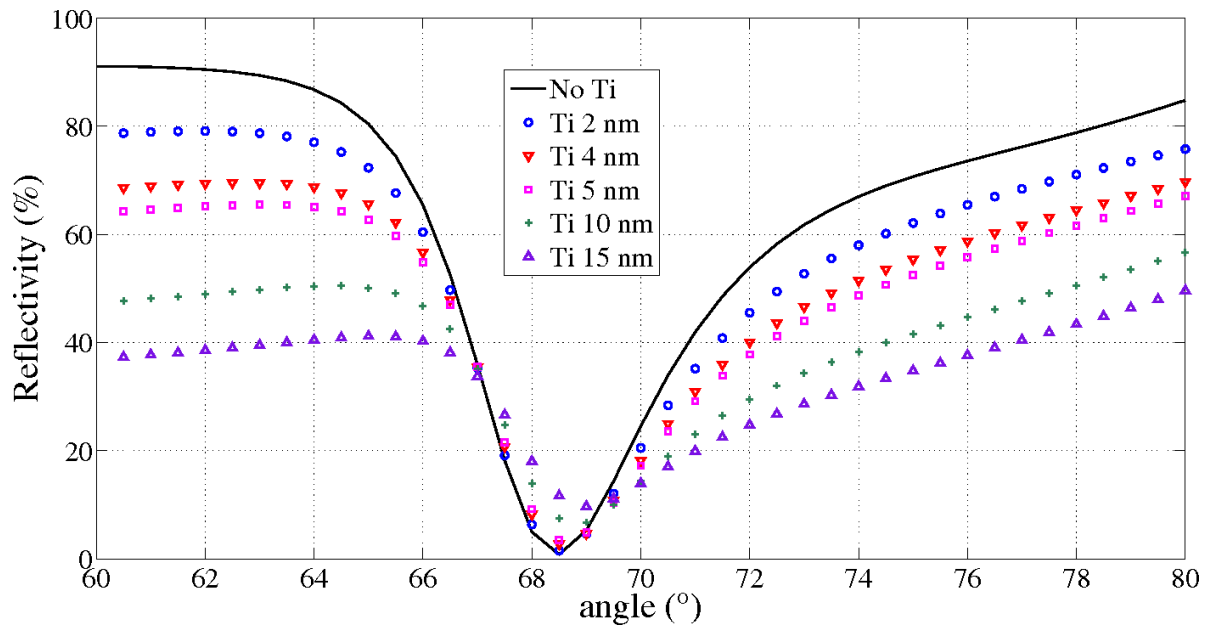


Figure 4.8: Reflectivity change for different Ti layer thickness, Au 50 nm, $\lambda=633$ nm. Prism $n_p = 1.55$.

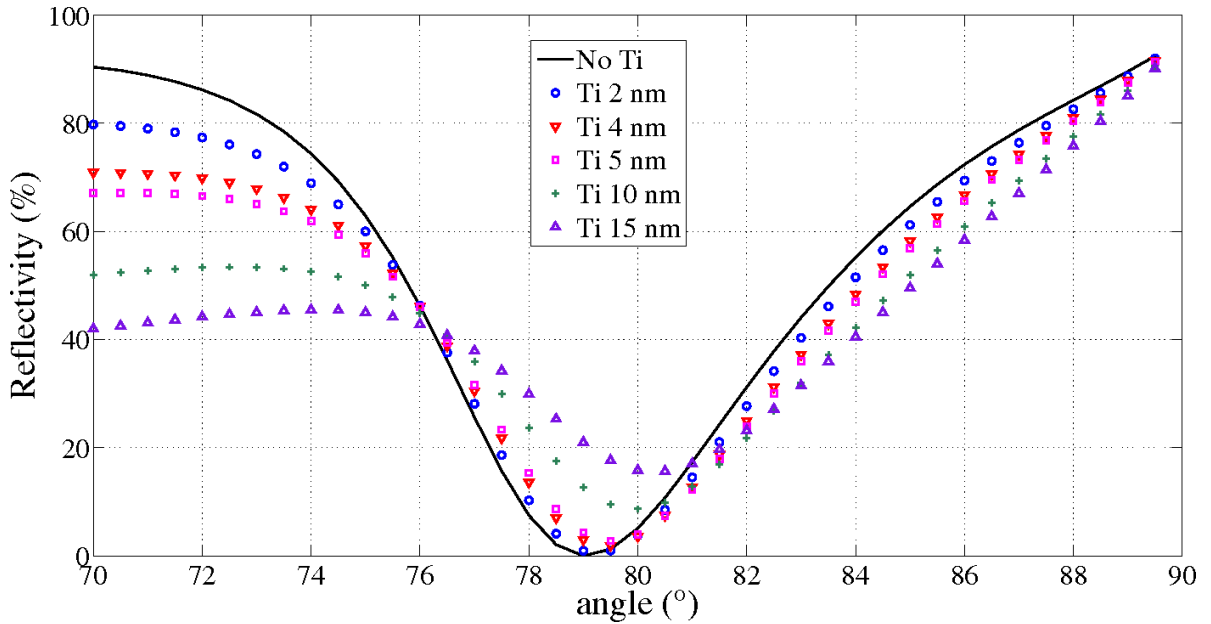


Figure 4.9: Reflectivity change for different Ti layer thickness, Au 45 nm, $\lambda=633$ nm. Prism $n_p = 1.46$.

4.5 Conclusions

In this chapter, simulations for a SPR interface, with the materials selected with miniaturization in mind, were performed. For a post-CMOS compatible gold layer, an optimal thickness of 50 nm thick was found at an incidence angle of 68.46° for a SiO_2 prism with refractive index of 1.55, where a minimum of approximately 1% of the light is reflected. On the other hand, for a fused silica prism, at resonance a minimum of 0.01% in the reflected light is observed, for an Au thickness of 45 nm and incident angle of 79.05° . A comparison with the results predicted by Fresnel equations on a multilayer system show good agreement on the conditions at which plasmon resonance is produced. Simulations also show that changes in the refractive index of 10^{-4} RIU, are reflected as a change in the resonance angle of 0.01° , for which a change of 0.08% in the reflected light is observed at the photodetector for both types of prisms. Finally, when a Ti adhesion layer is included, an increase to 3.2% and 2.8% in the reflectivity at the SPR angle is obtained for the prism with refractive indexes of 1.55 and 1.46 respectively, slightly reducing the dynamic range of the images taken by the photodetector. The results obtained in this chapter will facilitate the experimental testing on a SPR array, where a first set-up will consist of:

- Fused-Si prism of refractive index 1.46.
- Gold layer of thickness 45 nm.
- Titanium adhesion layer of thickness 5 nm.

- Aqueous solution of refractive index 1.33.
- Red light source $\lambda = 633$ nm.

In addition, by knowing beforehand the conditions at which resonance is encountered, the performance of the SPR sensor and the imager specifically designed for this application can be maximized by operating at the region where the optimal SPR response is obtained. Furthermore, the developed program facilitates the introduction of additional materials and light sources, according to the needs of the particular SPR-biosensor.

Chapter 5

Design of CMOS Imager for SPR-Biosensors

With the main benefits of CMOS image sensors being their better capacity for integration with processing circuitry, the design of a custom-made CMOS imager represents the possibility of incorporate application-specific functions such as the selection of region of interest in the photodetector (windowing); synchronization in the acquisition process with the excitation of the SPR, and the processing of the coupling angle [49]; the observation of transitory phenomenon in the SPR signals [41]; and the possibility of real-time, on-chip processing in SPR imaging biosensing, where a reference frame is subtracted to the current frame in order to detect the changes in intensity due to the biological interactions. In this chapter, the design of the proposed 32×32 -pixel CMOS imager with Active Column Sensor (ACS) prototype is presented. First in section 5.2, the selection of the photosensing element in the pixel is evaluated with the use of the computer aided design software Silvaco, where the structures of n-diff/p-sub and n-well/p-sub CMOS photodiodes are simulated, obtaining parameters such as spectral response and generated photocurrents. The photodiode simulations show a better response for the n-well/p-sub structure, from which this device is selected as the photosensing element in the imager pixel. In section 5.3 the design of an Active Column operational amplifier is described. Section 5.4 presents the readout circuits implementing NCDS and DDS. Finally, the global output circuit, including the design of the output operational amplifier, is presented.

5.1 CMOS Image Sensor Prototype

The block diagram of the complete CMOS Active Column Sensor prototype is shown in figure 5.1. The ACS consist of a 32×32 -pixel array with active column circuits, column sample-and-hold circuits, output circuit and the decoders to access and read the matrix. The control and bias signals, and the chip's output ADC are performed externally, which provide the flexibility of addressing specific pixels on the matrix and changing the integration time by controlling the duration of the control pulses.

The prototype building blocks are (figure 5.1):

- 32×32 -pixel Matrix with n-well/p-sub photodiodes.
- ACS readout operation amplifier per column.
- Double Sampling (Non-Correlated) circuit per column.
- Delta Double Sampling (DDS) per column.
- Global output circuit.
- Row Select, Reset and Column Select access decoders.
- External control signals, providing flexibility to scan a particular region of the matrix (windowing) and to control the integration time.

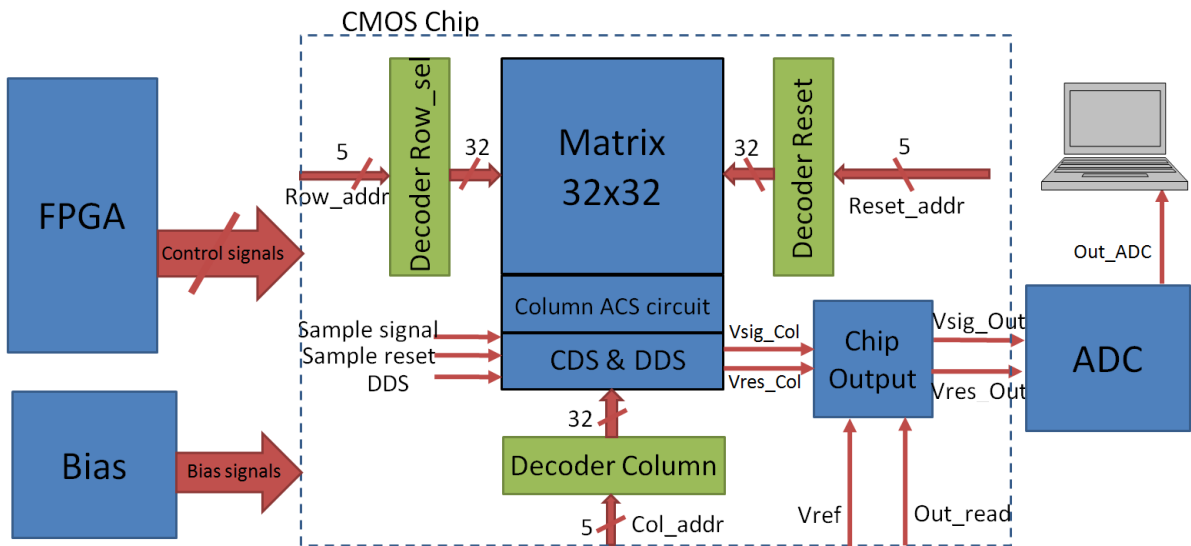


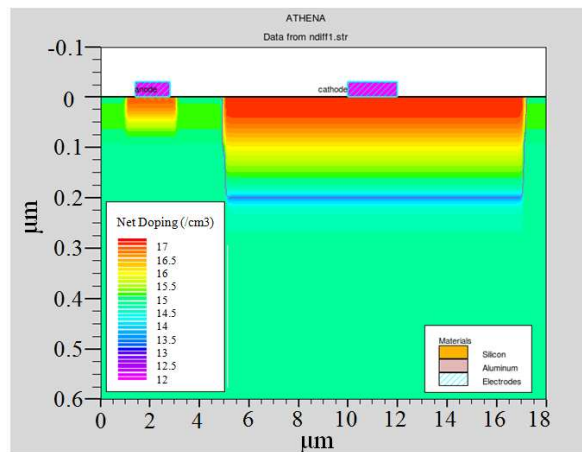
Figure 5.1: Block diagram of CMOS imager with ACS and test card.

5.2 CMOS Photodiode modeling

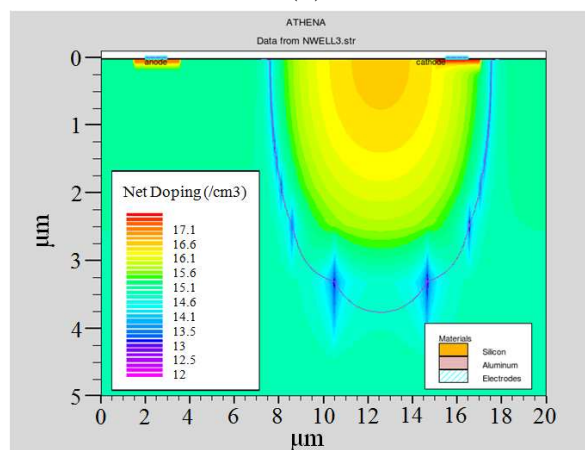
As a first step in the design of the CMOS imager, the photo-sensing element in the pixel is selected based on simulations performed with the TCAD (Technology Computer Aided Design) tools from the company Silvaco. This software is used for 2D and 3D analysis of semiconductor devices. Athena provides the capability to develop and optimize semiconductor manufacturing processes, such as CMOS. Atlas is used to simulate and predict the electrical behaviour of a specified semiconductor structure, and provide information about the internal physical mechanisms associated with device operation. Some of the available physical models in ATLAS are: DC, AC small-signal,

drift-diffusion transport models, energy balance and hydrodynamic transport models, optoelectronic interactions with general ray tracing, general circuit environments, stimulated emission and radiation, Fermi-Dirac and Boltzmann statistics, advanced mobility models, heavy doping effects, full acceptor and donor trap dynamics, SRH, radiative, Auger, and surface recombination [50].

With Athena the structures of the n-diff/p-sub and n-well/p-sub photodiodes are constructed, following the standard CMOS fabrication process steps (implantation, deposition, diffusion, etching), with the concentration levels, sheet resistance, n+ and p+ diffusions junctions depth, and n-well junction depth as specified in the AMS 0.35 μm process parameters document [33]. The 2D structures are shown on figure 5.2 both having a width of 20 μm , with the resulting currents (dark current and photo-current) given in units of $A/\mu m$. The total current can be obtained by multiplying the result by the depth of the pixel in the z-direction. For example, if the pixel size is 20 $\mu m \times 20 \mu m$, an estimation of the dark current is made by multiplying the sum of the diffusion and recombination currents by 20.



(a)



(b)

Figure 5.2: SILVACO structure of CMOS photodiodes. (a) n-diff/p-sub, (b) n-well/p-sub.

5.2.1 Dark current estimation

The first simulations are aimed at obtaining the dark current of the photodiodes. This value cannot be obtained directly due to the limitations in numerical precision of the software. This is due to the fact that internal scaling allows measurements of currents from 10^{-12} A/ μm to 10^{-16} A/ μm , but the diode reverse bias leakage currents can fall below this level, thus introducing uncertainty to the results. To overcome this issue, it is considered that under reverse bias, the diode's behaviour is dominated by the diffusion current in the neutral regions, and recombination inside the depletion zone [50, 51] (regions 2 and 1 respectively in figure 3.1). Both quantities can be estimated with Silvaco Atlas. For the recombination current, the total recombination rate is obtained through simulation, then by multiplying the resulting value by the electron charge (1.6023×10^{-19} C) the recombination current component of the dark current is estimated. Table 5.1 shows the obtained recombination rates and corresponding currents for different reverse bias voltages and donor and acceptor recombination lifetimes $\tau_p = 7 \times 10^{-6}$ s and $\tau_n = 10^{-5}$ s.

Table 5.1: Recombination rates and currents for n-diff/p-sub and n-well/p-sub photodiodes

V_{bias} (V)	n-diff/p-sub		n-well/p-sub	
	rec. rate ($\text{s}^{-1} \cdot \mu\text{m}^{-1}$)	rec current (fA/ μm)	rec. rate ($\text{s}^{-1} \cdot \mu\text{m}^{-1}$)	rec current (fA/ μm)
-0.1	7.905×10^3	1.266	9.040×10^4	14.483
-0.5	2.522×10^4	4.041	3.056×10^5	48.958
-1.0	4.114×10^4	6.592	5.489×10^5	87.947
-2.0	6.434×10^4	10.308	8.545×10^5	136.909
-5.0	1.136×10^5	18.205	2.008×10^6	321.744

For the diffusion current, the dependency on the temperature is considered according to the following formula:

$$I = \exp\left(\frac{-E_g}{K_B T_L}\right) \left[\exp\left(\frac{qV}{K_B T_L}\right) - 1 \right]. \quad (5.1)$$

Where E_g is the bandgap, T_L the operating temperature, K_B Boltzmann's constant, V the bias voltage and q the electron charge. In Atlas the normal operating temperature is set to 300 K, and as the temperature increases so does the current. Thus, a way to eliminate the numerical precision issues is to perform the simulation setting the temperature to 450 K, while leaving the bandgap unchanged ($E_g=1.12$ eV for silicon). The resulting current at 450 K is then used to calculate the current, at an operating temperature of 300 K, according to the following relationship:

$$I = I_e \cdot \exp\left(\frac{E_g}{K_B T_e} - \frac{E_g}{K_B T_L}\right) \cdot \left[\frac{\exp\left(\frac{qV}{K_B T_L}\right) - 1}{\exp\left(\frac{qV}{K_B T_e}\right) - 1} \right]. \quad (5.2)$$

Where T_e is the elevated temperature of 450 K, I_e is the current at T_e . Finally the dark current can be estimated by adding the diffusion and recombination contributions. Table 5.2 presents the diffusion currents obtained for both types of analyzed photodiodes.

Table 5.2: Diffusion currents at T=300 K for n-diff/p-sub and n-well/p-sub photodiodes

V_{bias} (V)	n-diff/p-sub		n-well/p-sub	
	I_e (pA/ μm)	I (fA/ μm)	I_e (pA/ μm)	I (fA/ μm)
-0.1	0.124	0.070	0.270	0.442
-0.5	0.174	0.093	0.381	0.204
-1.0	0.209	0.112	0.455	0.243
-2.0	0.262	0.140	0.526	0.282
-5.0	0.378	0.202	0.780	0.417

The total dark current is then obtained by adding the recombination and diffusion contributions, figure 5.3 shows the resulting dark currents for the n-diff/p-sub and n-well/p-sub photodiode for different bias voltages, where it can be observed how for the n-diff/p-sub photodiode the dark current density is significantly lower. However, important characteristics such as efficiency, photocurrent and conversion gain must be taken into consideration.

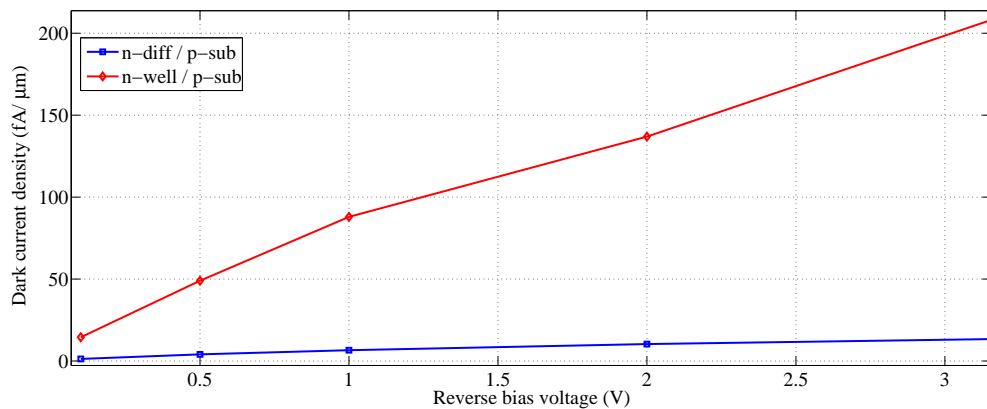


Figure 5.3: Estimated dark current density for n-diff/p-sub and n-well/p-sub

5.2.2 Spectral response estimation

The spectral response is obtained by defining an incident light beam in Atlas, specifying its incident angle, wavelength, intensity in W/cm^2 . Once the characteristics of the incident light are known, the method to solve the propagation is defined, the available methods are: ray tracing, transfer matrix method, beam propagation method (BPM) and finite difference time domain (FDTD). In this case BPM is used, defining a wavelength sweep from 100 to 1000 nm (covering the visible spectrum) and a beam of $1 \text{ W}/\text{cm}^2$. This intensity is a default value, with the important fact being that both photodiodes receive the same amount of incident power, so a comparison can be established. The software will return three quantities: source current, available current and cathode (contact) current.

The source current is a measure of the rate of photons incident on the photodiode. The available photocurrent is a measure of the photon absorption rate in the device, this value is slightly less than the source photocurrent, due to reflection and transmission losses from the device structure. Finally the cathode current is the current collected at the contact. The currents obtained for n-diff/p-sub, and n-well/p-sub photodiodes are shown on figures 5.4 and 5.5. As seen for the n-well/p-sub we obtain a higher photocurrent with a peak at a wavelength of 700 nm as expected from the optical absorption characteristics of silicon. If the incident power changes the response changes proportionally, with the n-well/p-sub always having a higher photocurrent. For the operating wavelength of 633 nm, the n-well/p-sub produces a 85 nA photocurrent, as opposed to 25 nA for the n-diff/p-sub.

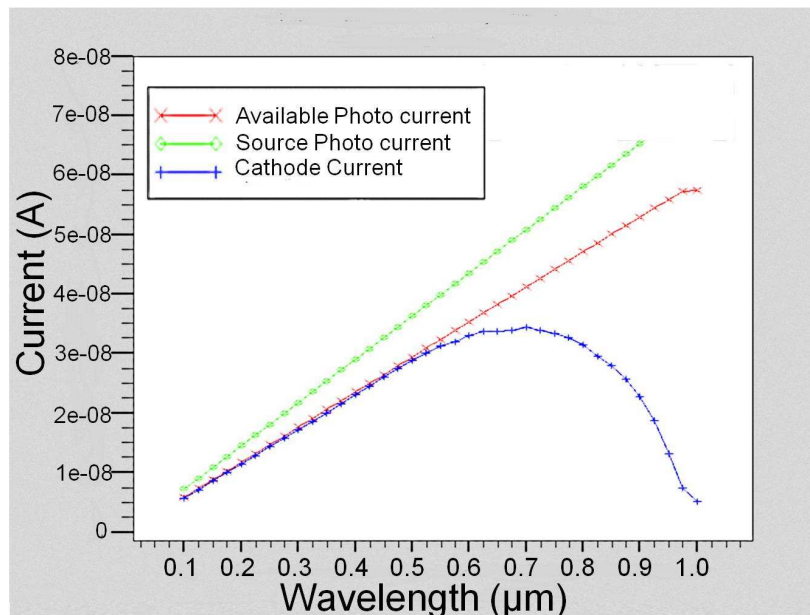


Figure 5.4: Simulated currents, n-diff/p-sub photodiode

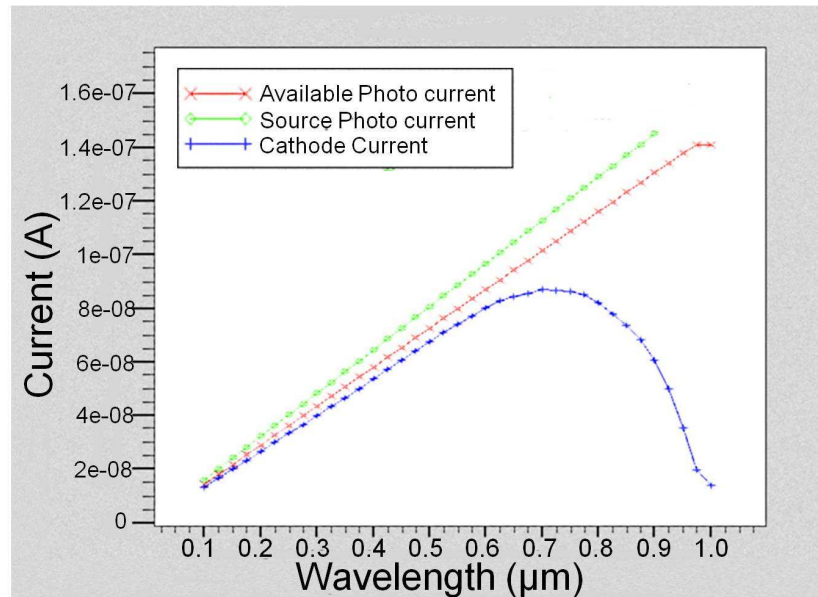


Figure 5.5: Simulated currents, n-well/p-sub photodiode

5.2.3 Quantum efficiency

We are interested in the quantum efficiency of the device. This is obtained by dividing the available photocurrent by the source photocurrent. Figure 5.6 presents the resulting quantum efficiency for the n-diff/p-sub and n-well/p-sub photodiodes. It is observed that for the latter a higher efficiency is obtained. However, it is important to mention that since the simulated structures don't cover the upper CMOS layers, in reality the overall quantum efficiency of the sensor will be reduced.

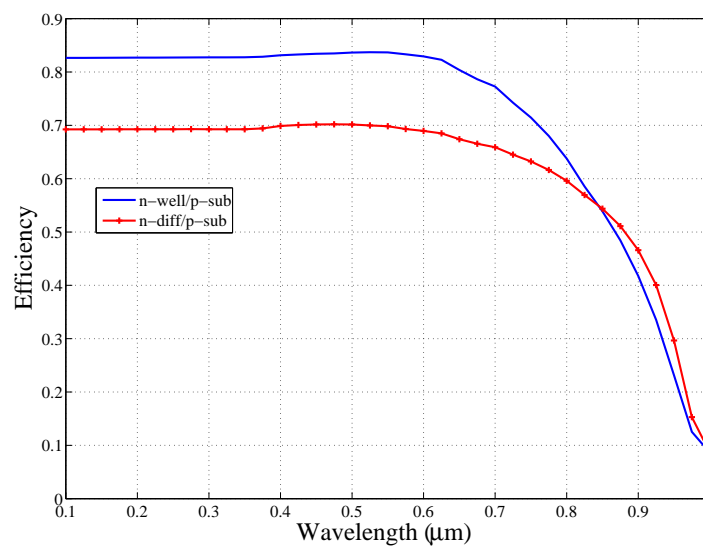


Figure 5.6: Quantum efficiency. (a) n-diff/p-sub; (b) n-well/p-sub

5.2.4 Photodiode's junction capacitance

Another important characteristic of the photodiode is the junction capacitance. From section 3.3 it is seen that the conversion gain is inversely proportional to the capacitance, thus a lower value is desired in order to maximize this conversion gain. In principle we expect the n-diff/p-sub to have a larger junction capacitance, as mentioned on section 3.1.1. From equation 3.12, it is observed how this value can be obtained from the AMS 0.35 μm process parameters document [33]. An alternative method to obtain the photodiode's capacitances is to use the AMS 0.35 μm kit on Cadence and perform a transient simulation varying the applied reverse voltage at the photodiode node, where a nftdiode represents the n-diff/p-sub and a nwd diode being the n-well/p-sub.

Remembering that for AC the electrical impedance is $V = I \cdot Z_c$ and $Z_c = 1/2\pi fC$ being the capacitive reactance. Taking the AC source frequency as $f = 2$ KHz with amplitude $V = 1$ mV, the capacitance for both photodiodes can be obtained from equation 5.3 and the results for the diode currents. Figure 5.7 shows the resulting cadence electrical simulation curves for both photodiodes, clearly observing the lower capacitance of the n-well/p-sub for all voltages.

$$C = \frac{I}{2\pi V \cdot f} \quad (5.3)$$

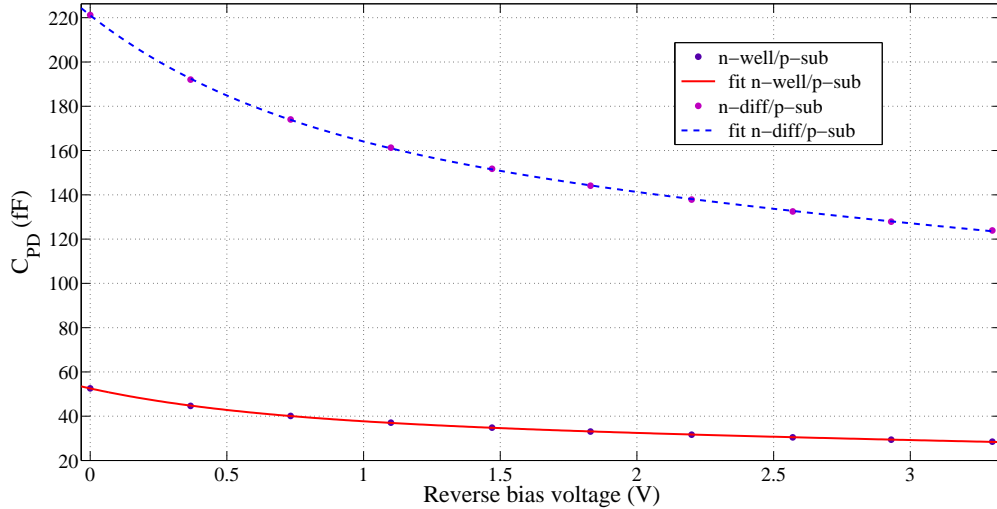


Figure 5.7: Cadence electrical simulation results. N-well/p-sub (solid) and n-diff/p-sub (dashed) junction capacitance vs. applied voltage.

The n-diff/p-sub photodiode is constructed as a n+ region in a p-substrate, while the n-well/p-sub is constructed with a n-well layer over the p-substrate. Following these basic structures, the layouts for pixels using both type of photodiodes are shown on figure 5.8. The layout view contains only the physical characteristics of the pixel, from here the extracted view is obtained, containing the devices and connectivity information. As

seen in the right side of figure 5.8, where the n-diff/p-sub photodiode is represented as a nftdiode and the n-well/p-sub as a nwd photodiode. Considering the dimensions of the pixel are $20 \times 20 \mu\text{m}^2$ the extracted photodiode dimension are used to obtain the areas and perimeters of both devices. Based on its higher photocurrent, higher efficiency and lower junction capacitance, n-well/p-sub photodiodes are selected as the photosensing element in the prototype 32×32 -pixel matrix.

Table 5.3: Extracted view geometrical characteristics and junction capacitances for n-diff/p-sub and n-well/p-sub photodiodes.

Photodiode	Area (μm^2)	Perimeter (μm)	$I_{simulation}$ (pA)	Capacitance (fF) at 2.4 V	Fill Factor (%)
n-diff/p-sub	237	63	1.55	135.0	59.2
n-well/p-sub	244	64.3	0.358	31.0	61.0

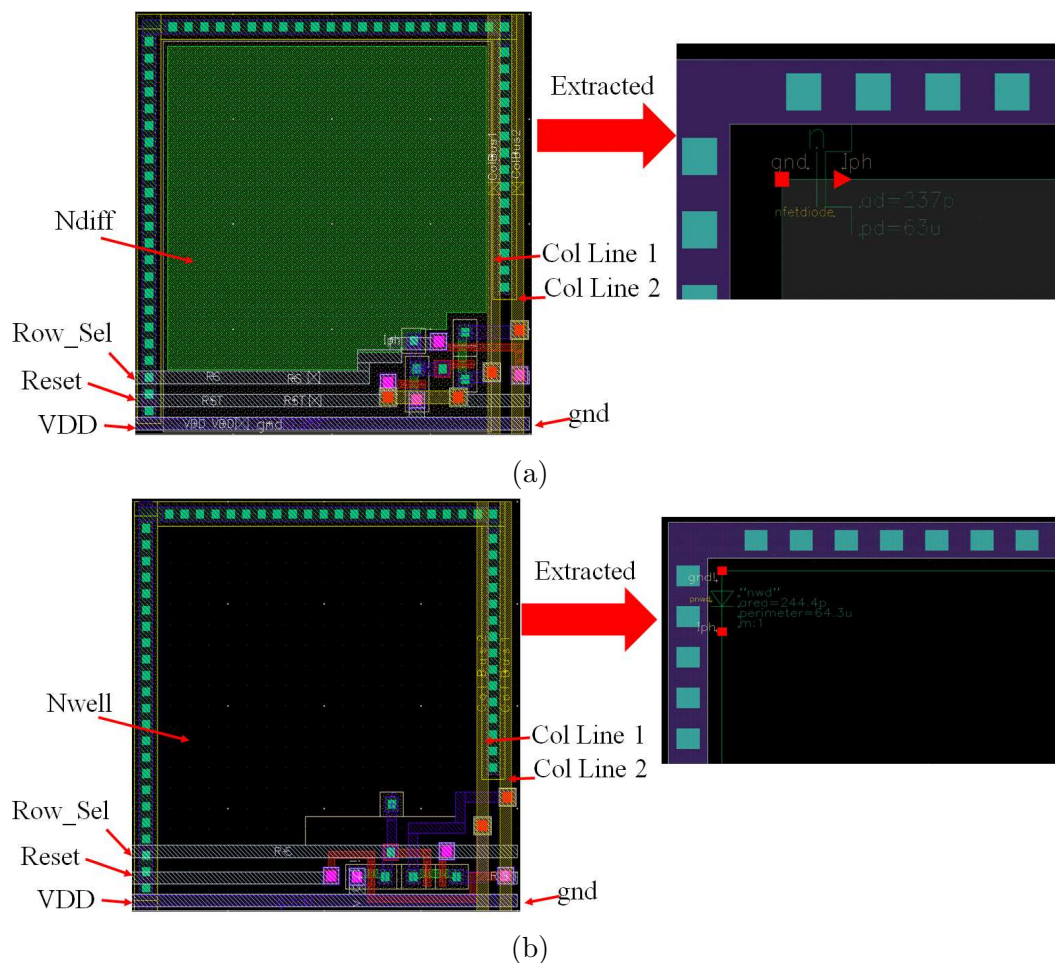


Figure 5.8: Virtuoso Cadence Pixel's layouts. The extracted view (right) gives the photodiode's area and perimeter (a) n-diff/p-sub, (b) n-well/p-sub.

5.3 Active Column Sensor

The active column sensor amplifier shown on figure 3.14 is based on a simple one-stage amplifier in voltage follower configuration. In the present work, the ACS amplifier is extended to a two-stage op-amp, which is useful in some applications where the gain and/or the output swings provided by cascode op-amps are not adequate [24]. With a power supply of 3.3 V, it is desired that the output swing covers as much as possible of the range from 0-3.3 V. The amplifier design is limited mainly by the size of the input transistor inside the pixel, where due to the need to maximize the fill factor, all pixels are selected to have minimum dimensions. Another aspect to take into consideration is that due to the column parallel architecture, the half differential pairs in the pixels are connected at the same node, causing capacitive loading of the amplifier, which decreases stability. This issue can be solved with higher capacitive compensation [52].

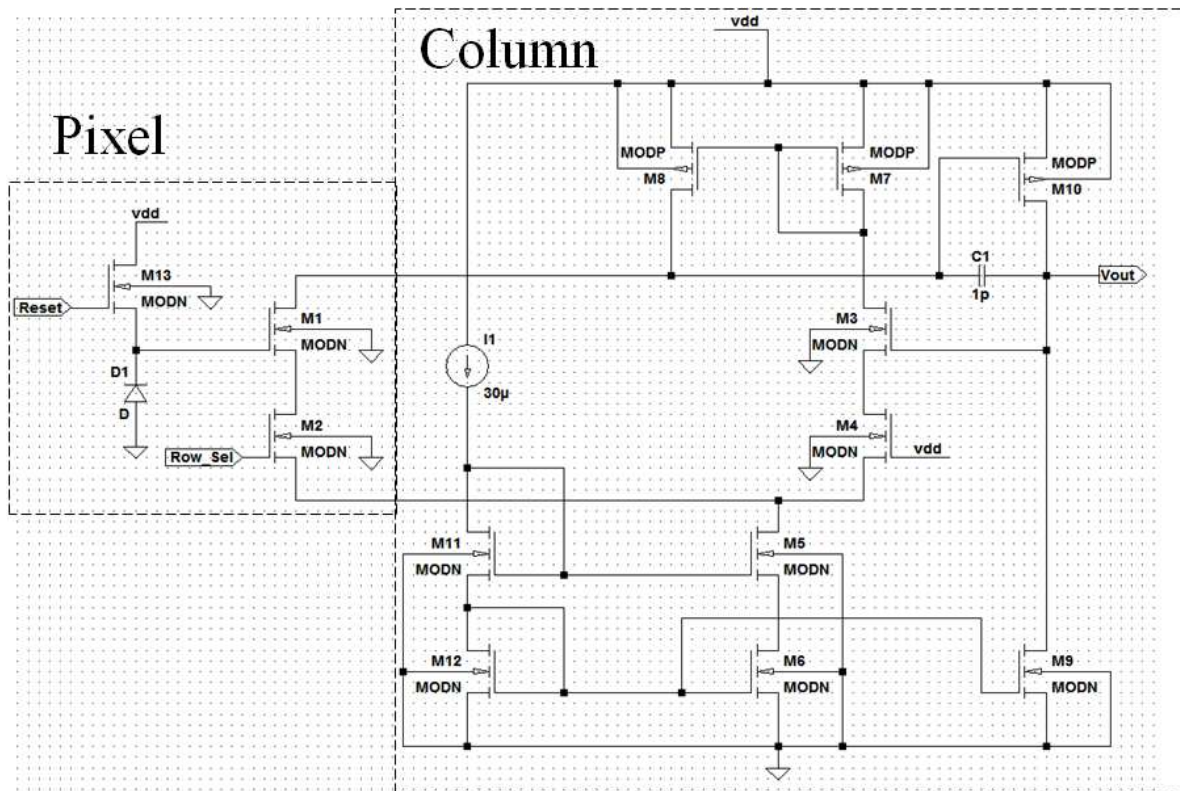


Figure 5.9: Schematic of Active Column Sensor circuit

In the schematic, transistors $M1$ and $M3$ are the differential input, with $M3$ connected to the output in voltage follower configuration. $M2$ is the row select signal, normally not part of a differential amplifier in this case used to activate/deactivate the input pixel. At the column level, $M4$ is added to preserve symmetry and is always biased to VDD. Transistors $M3 - M8$ form the first stage of the op-amp, while transistors $M9 - M10$ are the second stage gain stage (common source amplifier with active load). Capacitor $C1 = C_c$ is the compensation capacitor used to stabilize the op-amp. Transistors $M5, M6, M11$ and $M12$ are arranged as standard cascode current sink that

will bias the differential stage of the amplifier. The design of the amplifier is based on the following specifications:

Table 5.4: Specifications of the ACS amplifier

W1=W2=W3=W4=W13= 0.4 μm
L1=L2=L3=L4=L13= 0.35 μm
0V < ICMR < 3V
$I_5 = I_{Bias} = 30 \mu\text{A}$

The effects of the minimum dimension in the differential pair can be observed from the first stage gain given by:

$$A_{\nu 1} = \frac{-g_{m1}}{g_{ds3} + g_{ds7}}, \quad (5.4)$$

where g_{m1} , g_{ds3} and g_{ds7} are the channel conductances of transistors $M1$, $M3$ and $M7$. The factor $(W/L)_1$ decreases the gain of the first stage. The second stage of the op-amp will help to compensate for this low gain, which has a gain of:

$$A_{\nu 2} = \frac{-g_{m10}}{g_{ds10} + g_{ds9}}, \quad (5.5)$$

Furthermore, parameters such as the slew rate, gain and gain bandwidth at first will be left with some flexibility to adjust to the specification given in table 5.4. The procedure to design the ACS op-amps is described in detail in reference [24]:

1. The slew rate is given by:

$$SR = \frac{I_{Bias}}{C_c} \quad (5.6)$$

Current $I_{Bias} = 30 \mu\text{A}$ is selected considering that increasing it to much will cause the gain of the amplifier to decrease. For the compensation capacitor C_c his value was chosen considering that if the pixel size is $20 \mu\text{m} \times 20 \mu\text{m}$, the width of the column circuits must not exceed $20 \mu\text{m}$, and the larger the capacitor the larger the layout area it will occupy. This and the fact that a smaller capacitance will lead to a larger SR indicates that a smaller value is desired for C_c , however if made too small the phase margin also decreases making the op-amp unstable. Taking this factors into consideration a capacitance of $C_c = 1 \text{ pF}$ is selected. Thus making $SR = 30 \text{ V}/\mu\text{s}$.

2. The maximum common mode voltage $V_{in(max)} = 3.0 \text{ V}$, is selected assuming a maximum reset voltage (V_{GS-M13}) of 3.6 V (according to the process specifications). The soft reset technique used in the pixel means that the photodiode maximum voltage is $V_{reset} - V_{TH}$. That is the maximum input voltage buffered will be appropriately 3.0 V , assuming a 3.6 V reset voltage. This maximum voltage is limited by

the differential-pair going into the linear region, thus to keep them in saturation it is required that:

$$V_{D1,3} \geq V_{G1,3} - V_{THN}. \quad (5.7)$$

And,

$$V_{D1} = V_{DD} - V_{SG8}. \quad (5.8)$$

Thus,

$$V_{G1} \leq V_{DD} - V_{SG8} + V_{THN}. \quad (5.9)$$

Remembering that for a PMOS in saturation, without channel modulation, the drain current is given by:

$$I_D = K'_P \frac{W}{2L} (V_{SG} - V_{THP})^2. \quad (5.10)$$

Substituting eq. 5.10 into 5.9, and knowing that $I_{D8} = I_{Bias}/2$ we have that:

$$V_{G1} \leq V_{DD} - \sqrt{\left(\frac{I_{Bias}}{K'_P}\right) \left(\frac{L}{W}\right)_8} - V_{THP} + V_{THN}. \quad (5.11)$$

Finally, assuming the case where the gate voltage is the maximum input $V_{in(max)}$ we can obtain the dimensions of $M7$ and $M8$ as:

$$\left(\frac{W}{L}\right)_{7,8} = \frac{I_{Bias}}{K'_P [V_{DD} - V_{THP} + V_{THN} - V_{in(max)}]^2}. \quad (5.12)$$

3. The minimum voltage is limited by $M5$ and $M6$ being driven into non-saturation. Together with $M11$ and $M12$ they form a cascode current mirror. To keep both transistors in saturation it can be shown that [53]:

$$V_{D5} > 2\sqrt{\frac{2I_{Bias}}{K'_N(W/L)_5}} + V_{THN}. \quad (5.13)$$

Additionally, to keep $M1$ and $M3$ in saturation,

$$V_{D5} = V_{in} - 2\sqrt{\frac{I_{Bias}}{K'_N(W/L)_1}} - V_{THN}. \quad (5.14)$$

Substituting equation 5.14 into 5.13 it is obtained that:

$$\left(\frac{W}{L}\right)_5 \geq \frac{2I_{Bias}}{K'_N \left[\frac{V_{in}}{2} - \sqrt{\frac{I_{Bias}}{K'_N(W/L)_1}} - 2V_{THN}\right]^2}. \quad (5.15)$$

The sizes of $M5$, $M6$, $M11$ and $M12$ are kept equal.

4. The dimensions of $M9$ and $M10$ are determined considering that:

$$\left(\frac{W}{L}\right)_{10} = \left(\frac{W}{L}\right)_7 \left(\frac{g_{m10}}{g_{m7}}\right). \quad (5.16)$$

Where for a phase margin $>60^\circ$, $g_{m10} = 2.2[g_{m3}(c_L/c_C)]$:

$$g_{m7} = \sqrt{K'_P \left(\frac{W}{L}\right)_7 I_{Bias}}. \quad (5.17)$$

Then,

$$\left(\frac{W}{L}\right)_9 = \left(\frac{I_{10}}{I_{Bias}}\right) \left(\frac{W}{L}\right)_5 \quad (5.18)$$

The sizes of M9 and M10 are adjusted by observing the output swing and adjusting according to the requirements.

Table 5.5 summarizes the first values obtained for the ACS amplifier:

Table 5.5: First approximation ACS amplifier

I_{Bias}	$30 \mu\text{A}$
C_c	1 pF
SR	$30 \text{ V}/\mu\text{s}$
$(W/L)_{1,2,3,4,13}$	$0.4\mu\text{m}/0.35\mu\text{m}$
$(W/L)_{7,8}$	$8.3\mu\text{m}/1\mu\text{m}$
$(W/L)_{5,6,11,12}$	$>0.45\mu\text{m}/1\mu\text{m}$
$(W/L)_9$	$1.5\mu\text{m}/1\mu\text{m}$
$(W/L)_{10}$	$52.6\mu\text{m}/1\mu\text{m}$
Input Common Mode Range	$0\text{V} < \text{ICMR} < 2.9\text{V}$
Single Supply	$\text{vdd}=3.3 \text{ V}, \text{vss}=\text{gnd}$

The design process is iterative, adjusting the transistor dimensions, currents and capacitor have different effects on the characteristics of the op-amp as summarized in table 5.6 [24].

Table 5.6: Dependence of op-amp characteristics

$I_{Bias} \downarrow, I_{10} \downarrow, L_7 \uparrow, (W/L)_{10} \uparrow, L_9 \uparrow$	Increase gain
$I_{Bias} \uparrow, C_c \downarrow$	Increase GB
$I_{10} \uparrow, (W/L)_{10} \uparrow, C_c \downarrow$	Increase RHP Zero
$I_{Bias} \uparrow, C_c \downarrow$	Increase Slew Rate

According to these guidelines table 5.7 presents the final ratios, currents and compensation capacitor for the proposed ACS op-amp.

Table 5.7: Final ACS op-amp parameters

I_{Bias}	30 μ A
C_c	1 pF
$(W/L)_{1,2,3,4,13}$	0.4 μ m/0.35 μ m
$(W/L)_{7,8}$	4.5 μ m/1 μ m
$(W/L)_{5,6,11,12}$	3 μ m/1 μ m
$(W/L)_9$	6 μ m/0.5 μ m
$(W/L)_{10}$	14 μ m/0.35 μ m
Single Supply	vdd=3.3 V, vss=gnd

A series of simulations were performed with the CMOS-AMS 0.35 μ m design kit to obtain the performance characteristics of the ACS op-amp. The open-loop gain, GB, cut-off frequency and phase margin are obtained with a AC analysis with the results shown on figure 5.10.

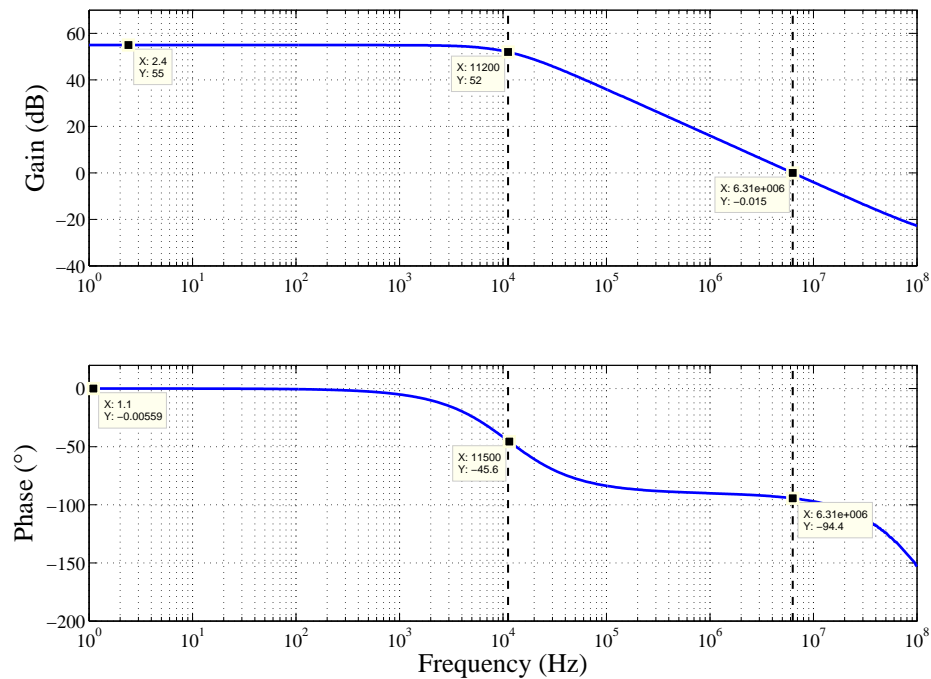


Figure 5.10: ACS simulated frequency response Active Column Sensor

The input common mode range is obtained by setting the op-amp in voltage follower

configuration and sweeping the positive input voltage, the resulting signal shown on figure 5.11:

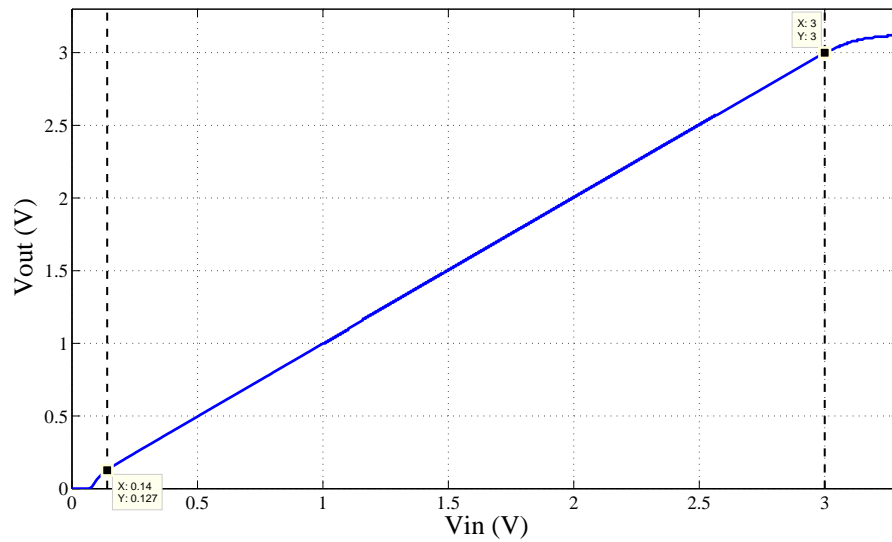


Figure 5.11: ACS simulated Input Common Mode Range (ICMR)

The slew rate is determined from the slope of the output signal when rising applying an input pulse voltage while on voltage follower configuration. Resulting in the following plot:

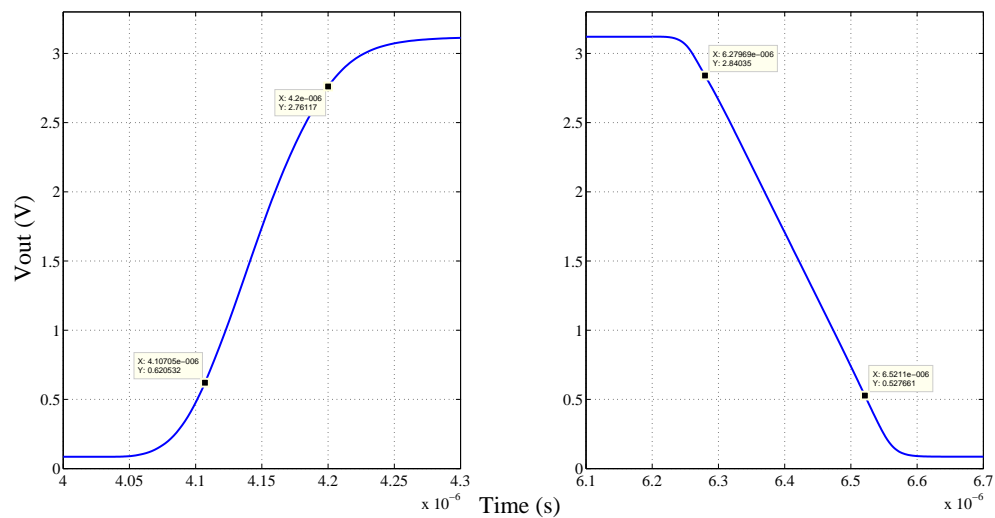


Figure 5.12: ACS simulated positive and negative slew rate

Placing a small AC voltage in series with power supply vdd the power supply rejection ratio (PSRR) can be measured. The PSRR is the product of the ratio of

change in the supply voltage to the change in output voltage caused by this change in the supply. This is shown on figure 5.13.

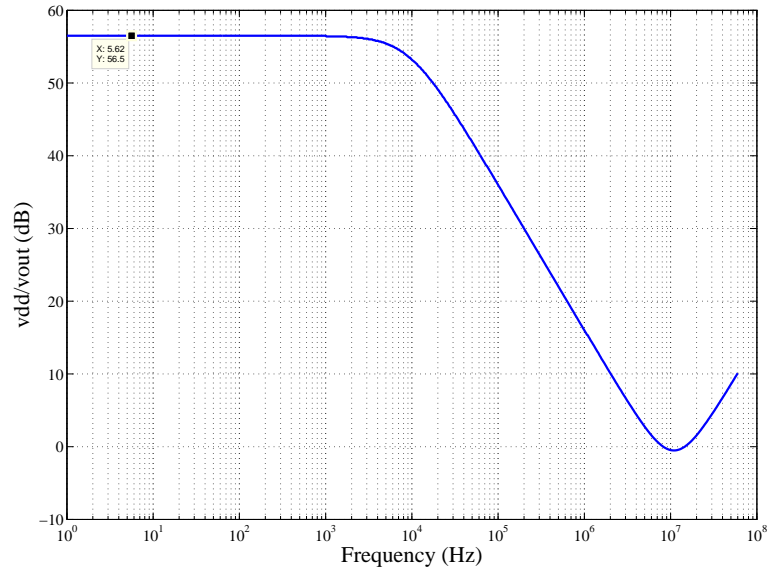


Figure 5.13: ACS simulated power supply rejection ratio

Finally, the common mode rejection ratio is a measure of how the output changes when the common-mode input changes, ideally is zero. CMRR is tested by placing two identical AC sources in at the inputs, with the op-amp in voltage follower configuration. The result of this simulation is shown on figure 5.14.

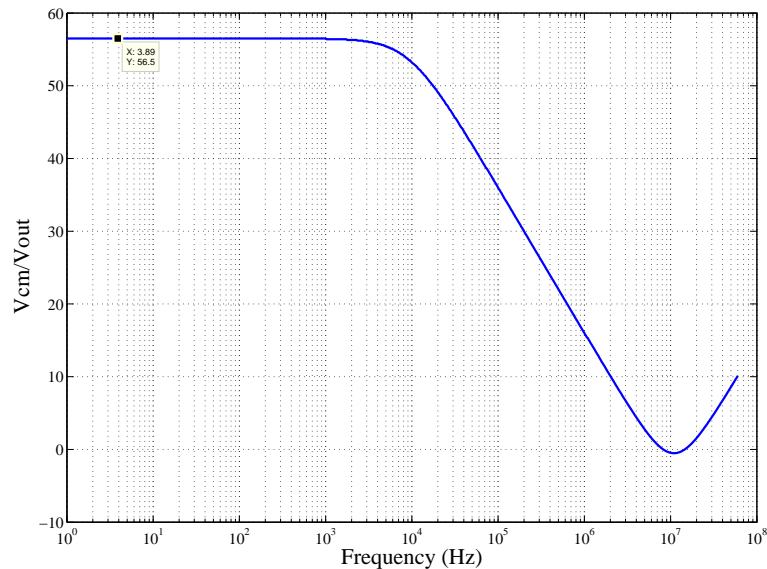


Figure 5.14: ACS simulated common mode rejection ratio

From the previous figures the performance characteristics of the ACS op-amp are summarized on table 5.8.

Table 5.8: Final ACS op-amp performance characteristics

Open loop gain	55 dB
Cut-off frequency	11.2 KHz
Gain bandwidth (GB)	6.31 MHz
Phase margin	85.6°
PSRR	56.5 dB
CMRR	56.5 dB
ICMR	0.15 V - 3 V
Output Swing	0.21 V - 3.1 V
Slew rate (positive)	23.0 V/ μ s
Slew rate (negative)	9.6 V/ μ s
Slew rate (average)	16.3 V/ μ s

The column ACS layout is shown on figure 5.15, where most of the area is occupied by the poly capacitor due to the requirement of keeping the column width to 20 μ m .

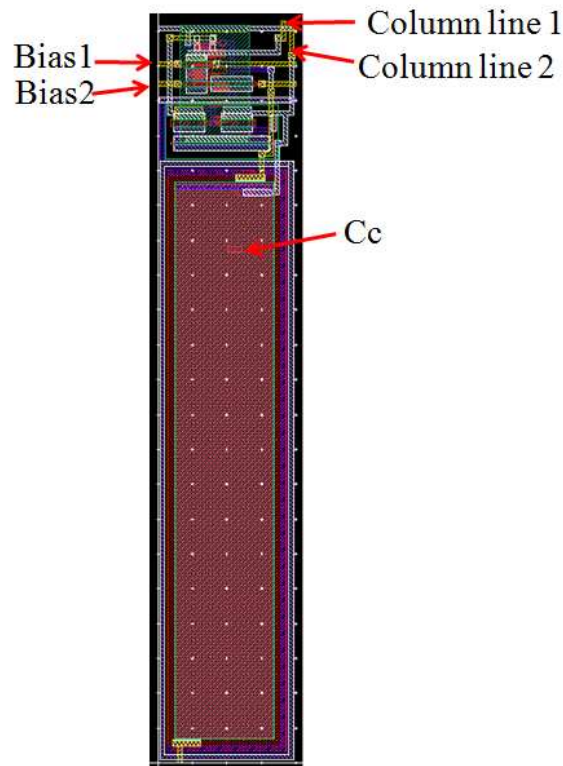


Figure 5.15: Virtuoso cadence ACS circuit Layout

5.3.1 APS vs ACS

To observe the performance of the ACS readout and how it compares with a classical APS architecture with a pixel source follower transistor, a cadence simulation is performed. First it is necessary to define an electrical model associated to the photodiode. For a PN junction photodiode, the simplest model is shown in figure 5.16 [54]. With the value of $C_{junction}$ given in table 5.3.

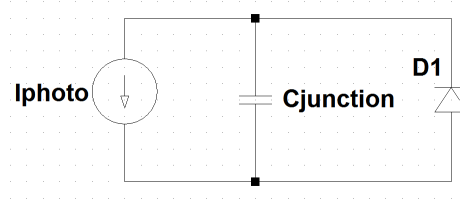


Figure 5.16: Simplified electrical model of a photodiode

It must be noted that during the reset operation, the final value at which the junction capacitance is set depends on the value of the reset pulse. The presence of the NMOS reset transistor will cause that the maximum voltage at the photodiode node to be $V_{Reset} - V_{THN}$, so for example if $V_{Reset} = vdd = 3.3V$ then $V_{PDmax} \approx 2.8V$. One possible solution is to boost the reset voltage to a value larger than the power supply. Figure 5.17 shows how in CMOS-ACS the difference between the photodiode voltage and pixel's output is minimized by greatly reducing the level shifting associated with the SF. Running a Monte Carlo simulation for 500 samples it is observed how the average difference between the pixel's output and the photodiode is null thanks to the ACS configuration. Where the distribution of this difference is caused by the amplitude offset (figure 5.18). At the SPR platform, the improvement of the ACS configuration will be reflected in a larger dynamic range.

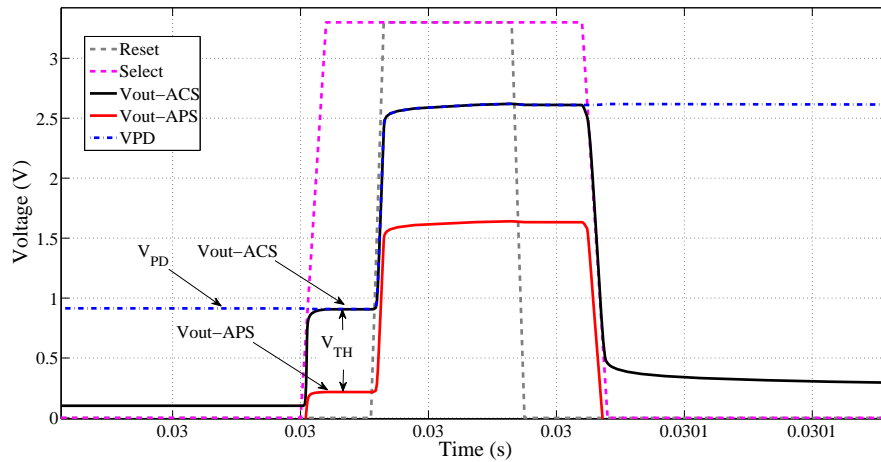


Figure 5.17: Pixel's output for APS and ACS. Integration time 30 ms. $V_{PD} - V_{outACS} = 1.9mV$ and $V_{PD} - V_{outACS} = 0.69V \approx V_{TH}$.

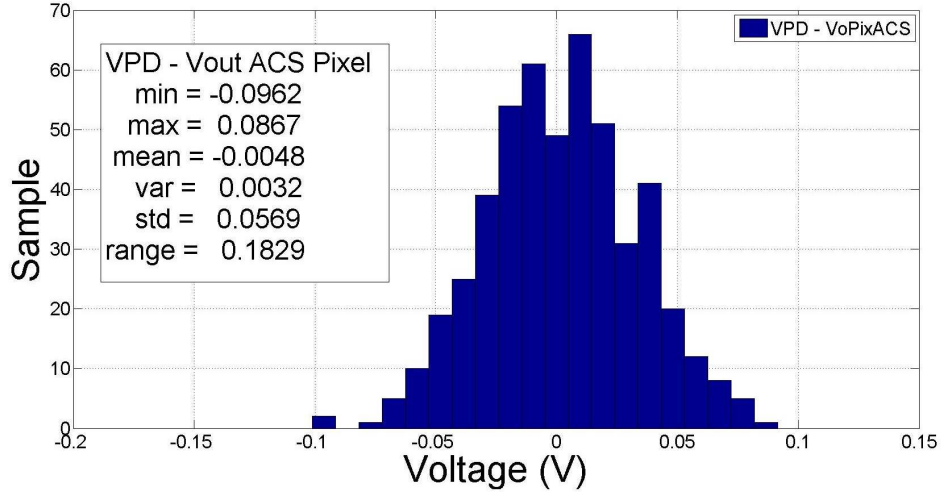


Figure 5.18: Difference between photodiode voltage and Pixel ACS output. 500 sample Monte Carlo simulation

5.4 Column Readout circuits

Two Sample-and-Hold (S/H) circuits per column are required to implement NCDS. The simplest sampling and hold circuit consist of a switch and a capacitor as shown on figure 5.19. In it, when V_{ctl} is high V_{out} will follow V_{in} . When V_{ctl} goes low V_{out} will ideally remain constant at the value that V_{in} has at this instant. An effect to consider for this S/H configuration is that when transistor M1 turns off, the channel charges flow out from the gate into its junctions. At the V_{in} node this has little effect, however at the C_{sh} node this charge transfer will cause a negative voltage change that will last until M1 turns on again. The change associated to this flowing charge is given by [53]:

$$\Delta V_{out} = \frac{C_{ox}WL(V_{dd} - V_{THN} - V_{in})}{2C_{sh}}. \quad (5.19)$$

Where C_{ox} is the capacitance per unit area of the gate oxide. This change is linearly proportional to V_{in} and V_{THN} , the latter which is nonlinearly related to V_{in} . This nonlinear relation ultimately leads to distortion in the overall S/H circuit. This issue is known as charge injection.

To minimize this negative effect, the NMOS switch is replaced with a transmission gate as shown in figure 5.20. The idea behind this configuration is that when the transmission gate turns off the charge injection due to each transistor will cancel each other. Furthermore, transmission gates are used to accommodate greater voltage swings.

To buffer the S/H output at the column level, due to space constraints a PMOS source follower was used. Additionally, the Delta Double Sampling (DDS) technique during a column read cycle is used reduce the column-FPN, where by shorting the sampling capacitors the signal's dispersion at the output can be reduced [29, 55]. The

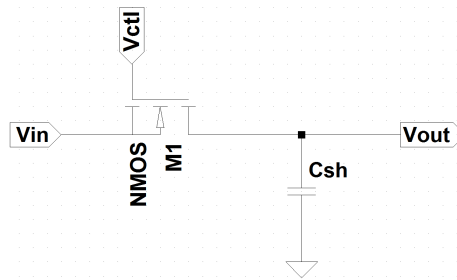


Figure 5.19: Simple CMOS sample and hold circuit

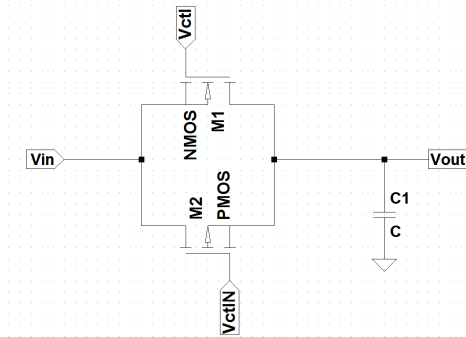


Figure 5.20: Sample-and-Hold circuit using a CMOS transmission gate

NCDS-DDS schematic is shown on figure 5.21 and its layout is shown in figure 5.22.

The two outputs per column are sent to the global output circuit in figure 5.23. It can be noticed that the current load (provided externally) of the columns PMOS-SF can be shared, since only one will be active at one time. The output coupling capacitors are kept at a relatively large value of 12 pF in order to reduce kTC noise and minimize the attenuation of the signal in the capacitive divider at the output stage [56]. The output circuit layout is shown of figure 5.24.

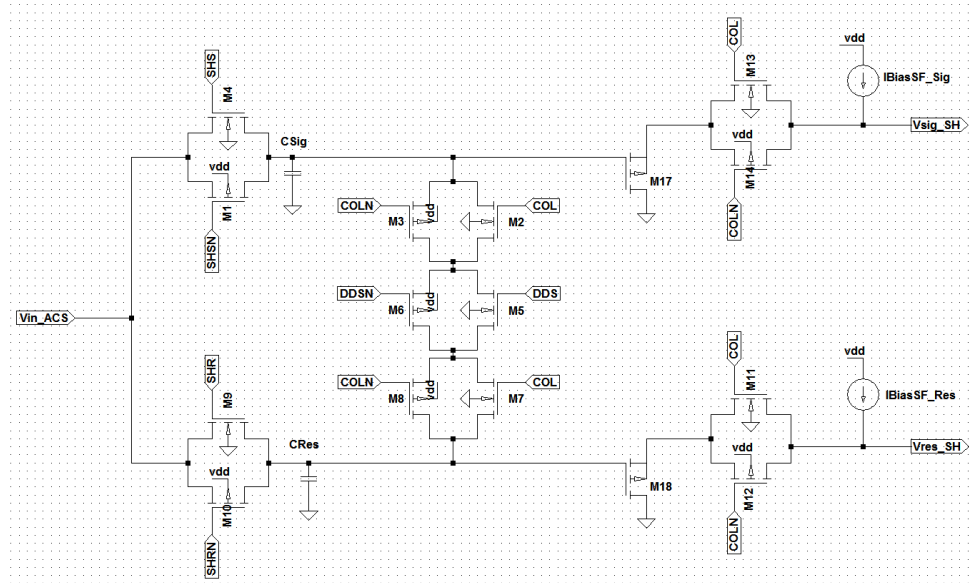


Figure 5.21: Schematic of NCDS-DDS Column circuit

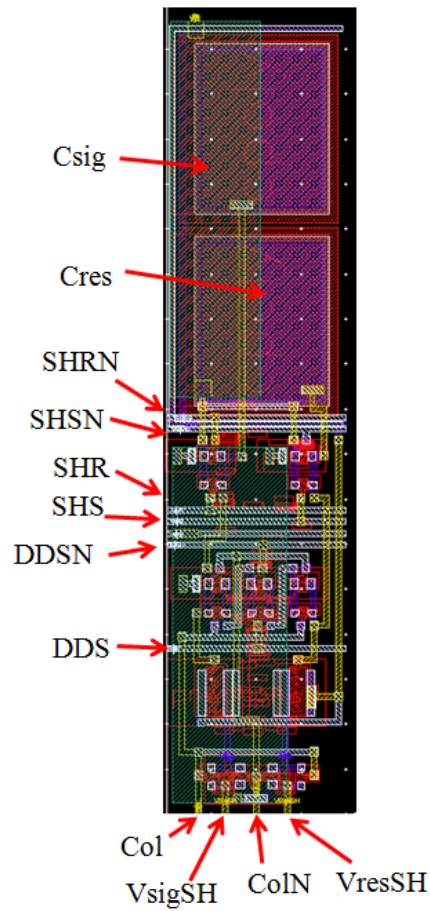


Figure 5.22: Virtuoso Cadence Layout of NCDS-DDS Column circuit

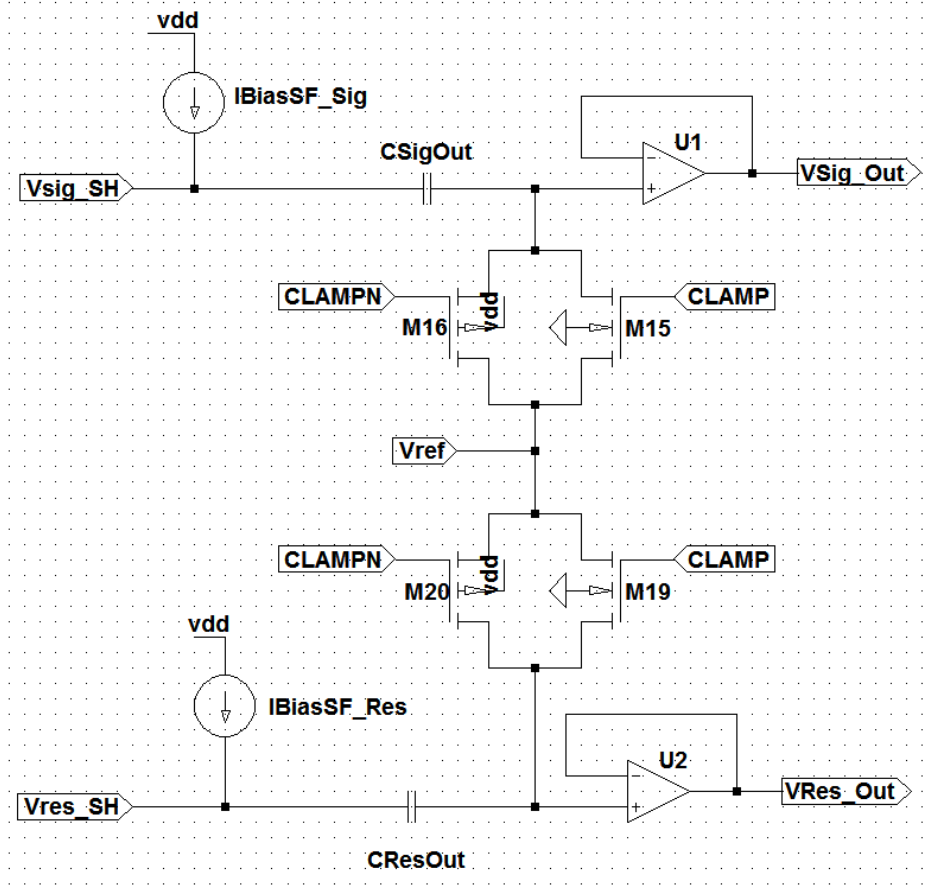


Figure 5.23: Schematic of CMOS-ACS shared output stage circuit

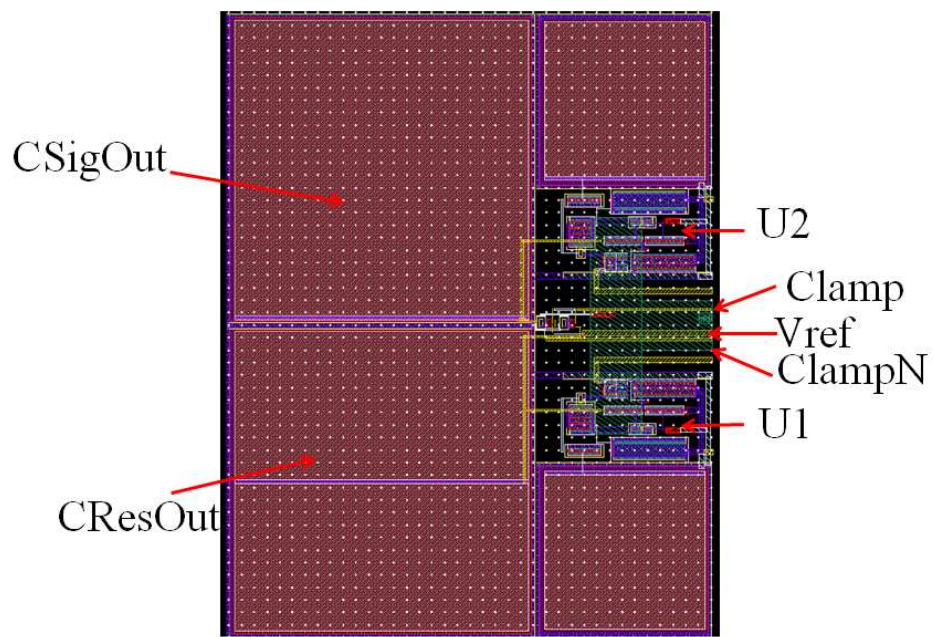


Figure 5.24: Virtuoso Cadence layout of global output stage

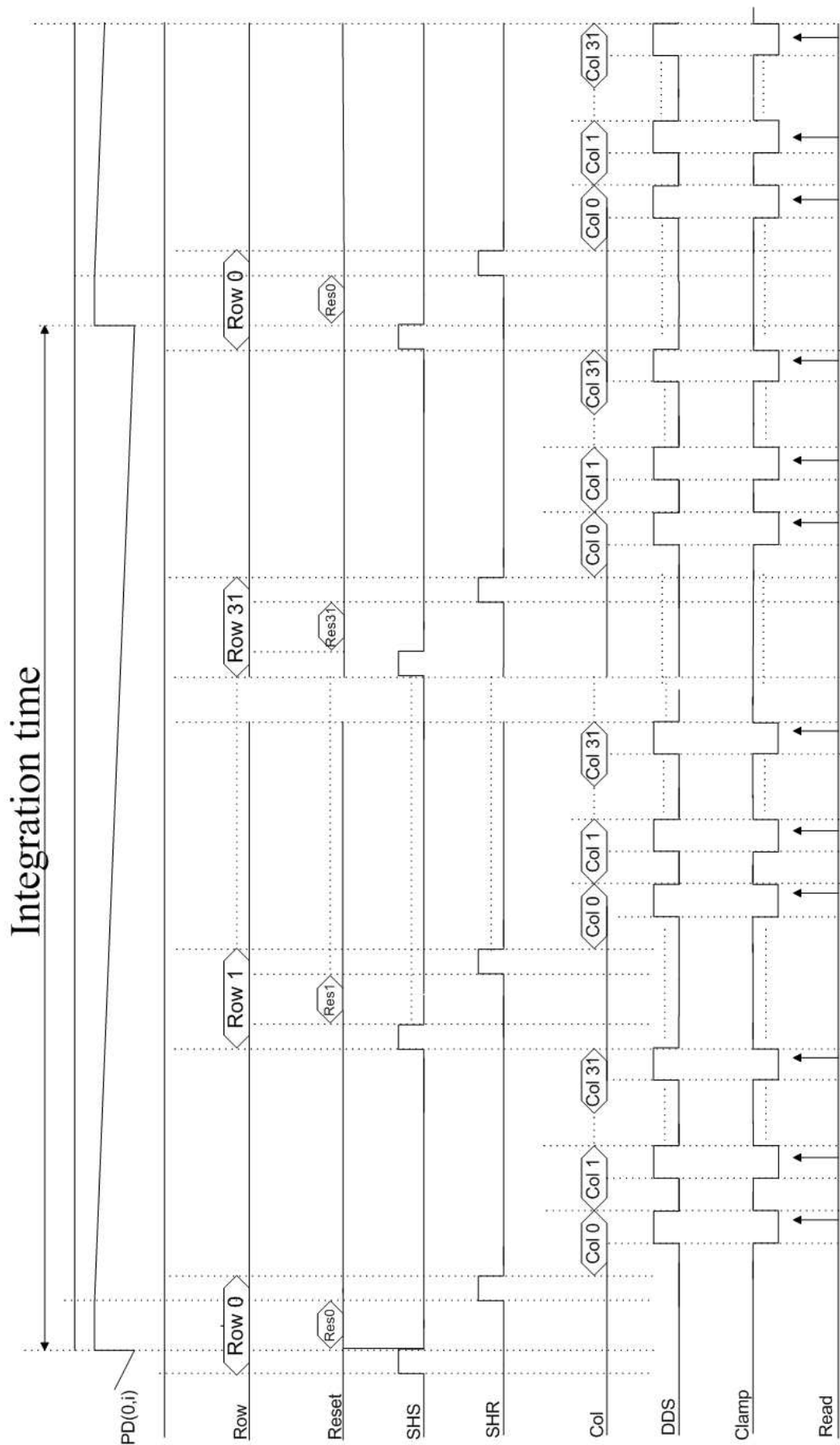


Figure 5.25: Proposed CMOS-ACS timing sequence diagram

Figure 5.25 shows the timing diagram of the prototype CMOS-ACS. With the first frame cycle serving as set-up and assuming the scan cycle has begun, the readout sequence is as follows:

1. A row is selected, this is done by sending the address to a 5 to 32 decoder and activating its enabling input. This will activate the 32 pixels (of the 32 columns) on this row.
2. SHS signal is activated. The 32 voltages at the end of integration time of the selected line (from the previous frame) are sampled. The signal will be buffered through their respective ACS column circuit and stored on their S/H signal capacitor C_{sig} .
3. SHS is deactivated and the Reset signal of the selected line goes high by enabling the 5 to 32 reset decoder. Due to the use of a NMOS reset transistor, the maximum voltage at which the photodiode's junction capacitance can be set is $V_{PD(i,j)} = V_{reset} - V_{THN}$.
4. The reset decoder is deactivated, at this point the integration time of the selected pixels begin, with their corresponding photodiodes junction capacitances discharging at a rate proportional to the illumination. At the same time, SHR is activated to store in the S/H reset capacitor the reset voltages. Considering that with the ACS at the pixel level we achieve unity gain, the signals at the output of the column circuits V_{sig-SH} and V_{res-SH} can be estimated following a procedure similar to the one described in reference [55]:

$$V_{res-SH} \simeq G_{SFP}[(G_{ACS} \cdot V_{pd-reset}) + V_{THP-reset}]. \quad (5.20)$$

Where G_{ACS} is the gain of the ACS amplifier, taken to be $G_{ACS} = 1$, G_{SFP} is the gain of the PMOS column SF and from equation 3.21 estimated at $G_{SFP} = 0.9$, $V_{THP-reset}$ is the threshold voltage of the column PMOS SF in the reset branch of the NCDS circuit, $V_{pd-reset}$ is the stored reset voltage. Similarly, for the signal at the end of integration.

$$V_{sig-SH} \simeq G_{SFP}[(G_{ACS} \cdot V_{pd-signal}) + V_{THP-signal}]. \quad (5.21)$$

Where $V_{pd-signal}$ is the signal's value at the end of integration time and $V_{THP-signal}$ is the threshold voltage of the column PMOS SF in the signal branch of the NCDS circuit. Ideally of equal value, in reality there is a difference of 10-20 mV between $V_{THP-signal}$ and $V_{THP-reset}$, this contributes to the column FPN of the imager. The DDS technique during the read phase is used to eliminate this variation.

5. The SHR and Row select signals are deactivated, then the sequential read of the 32 columns in the last selected line begins. As in the case of the row, the column address is selected through a 5 to 32 column decoder. First, column 0 is activated, each column select cycle is divided in two stages: during the first one, a time of

approximately half the column active time, the value stored in the S/H capacitors is stored in capacitors C_{SigOut} and C_{ResOut} . During this stage the Clamp signals are active, so V_{ref} is buffered as the output in both branches making:

$$V_{Sig-Out} = V_{Res-Out} = V_{ref} \quad (5.22)$$

6. During the second stage of the column select pulse, Clamp is deactivated and DDS activated simultaneously. At the column level this causes capacitors C_{sig} and C_{rest} to be shorted, thus the voltages at the S/H capacitors become:

$$V_{sig} = V_{reset} = \frac{G_{ACS}(V_{pd-sign} + V_{pd-reset})}{2} \quad (5.23)$$

This in turn causes that

$$V'_{res-SH} \simeq G_{SFP} \cdot \left[G_{ACS} \left(\frac{V_{pd-sign} + V_{pd-reset}}{2} \right) + V_{THP-reset} \right], \quad (5.24)$$

and,

$$V'_{sig-SH} \simeq G_{SFP} \cdot \left[G_{ACS} \left(\frac{V_{pd-sign} + V_{pd-reset}}{2} \right) + V_{THP-signal} \right]. \quad (5.25)$$

Since the clamp transmission gates are now open,

$$V_{Res-out} \simeq G_{U2}(V_{ref} + V'_{res-SH} - V_{res-SH}) \quad (5.26)$$

$$V_{Sig-out} \simeq G_{U1}(V_{ref} + V'_{sig-SH} - V_{sig-SH}) \quad (5.27)$$

And with,

$$V'_{res-SH} - V_{res-SH} = G_{SFP} \left[G_{ACS} \left(\frac{V_{pd-reset} - V_{pd-sign}}{2} \right) \right] \quad (5.28)$$

$$V'_{sig-SH} - V_{sig-SH} = G_{SFP} \left[G_{ACS} \left(\frac{V_{pd-sign} - V_{pd-reset}}{2} \right) \right] \quad (5.29)$$

where we notice that thanks to the DDS technique the terms $V_{THP-signal}$ and $V_{THP-reset}$ can be eliminated.

7. We are interested in the difference between the output reset and signal voltages, this will be done externally, as will be discussed in the next chapter. Assuming that the output amplifiers U1 and U2 have the same gain ($G_U=1$), theoretically this difference will be given by:

$$V_{Sig-out} - V_{Res-out} = G_U [G_{SFP}G_{ACS} (V_{pd-reset} - V_{pd-sign})] \quad (5.30)$$

8. Next, the column and DDS signals are deactivated and the process repeated for the next column, until the 32 column on the line were read.
9. The next row is selected and steps 1 to 8 repeated, continuously scanning the matrix.

A Monte Carlo simulation for 500 samples was performed and observing the pixel's output. Without double sampling, for a constant photocurrent, the variance on the output is 3.3 mV, while for the output with NCDS subtracting a reset level the variance is 0.5 mV, as seen in figure 5.26.

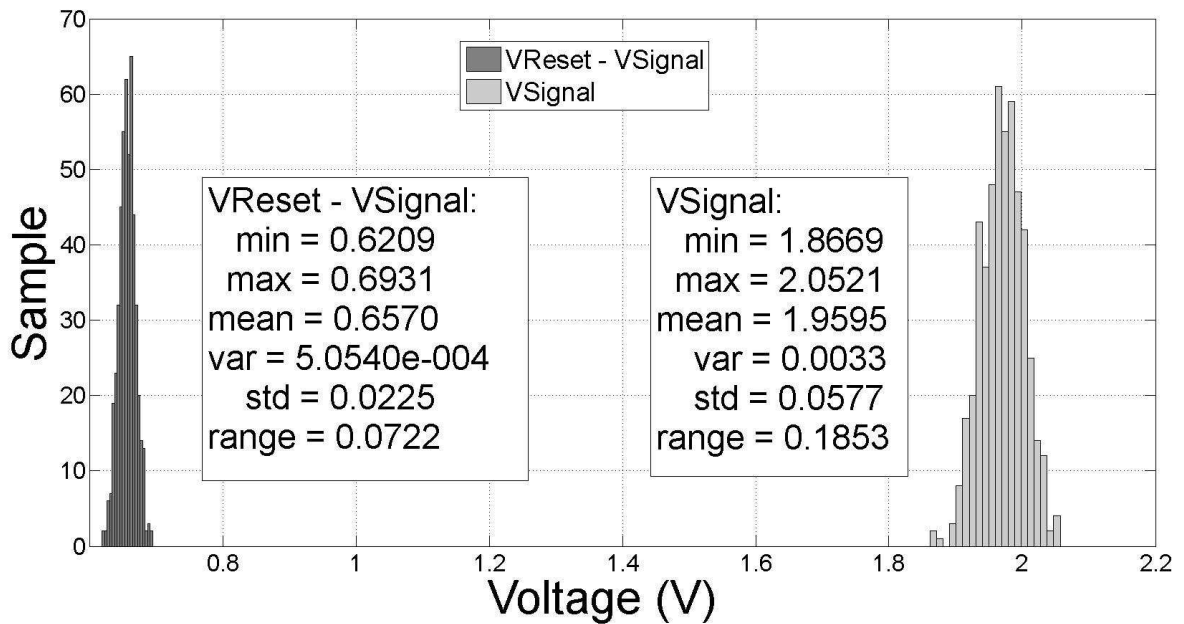


Figure 5.26: Variation of output with and without NCDS for a constant photocurrent. 500 sample Monte Carlo simulation

5.4.1 Output amplifier

For the design of the output amplifier, the strict space constraints required for the column ACS amplifier don't exist. However there is the need to increase the bandwidth, due to the fact that the output amplifier buffer the outputs from all the columns. For a larger GB specification a nulling resistor compensation method is used [24]. Figure 5.27 presents the schematic of the output op-amp schematic. Following the same procedure as the column ACS amplifier, adding the steps to determine the size of transistors M8, M9, M10 and M11 added to move the RHP-Zero at the second pole p2 location and ultimately providing additional robustness. Table 5.9 shows the specifications of the Op-amp out amplifier,

Through an iterative simulation, the transistor ratios are obtained as shown on table 5.10

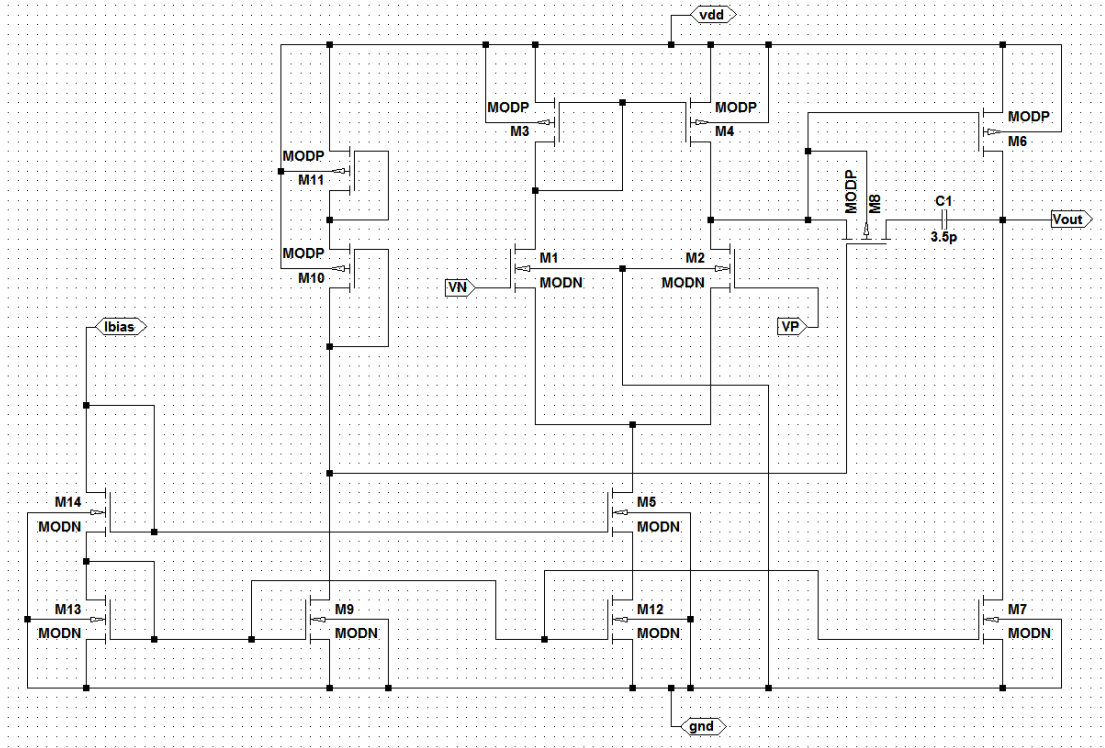


Figure 5.27: Schematic of output amplifiers (Reset and signal voltages)

Table 5.9: Specifications of the Output amplifier

$0V < ICMR < 2.9V$
$I_5 = I_{Bias} = 100 \mu A$
$GB > 10 \text{ MHz}$

Table 5.10: Output op-amp transistor ratios

I_{Bias}	100 μA
C_c	3.5 pF
$(W/L)_{1,2}$	15 $\mu m / 1 \mu m$
$(W/L)_{3,4}$	10.3 $\mu m / 1 \mu m$
$(W/L)_{5,12,13,14}$	4 $\mu m / 1 \mu m$
$(W/L)_6$	140 $\mu m / 0.35 \mu m$
$(W/L)_7$	70 $\mu m / 1 \mu m$
$(W/L)_8$	12.8 $\mu m / 1 \mu m$
$(W/L)_9$	4 $\mu m / 1 \mu m$
$(W/L)_{10}$	1 $\mu m / 1 \mu m$
$(W/L)_{11}$	43 $\mu m / 1 \mu m$
Single Supply	vdd=3.3 V, vss=gnd

Figures 5.28 to 5.32 show the results of the simulations performed to obtain the output op-amp performance.

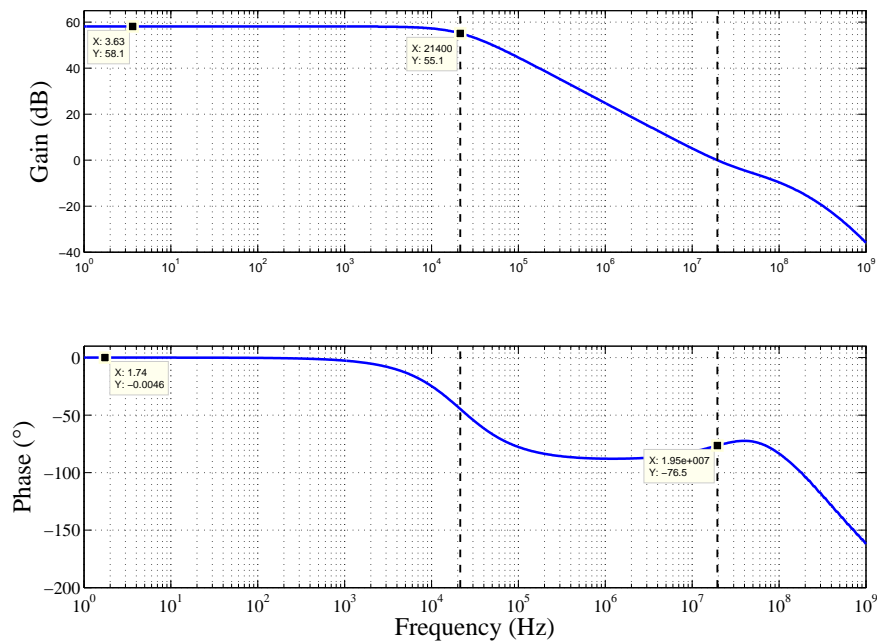


Figure 5.28: Simulated frequency response of output op-amps

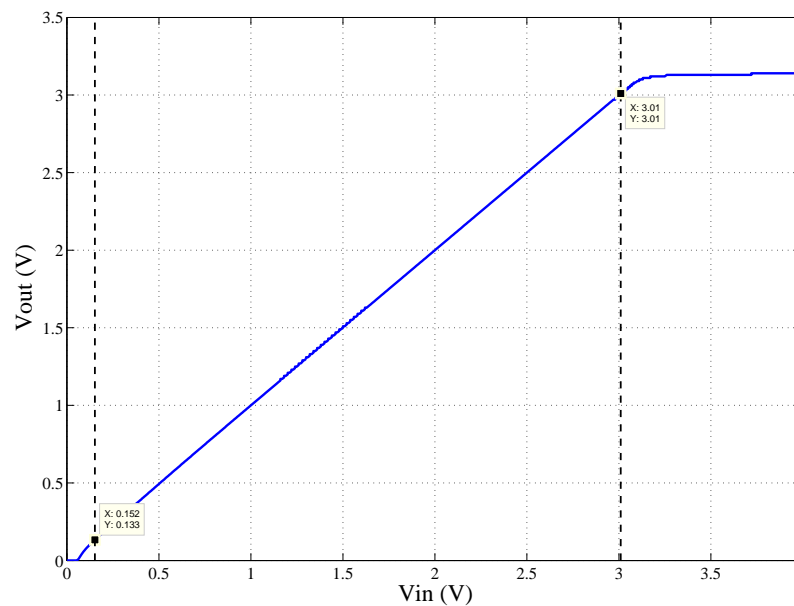


Figure 5.29: Simulated Input Common Mode Range (ICMR) of output op-amps

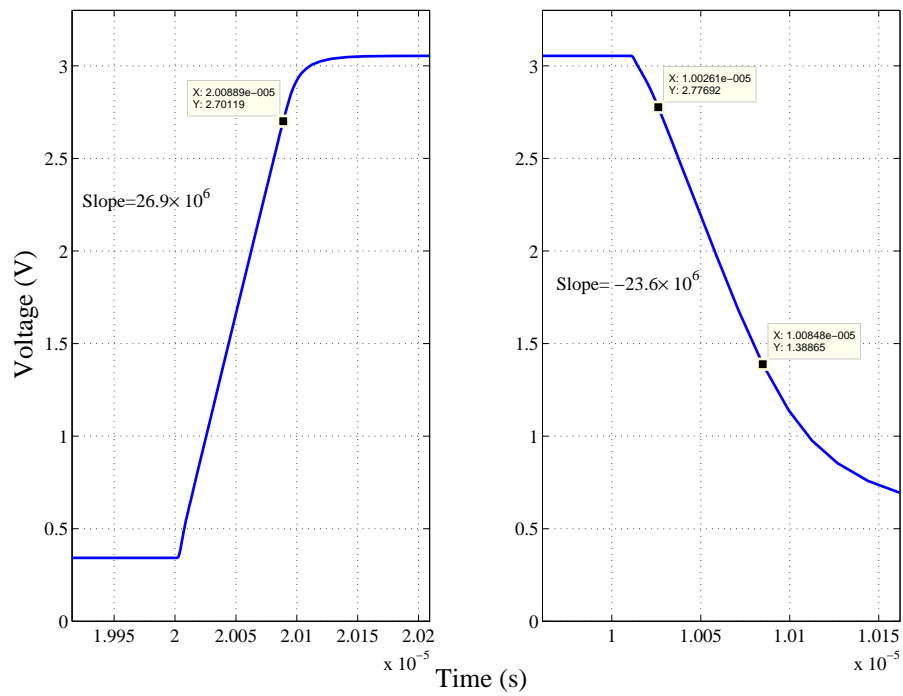


Figure 5.30: Simulated positive and negative slew rate of output op-amps

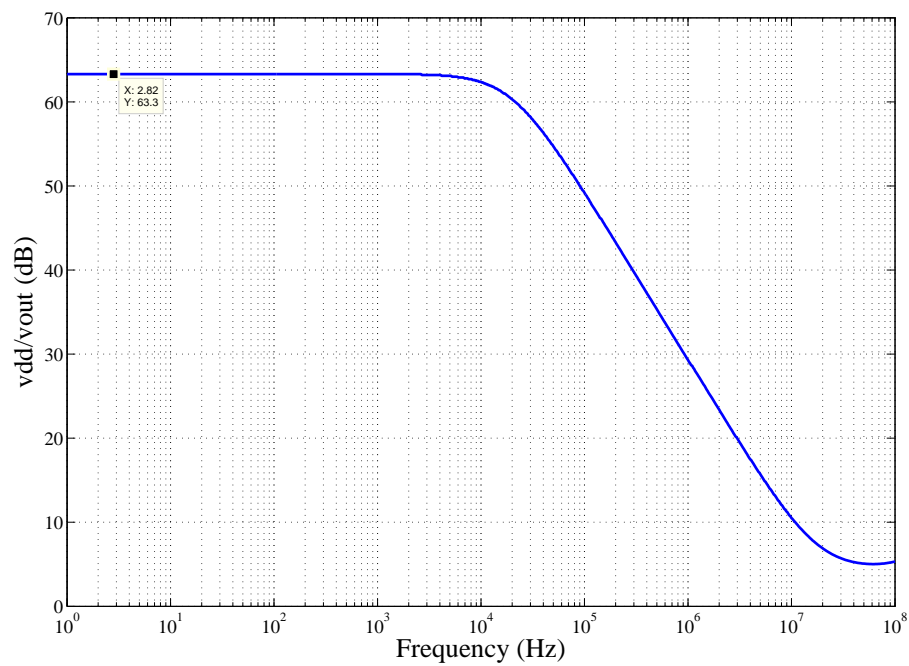


Figure 5.31: Simulated power supply rejection ratio of output op-amps

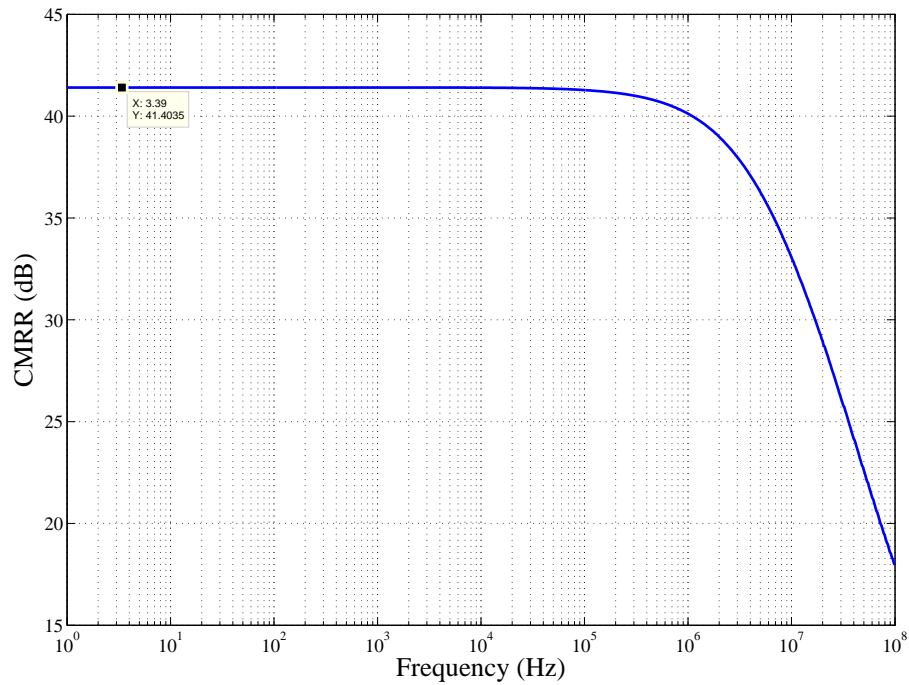


Figure 5.32: Simulated common mode rejection ratio of output op-amps

Table 5.11 presents the final performance characteristics of the both output op-amps.

Table 5.11: Final ACS op-amp performance characteristics

Open loop gain	58.1 dB
Cut-off frequency	21.4 KHz
Gain bandwidth (GB)	19.5 MHz
Phase margin	103.5°
PSRR	63.3 dB
CMRR	41.4 dB
ICMR	0.15 V - 3.1 V
Output Swing	0.20 V - 3.1 V
Slew rate (positive)	26.9 V/ μ s
Slew rate (negative)	-23.6 V/ μ s
Slew rate (average)	25.2 V/ μ s

5.4.2 CMOS-ACS 4x4 cadence simulation

To test the proper performance of the circuit and its agreement with the equations, a sub-array of 4×4 pixels, as shown on figure 5.33 is simulated with the AMS $0.35 \mu\text{m}$ kit in Cadence. For different values of the photocurrent, the values of the photodiode voltage, the ACS amplifier output voltage, the column voltages after the PMOS-SF, the two output voltages, the simulated differential output and the estimated differential output from equation 5.30. A curve describing the sensor's differential output vs the input photocurrent is shown on figure 5.34, where the saturation voltage is estimated at 2.3 V. A linear fit is applied to the resulting data, obtaining the following equation describing the relation between input photocurrent and the differential output voltage:

$$V_{diff} = 6.429 \times 10^{11} \cdot I_{ph} - 0.425[V]. \quad (5.31)$$

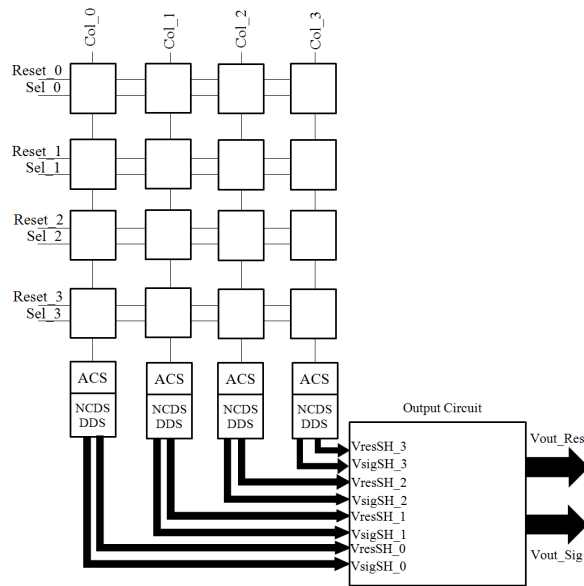


Figure 5.33: Simulated 4×4 pixel array

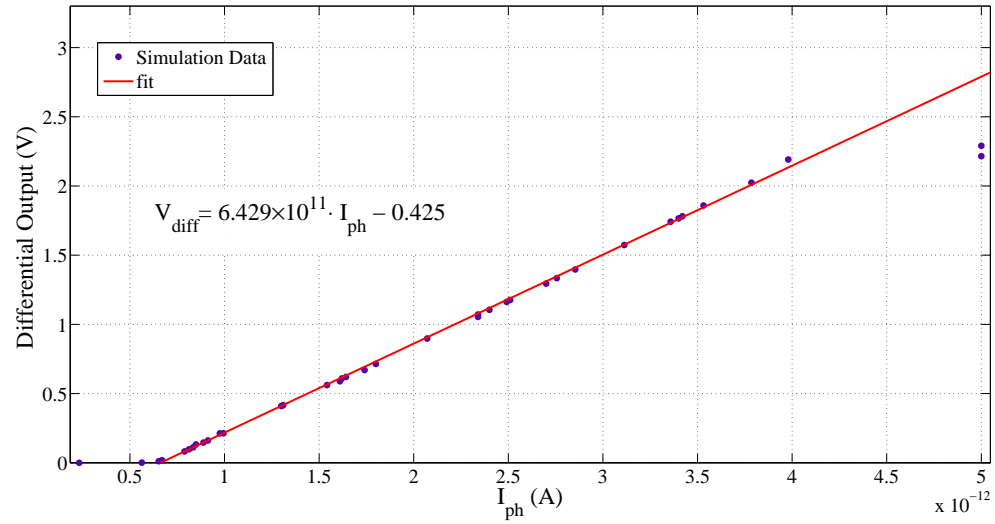


Figure 5.34: Differential output dependency on the photocurrent.

5.5 Complete CMOS-ACS chip

Integrating all the described elements, the schematic in figure 5.35 shows the complete output chain for one column in the proposed circuit. Figure 5.36 presents the 32×32 -pixel CMOS-ACS prototype, built with the AMS C35B4C3 $0.35 \mu\text{m}$ CMOS process (3.3V). The chip dimensions are $2 \text{ mm} \times 2.25 \text{ mm}$.

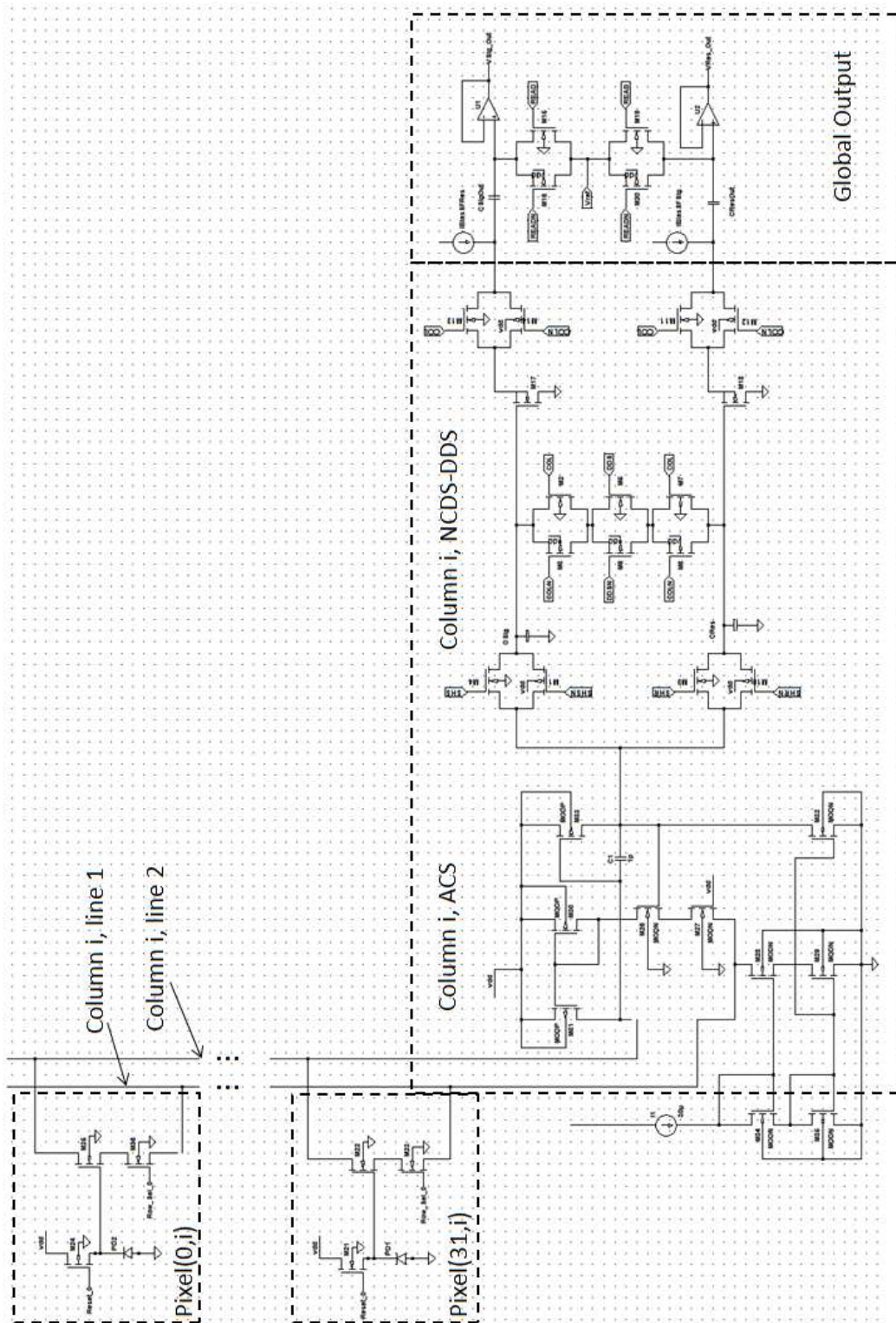


Figure 5.35: Schematic of CMOS-ACS with NCDS-DDS

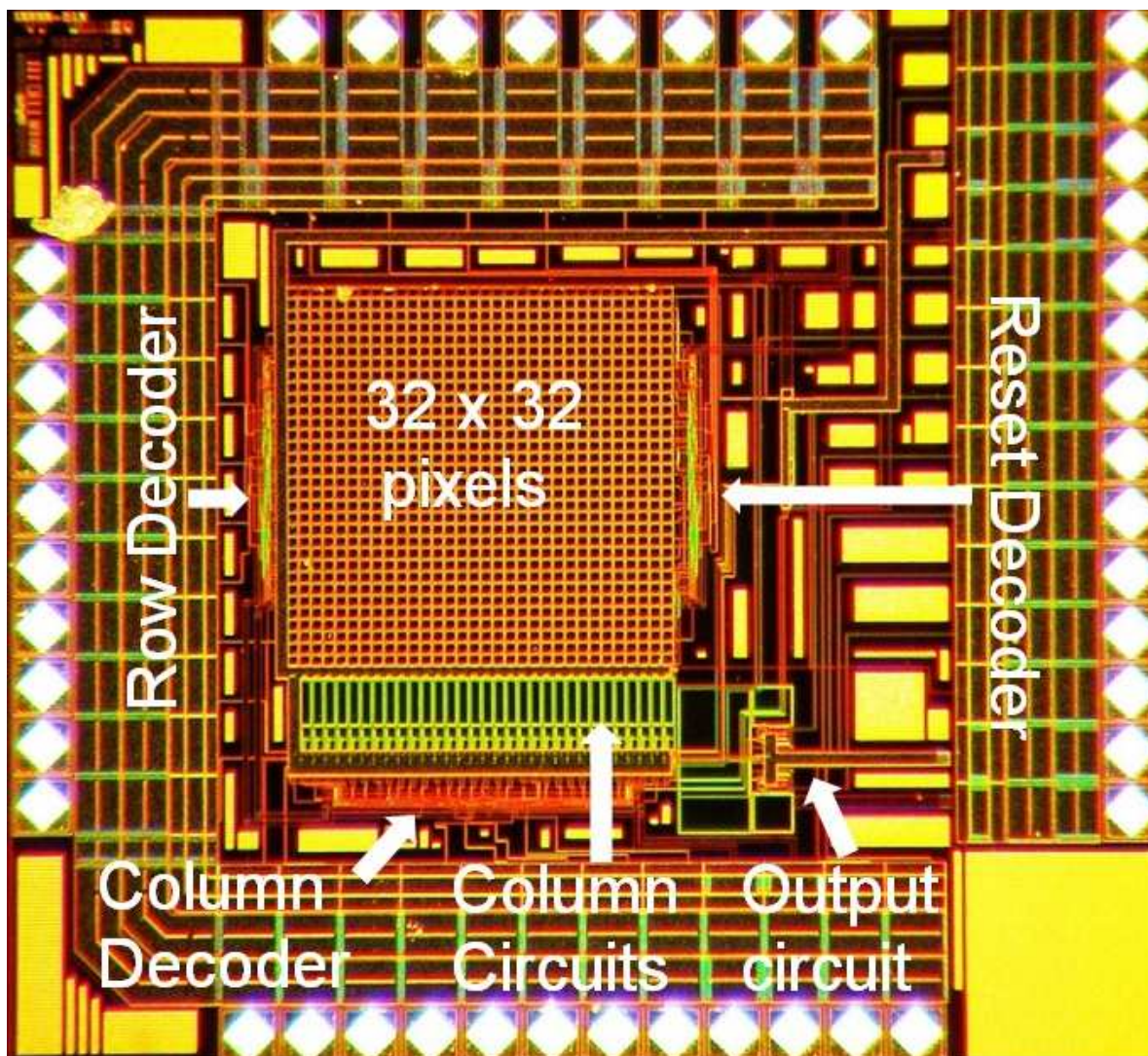


Figure 5.36: CMOS-ACS chip. AMS $0.35\mu\text{m}$ CMOS 3.3V. Total chip area $2\text{ mm} \times 2.25\text{ mm}$

5.6 Conclusions

In this chapter the design of a first 32×32 -pixel CMOS-ACS prototype, intended to be included on an SPR biosensing platform was presented. First, with the aid of TCAD software Silvaco, the CMOS photodiode that will give a better photoresponse for our purposes was found. With a higher efficiency and conversion gain, a n-well/p-sub is the selected photosensing element inside the imager pixel. The use of ACS readout is used to eliminate variations due to the use of the in-pixel source follower and thus reduce the pixel FPN. Furthermore the use of NCDS-DDS are used to eliminate the column FPN. Simulations in cadence for a small array show good agreement between the equations and the outputs. Next chapter the performance test of the imager will be presented.

Chapter 6

Characterization of 32×32 CMOS imager with ACS

6.1 Introduction

This chapter presents the characterization tests for the designed prototype of the 32×32 -pixel CMOS-ACS imager. In section 6.2, the test card and communication with the PC is briefly described. Next, in section 6.3 the characterization of the CMOS-ACS prototype is performed, obtaining parameters such as conversion gain, dark current, sensitivity, dynamic range and FPN, where the benefits of the readout strategies implemented are observed. Finally, the expected performance of the CMOS-ACS imager in a SPR bioensing platform is briefly discussed.

6.2 Test Card

The function of the test card is to provide the analog supply voltages and bias to the CMOS-ACS, provide the control signals to the circuit, additionally, in the test card the subtraction operation between the two outputs of the sensor is performed and the resulting signal digitized through a 16-bit differential input ADC. The test card also coordinates the communication between the sensor and the PC. Figure 6.1 shows a photo of the test card. Figure 6.2 presents the general block diagram of the test card, its functioning will be described next.

The core of the test card is a FPGA Spartan-3AN (XC3S50AN), this device generates the control signals, implements an 2048×16 FIFO memory where the pixel output is stored, controls the ADC process and establish communication with a PC. For this first prototype, the flexibility to control the input signals and thus the integration time is of great importance.

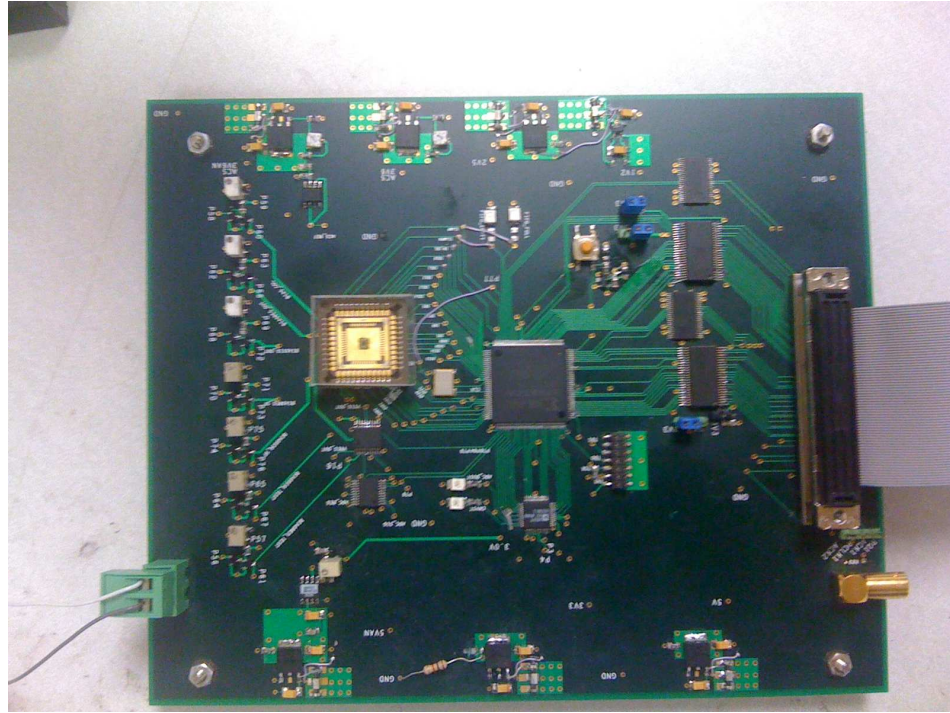


Figure 6.1: Test Card Circuit

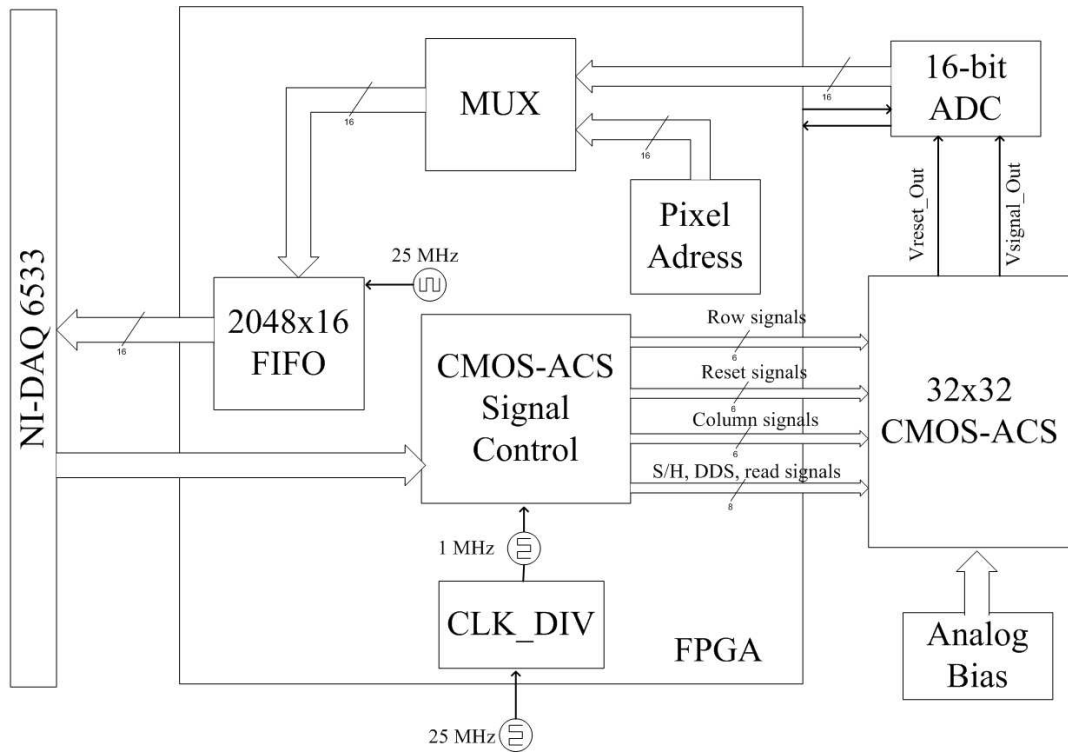


Figure 6.2: Test Card block diagram

6.2.1 CMOS-ACS digital control signals

The signal control module operates at a frequency of 1 MHz, limiting the minimum pulse width to 1 μ s. However for our purposes this doesn't represent a disadvantage not being the focus of this project a high-speed CMOS image sensor, since the reaction rates associated with binding interactions in SPR biosensors is in the order of dozens of seconds [15].

The basic timing sequence to operate the image sensor is described on section 5.4 and graphically shown on figure 5.25. In appendix B the pin description of the sensor is presented. The control sequence is implemented as a state machine, where once the sequence is initiated, the FPGA will continuously generate the digital control signals to scan the pixel's array.

One of the main advantages of an external control is the integration time tuning according to the particular needs of the application. Longer integration times for low light scenarios and shorter times for illuminated scenes. The integration time, can be modified in two ways: first, by changing the duration of the control pulses, with the read column time having the bigger impact in this time, since for each row all the columns are read sequentially. For example for the 32x32 array, a 30 fps can be achieved by taking a row select width of 80 μ s and a column width of 30 μ s.

Second, the integration time can also be changed by selecting a sub-window in the pixel array and thus, by reducing the size of the array to scan reducing the integration time. This "windowing" characteristic is precisely one of the main advantages of CMOS image sensor, and that in our case represents the potential for example to focus on a specific section of a DNA or protein microarray while performing SPR imaging. Both the duration of the control pulses and the size of the sub-array to scan can be controlled through an interface between a PC running NI-LabView 2010 and the test card.

6.2.2 Analog to Digital conversion and 2048x16 FIFO

A 16-bit resolution, differential input ADC (Analog Devices AD7677) is used to compute and digitize the difference between the two CMOS-ACS outputs (signal and reset). The ADC uses an external 3.0 V reference supporting an input range of ± 3 V, with the conversion process controlled by the FPGA using the CLAMP signal as conversion clock.

The 16-bit ADC output is taken by the FPGA and sent to a multiplexer controlling the access to a FIFO (First In, First Out) memory where the values will be stored. The purpose of this step is to add the pixel's coordinates to the read value in order to facilitate the image processing. The pixel's coordinates will be stored in the previous FIFO address to the pixel's output. This way, 1024 spaces on the FIFO will be occupied by the sensor's output (1 frame) and the other 1024 will correspond to the pixel's address, as illustrated in figure 6.3, where each pixel's is always preceded in the FIFO by its corresponding coordinate. The format of the coordinates is from LSB to MSB, 5 bits representing the column, 5 bits representing the row and the 16 bit word is completed with "1's".

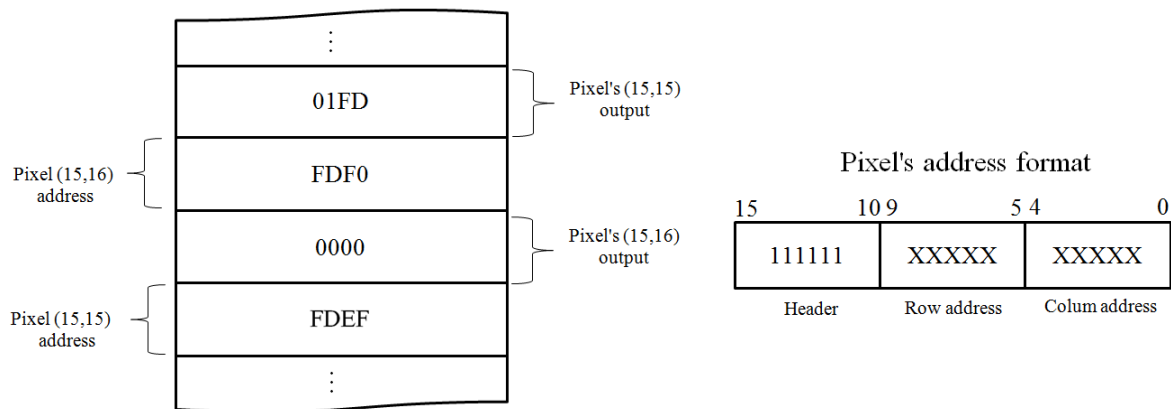


Figure 6.3: FIFO memory address format

6.2.3 Interface with NI-LabView

Communication between the test card and a PC is done with a National Instruments DAQ card PCI-6533. Transferring data between the two devices involves the exchange of signals to request and acknowledge each data transfer in a handshaking I/O mode. With LabView 2010 commands such as start/stop, reset, begin data acquisition are transferred to the test card, furthermore we are able to send the control signals duration and/or select a pixel sub-array.

6.3 CMOS-ACS prototype characterization

Obtaining accurate results strongly depends on the use of an appropriate and quality light source. To properly characterize the device, it is desired a source that is directional, monochromatic and uniform over the entire photosensitive area of the sensor. While a laser produces a highly monochromatic beam and is used frequently on SPR applications, its beam is not as uniform as needed. For characterization purposes an halogen lamp (Thorlabs OSL1) is selected, which results in a more uniform beam. In the used optical experiments, the white light is made monochromatic by passing it through a color filter and directed by collimating the beam and passing it through an optical diaphragm (aperture). The optical setup is shown on figure 6.4.

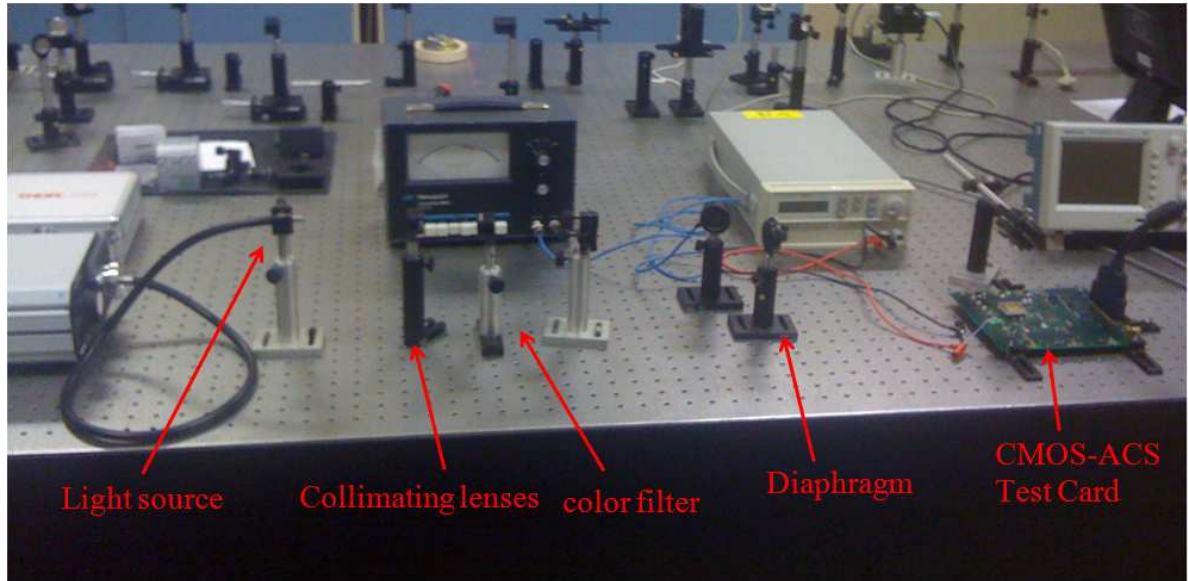


Figure 6.4: Optical test setup

6.3.1 Conversion Gain

The conversion gain is one of the most important parameters in the characterization of an image sensor, as mentioned on section 3.3, it is a measure of the signal generated per photogenerated electron and can also be given by [26]:

$$CG = \frac{\partial x}{\partial QE \cdot \Phi}. \quad (6.1)$$

Where x is the sensor's output signal, QE is the quantum efficiency and Φ is the number of photons incident on the sensor during integration. The number of photons arriving at the pixel is difficult to obtain, an alternative to compute the conversion gain is described in reference [57], where with Poisson statistics the conversion gain is estimated. First, considering that fluctuations on the number of detected photons ($S_{QE \cdot \Phi}$), produces a fluctuation S in the sensor's output x , expressed as:

$$S = \frac{\partial x}{\partial QE \cdot \Phi} S_{QE \cdot \Phi} = CG \cdot S_{QE \cdot \Phi}. \quad (6.2)$$

Taking photons fluctuation to be a standard deviation following a Poisson distribution as:

$$S_{QE \cdot \Phi} = (QE \cdot \Phi)^{1/2}. \quad (6.3)$$

Additionally, assuming a linear relation in equation 6.1, the mean number of photons is given by:

$$\overline{QE \cdot \Phi} = \frac{\bar{x}}{CG}. \quad (6.4)$$

From equations 6.2 to 6.4 the conversion gain in $\mu\text{V}/e^-$ is:

$$CG = \frac{S^2}{\bar{x}} \quad (6.5)$$

Where S^2 is the variance of the detector's signal and \bar{x} the mean value of the detector's signal. The measurement of this parameter can be done by uniformly illuminating the image sensor, and stepping the light's intensity from darkness to saturation in determined increments, taking at each stage 50 frames from where the variance and mean of the sensor's differential output are obtained. The conversion gain is the slope of these curve. A Newport 818-SL photodetector is used as a reference detector to monitor the changes in light intensity. In Figure 6.5 a line is fitted to the measurements resulting in a conversion gain of $7.3 \mu\text{V}/e^-$. Furthermore, from this curve we observe a saturation voltage of 2.4 V, resulting in a full-well capacity of $118.81 \times 10^3 e^-$.

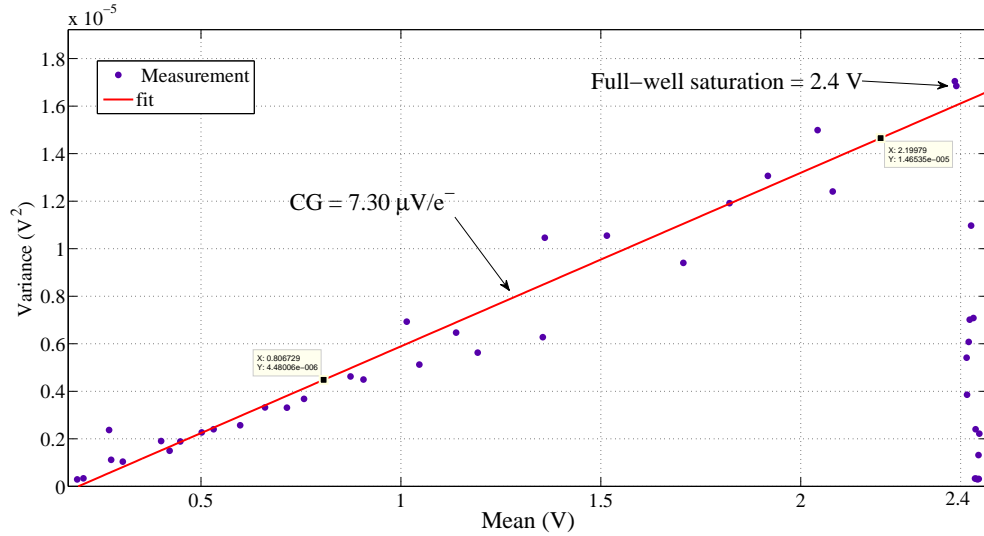


Figure 6.5: Conversion gain measurement. Slope of fit $7.3 \mu\text{V}/e^-$.

The estimated conversion gain implies a photodiode capacitance $C_{PD} = q/CG = 21.9 \text{ fF}$, compared with the capacitance obtained from the electrical simulation of $C_{PD} = 31 \text{ fF}$.

6.3.2 Dark current

The variations in the dark current from pixel to pixel is one of the main contributors of FPN in the sensor (DSNU). These variations have their origin mainly on the variations inherent to the CMOS process. The dark current is obtained by measuring the sensor's output under no-illumination conditions for different integration times and computing the mean output. The slope of the curve results in a dark voltage in (V/s) . The dark current density is subsequently given by [26]:

$$J_{dark} = \frac{V_{dark} \cdot q}{CG \cdot A_{PD}}. \quad (6.6)$$

Where V_{dark} is the obtained mean output vs integration time slope and A_{PD} is the photosensitive area. The mean voltage under dark conditions is presented in figure 6.6, where the slope of the curve results in $V_{dark} = 0.43 \text{ V/s}$. From equation 6.6 the resulting dark current density is $J_{dark} = 0.014 \text{ fA}/\mu\text{m}^2$, or a dark current $I_{dark} = 3.42 \text{ fA}$ for one pixel with a photodiode of area $244 \mu\text{m}^2$. Comparing this results with figure 5.3, a noticeable difference is observed. A possible contributor to this discrepancy is the fact that the values of the SRH lifetime of the carriers were not properly selected according to the concentration levels given by the foundry and from where the simulated structures were constructed. In Silvaco the default lifetimes are at a value of $0.1 \mu\text{s}$ for both acceptors and donors, with this values taken to perform the recombination dark current simulation. From the process parameters, given in [33], more appropriate values for the carrier lifetimes are 40 ns for the donors and $0.2 \mu\text{s}$ for the acceptors [58]. However, further test on Silvaco need to be conducted for the dark current in order to determine the source of this difference. To confirm the correct experimental estimation of the dark current, a simple cadence electrical simulation with AMS $0.35 \mu\text{m}$ kit for the n-well diode shows a leakage current of 1.17 fA , a result closer to the estimated experimental value.

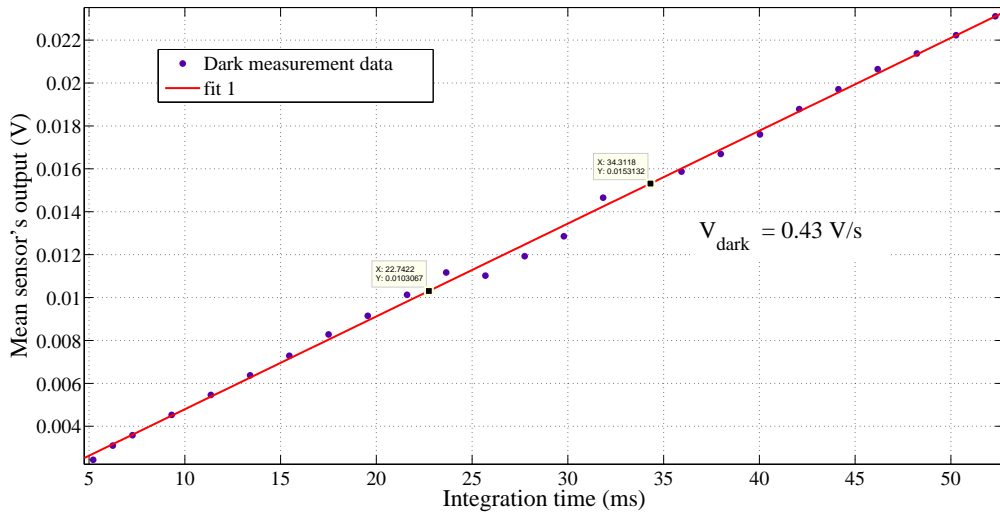


Figure 6.6: Measurement of dark voltages for different integration times.

6.3.3 Sensitivity

This parameter indicates the sensor's output change for a given integration time at an specific light intensity (exposure). The measurement of the sensitivity is done by taking 100 frames of the sensor, starting from dark conditions and increase the illumination level

at known steps. The mean of the taken frames for each illumination level is calculated with the slope of the resulting curve being the sensitivity. The incident light intensity is controlled using a calibrated reference photodetector (Newport 818-SL) and a Newport Model 820 Laser Power Meter. The Thorlabs OSL1 light source has a lamp intensity adjustment ramp from 0 to 100% and maximum light output of 430,000 Lux. A 610 nm filter is used to produce a red monochromatic light. Finally, to cover the whole range of the image sensor, from dark to full-well saturation, the imager is programmed for three different integration times: 2.240 ms, 8.32 ms and 24.640 ms. Figure 6.7 shows the measured sensitivity curve, resulting in a sensitivity of $0.26 \text{ V/Lux} \cdot \text{s}$

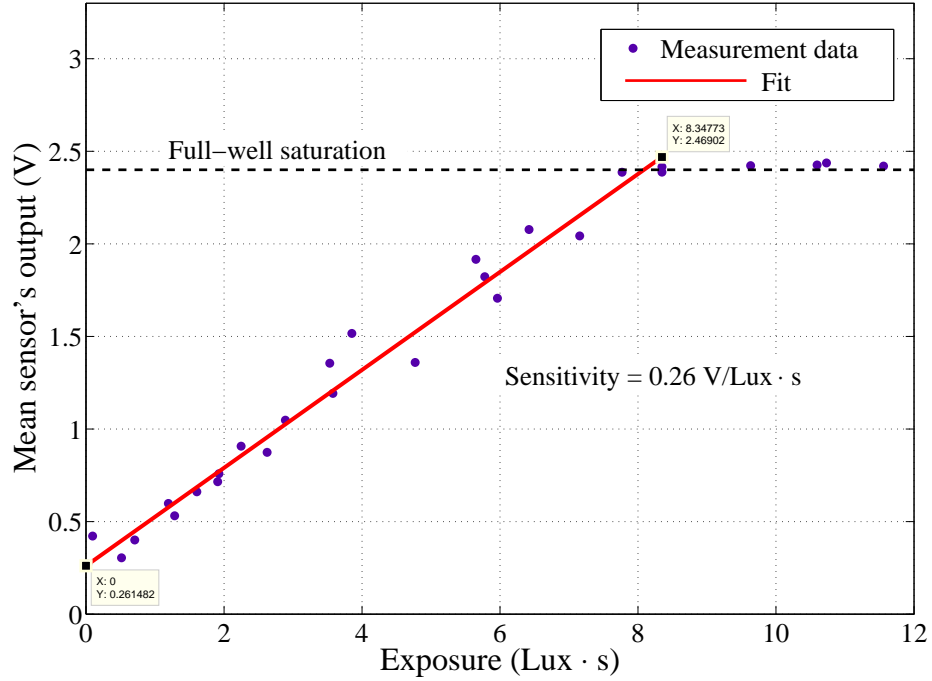


Figure 6.7: Measurement of sensitivity of CMOS-ACS.

6.3.4 Fixed Pattern Noise

For a $M \times N$ pixel's array, under uniform monochromatic illumination the FPN ($F_{i,j}$) is taken to be the sum of the pixels ($X_{i,j}$) and the columns (Y_j) FPN contribution, where i and j are the row and column number respectively. It is assumed that both parameters are uncorrelated, since their variations depend on different process parameters. A detailed description of the method followed for the estimation of FPN is presented on reference [30]. Where the FPN can be described through the following equations:

$$F_{i,j} = Y_j + X_{i,j}. \quad (6.7)$$

$$\overline{Y}_j = \frac{1}{M} \sum_{i=1}^M F_{i,j}, \quad (6.8)$$

$$\overline{X}_{i,j} = F_{i,j} - \overline{Y}_j. \quad (6.9)$$

$$\overline{\sigma_Y^2} = \frac{1}{N-1} \sum_{j=1}^N \overline{Y}_j^2, \quad (6.10)$$

$$\overline{\sigma_X^2} = \frac{1}{N(M-1)} \sum_{i=1}^M \sum_{j=1}^N \overline{X}_{i,j}^2, \quad (6.11)$$

The estimation of the FPN parameters were made at 50% of full-well saturation illumination and under dark conditions, with an integration time $T_{int} = 8.3$ ms. First, 1000 frames were taken and averaged over time, obtaining one frame where random temporal noise variations from frame to frame are eliminated. Then, $F_{i,j}$ for a given pixel is calculated as the difference between the pixel's differential output and the averaged pixel's value, from where the rest of the parameters are obtained. The FPN can then be taken as the standard deviation in pixel or column voltages and expressed as a percentage of the full-well capacity. For the dark frame (DSNU), the pixel's FPN is estimated at 0.024% and the column FPN at 0.006%. While for the 50% of full-well saturation illumination the pixel's FPN is estimated at 0.09% and the column FPN at 0.06%.

The effect of CDS and ACS can be observed by instead of analyzing the sensor's differential output, taking only measurements and applying the same procedure to the single signal branch without subtracting the reset and signal voltages. Resulting in a pixel FPN 0.47% and column FPN of 5.43% for dark conditions; and a pixel FPN of 0.35% and column FPN of 4.19% for 50% of full-well saturation illumination. Observing a significant reduction in column FPN due to the use of NCDS and pixel FPN reduction due to the use of ACS configuration. Figures 6.8 and 6.9 present a normalized frame for each case observing the greater variations in the single signal output.

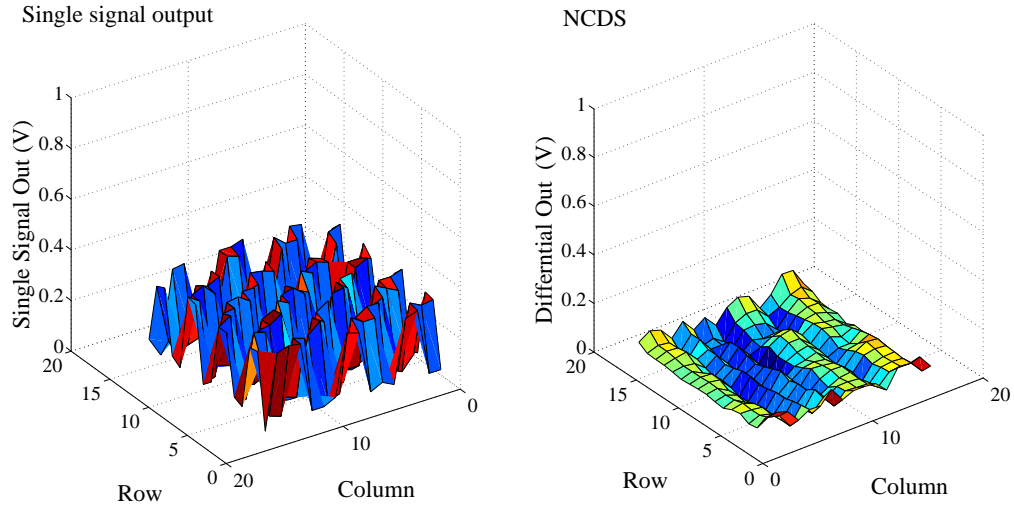


Figure 6.8: Output Frame for dark illumination conditions. Single signal output and differential output with NCDS

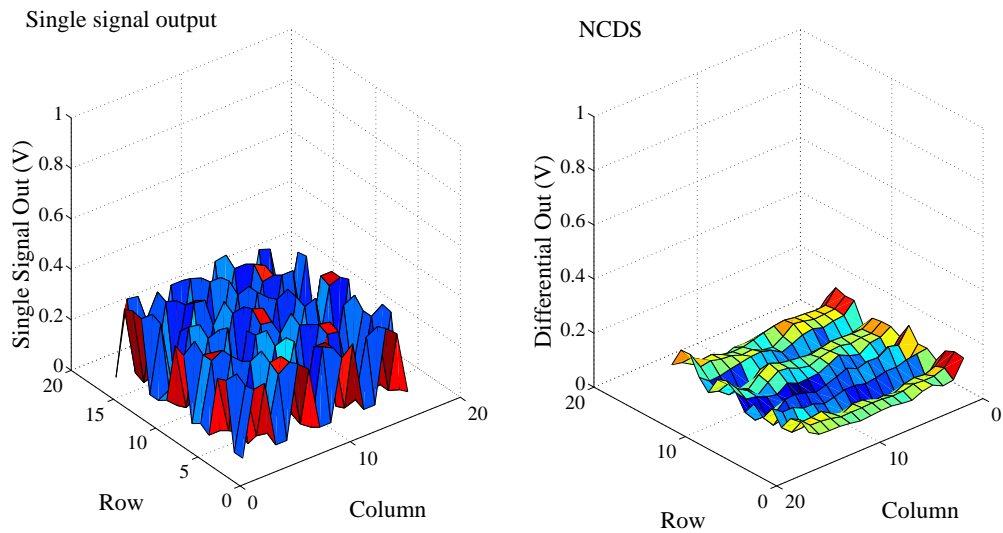


Figure 6.9: Output Frame for 50% of full-well saturation illumination conditions. Single signal output and differential output with NCDS

6.3.5 Read Noise

The measurement of the read noise is done by selecting only one pixel and recording its differential output for a short exposure time of $100 \mu s$ under dark conditions. The short integration time and dark conditions ensures that the signal and reset branches are practically equal with the dispersion being only due to the signal's path circuitry noise and the reset noise. The $1/f$ noise, dominant at long exposure times, is disregarded for these measurements. The read noise is then calculated as the RMS difference:

$$\sigma_R = \sqrt{\frac{\sum_{i=1}^N (V_{pix} - \overline{V_{pix}})^2}{N - 1}}. \quad (6.12)$$

Where V_{pix} is the pixel's output, $\overline{V_{pix}}$ the pixel's mean output, and N the total number of readings. The resulting read noise is estimated from figure 6.10 as the standard deviation of the pixel's output with a value of $\sigma_R = 324.5 \mu\text{V}$, or equivalently, using the conversion gain the read noise is $45 e^-$.

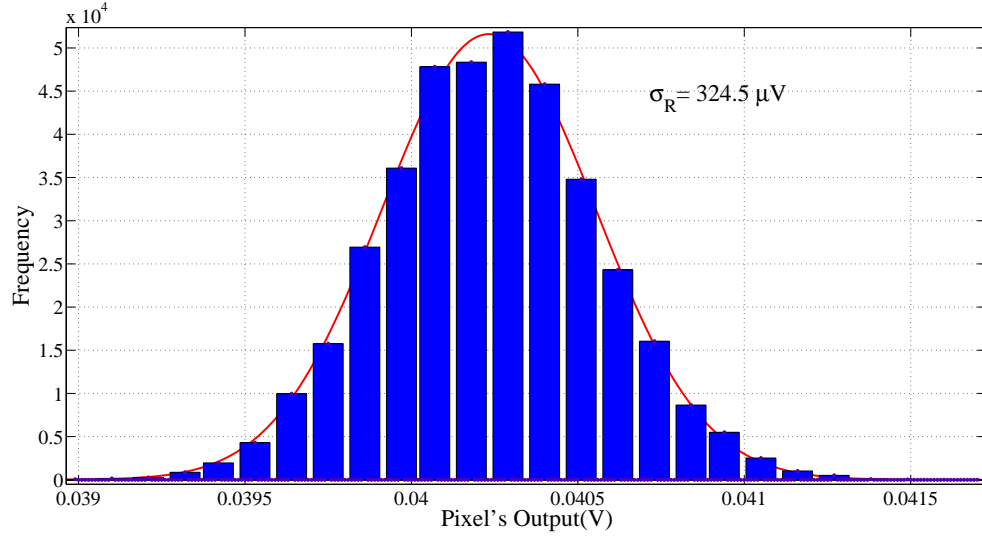


Figure 6.10: Histogram of measured single pixel output under dark conditions and short integration time.

6.3.6 Dynamic range

The dynamic range describes the ability of a sensor to image highlights and shadows and is defined as the ratio of the largest non-saturating current to the smallest detectable current signal. This parameter can be obtained as [59]:

$$DR = 20 \log \frac{q_{max} - i_{dark}t_{int}}{\sqrt{\sigma_r^2 + qi_{dark}t_{int}}}. \quad (6.13)$$

Where q_{max} is the sensor's charge well capacity, i_{dark} the dark current, t_{int} the integration time and σ_r^2 is the variance of the temporal read noise. In order to estimate the dynamic range, the well capacity is obtained as $q_{max} = C_{pd}V_{sat}$, where the capacitance is $C_{pd} = q/CG$ and V_{sat} is the full-well saturation voltage. The measurement is done for an integration time of $t_{int} = 8.32 \text{ ms}$. The dynamic range is then calculated at $DR = 62.2 \text{ dB}$.

6.3.7 Signal-to-noise-ratio

The SNR is the ratio of input referred signal to the input referred noise at a given illumination level. At high illumination, shot noise is the dominant source of noise, while the read noise dominates under low illumination conditions. As a function of the photocurrent (i_{ph}), the SNR is given by [59]:

$$SNR = 20 \log \frac{i_{ph} t_{int}}{\sqrt{\sigma_r^2 + q(i_{ph} + i_{dark}) t_{int}}}. \quad (6.14)$$

The estimation of the SNR is done by, under constant illumination, changing the integration time, which in turn produces a change in the differential output. From where the incident photocurrent is then estimated from equation 5.31. Figure 6.11 shows the measured SNR as a function of the imager's output, observing a maximum value at saturation voltage of $SNR = 49.5$ dB.

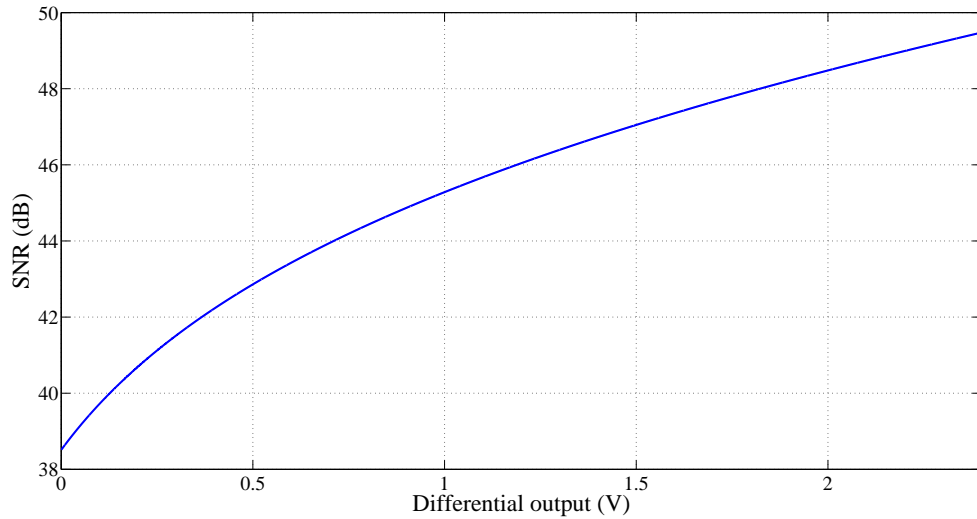


Figure 6.11: Measured SNR variation with differential output

6.3.8 CMOS-ACS performance characteristics summary

Table 6.1 summarizes the obtained performance characteristics:

Table 6.1: Measured CMOS-ACS performance characteristics

Conversion Gain gain	$7.3 \mu\text{V}/e^-$
Full-well saturation	$118.8 \times 10^3 e^-$
Dark current density	$0.014 \text{ fA}/\mu\text{m}^2$
Sensitivity	$0.26 \text{ V}/\text{Lux}\cdot\text{s}$
DSNU	0.03%
Pixel FPN	0.09%
Column FPN	0.06%
Read noise	$45 e^-$
Dynamic range	62.2 dB
SNR (at 2.4 V)	49.5 dB

6.4 CMOS-ACS in SPR biosensing platform

In chapter 4 the intensity profile of the reflected light under different conditions is presented. Not considering losses from other optical elements in the light's path, for the prism with refractive index $n_p = 1.55$, approximately 90% of the light is reflected when the resonance conditions has not been achieved and when the incidence angle is 68.45° the reflectivity falls to 0.81% (figure 4.2e). These minimum and maximum values represent a dynamic range for the SPR signal of 20.4 dB, which from the value of 62.2 dB for the dynamic range (table 6.1) the image sensor is able to cover.

For the prism with refractive index $n_p = 1.46$, the strong SPR coupling results in a maximum reflectivity of 90% and a minimum reflectivity of only 0.01% at the resonance angle (figure 4.3d), resulting in a dynamic range of the SPR output signal of 39.5 dB, which the CMOS imager is also able to fully detect.

On the other hand, COMSOL simulations indicate that for a change of 10^{-4} in the dielectric refractive index, a change of 0.08% in the reflectivity is expected. It is desired to relate this change to the minimum detected value given by the read noise, estimated as $324.5 \mu\text{V}$. Assuming from equation 5.31 that the minimum photocurrent detectable by the sensor's is $I_{ph} = 0.7 \text{ pA}$, a value larger than the estimated dark current $I_{dark} = 3.42 \text{ fA}$. The minimum resolvable incident power can be obtained from:

$$P_0 = \frac{hc}{\eta q \lambda} I_{ph} \quad (6.15)$$

Where η is the photodetector's quantum efficiency. The determination of this parameter consists in the evaluation of the photosensor's response at a given wavelength range. The control of the light source's wavelength must be carefully performed, usually requiring a monochromator to filter the desired wavelength. In the absence of such device, a first approximation of the sensor's quantum efficiency is made by taking as

value the reported quantum efficiency of similar CMOS imagers, placing this quantum efficiency at $\sim 30\%$ from 600 to 700 nm [26, 31, 60]. From where it follows that the minimum detectable incident power is $P_0 = 4.3$ pW. Thus in order to detect the 0.08% change in the reflectivity an incident power larger than this value is required.

A biosensor based on SPR imaging will take advantage of the designed CMOS-ACS where a high dynamic range and contrast is essential to the correct operation of the device. Furthermore, the windowing characteristics of the CMOS-ACS will provide the capability to select a desired area of interest in the SPR microarray under analysis.

6.5 Conclusions

In this chapter the characterization of the CMOS-ACS prototype was performed. The selection of an n-well/p-sub photodiode resulted in a conversion gain of $7.3 \mu\text{V}/e^-$. For the dark current, a significant difference exist between the estimated dark current with the experimental array and the Silvaco model of the photodiode. However, the experimental result is confirmed through an electrical cadence simulation. For the obtained dark current density of $J_{dark} = 0.014 \text{ fA}/\mu\text{m}^2$ at the moment is not anticipated to be an issue.

The results for the FPN are encouraging, at 0.09% of well capacity for the pixel FPN this value indicates the benefit of implementing a pixel with ACS, where the gain variations due to the pixel SF where significantly reduced. In addition the 0.06% of well capacity for the column level FPN shows the benefits of using NCDS and DDS reading, in order to reduce the dispersion in the column signal path. The read noise level is at an acceptable level considering the contributions from sources along the signal path, including the ADC conversion and test card processing. The dynamic range of 62.2 dB, furthermore shows the benefits of ACS, where in principle the CMOS imager is expected to detect the reflected light's profile associated with the presence of SPR.

Chapter 7

Conclusions

This thesis has presented the design, implementation and characterization of a 32×32 -pixel CMOS-ACS imager for use in SPR-based integrated biosensors. First, the operating conditions in a CMOS/post-CMOS compatible SPR-interface were modelled in COMSOL. The model has assumed a Kretschmann prism excitation and a gold-water interface. It was found that for prisms of silicon dioxide with refractive indexes of 1.55 and 1.46, the optimal plasmon coupling is obtained with gold thicknesses of 50 and 45 nm respectively. For the prism of refractive index of 1.55, only 0.81% of the incident light's energy is reflected at resonance, indicating a transfer of the incident wave energy of 99.19% to the surface plasmon propagating in the interface. For a prism refractive index of 1.46, 0.01% of the incident light is reflected at resonance, thus practically all of the light's energy, 99.99%, is transferred to the surface plasmon. The incidence angles at which SPR occurs for refractive indexes of 1.55 and 1.46, are 68.45° and 79.05° respectively, for light's wavelength of 633 nm.

Also, with a COMSOL simulation it was found that a change of 10^{-4} RIU in the refractive index of the dielectric medium, produces a change of 0.01° in the plasmon resonance angle, which in turn produces a change of 0.08% in the reflectivity. The detector will be able to detect this change, provided that the light source is selected in a way that the change in reflectivity is larger than 4.3 pW, based on the read noise level of $324.5 \mu\text{V}$.

Finally, selecting a titanium adhesion layer of 5 nm, the COMSOL model produced an increase of 3.2% in the reflectivity at resonance of the prism with refractive index of 1.46 and an increase of 2.8% in the reflectivity for the prism with refractive index of 1.55. This effect reduces slightly the dynamic range of the images in the photodetector.

The results obtained from COMSOL modeling establish some design requirements for the CMOS imager. Additionally, they are also required for the eventual implementation of the SPR-biosensing platform. Furthermore, even though the results presented in this work correspond to a gold-water interface, the implemented model in COMSOL can be easily configured to find optimal conditions for plasmon coupling in interfaces built with other materials.

The imager's pixel is based on a n-well/p-substrate photodiode due to its low junction capacitance. With electrical simulations the value of this capacitance was obtained as 31 fF, in comparison to the higher value of 135 fF for a n-diff/p-substrate photodiode. Experimentally, this value is in good agreement with the estimated value of 21.9 fF, obtained through the measurement of the conversion gain of $7.3 \mu\text{V}/e^-$. This conversion value is desired to be high due to the low illumination conditions expected on biosensor devices, where incident powers in the range of μW - mW can be expected. With a 3-T pixel configuration, the CMOS imager pixel achieves a relatively high fill-factor of 61% increasing the sensitivity of the device, estimated in this case at 0.26 V/Lux·s.

The pixel was based on an Active Column Sensor configuration, with the purpose of reducing the pixel FPN. Furthermore, the negative voltage shift associated with a NMOS source follower is eliminated resulting in an higher output swing and dynamic range. The designed sensor has a full-well saturation voltage of 2.4 V, which can be eventually increased by boosting the reset voltage. The dynamic range of 62.2 dB, permits the detection of the maximum and minimum levels of incident power expected from the reflecting SPR interfaces, where dynamic ranges of 20.4 dB and 39.5 dB are expected for coupling prisms with refractive indexes of 1.55 and 1.46, respectively.

Complementing the ACS configuration, the CMOS image sensors incorporates column-FPN reduction readout circuits, by implementing NCDS and DDS. These techniques don't require extra transistors inside the pixel or additional memory and thus don't reduce the fill factor or increase the chip's area. Additionally, DDS further reduces column FPN and signal dispersion. By taking the differential NCDS-DDS output, the circuit was able to achieve a low pixel and column FPN of 0.09% and 0.06% respectively. This is an acceptable level of FPN noise, since it is lower than the human eye perception of 0.5% of the saturation level [26].

The CMOS-ACS operates with a custom-made test card providing the digital control pulses with a FPGA, which gives the flexibility to modify the integration time. This change can be done by changing the duration time of the digital signals or by selecting a sub-section of the pixel array, taking advantage of one of the particular characteristics of CMOS image sensors: windowing. The test card also performs the subtraction operation of the reset and signal outputs and digitize them through a 16-bit ADC.

7.1 Future work

7.1.1 Experimental set-up

Using the results of the SPR simulations obtained in chapter 4, a biosensing platform will be implemented with all of the elements of a SPR-biosensor, including the designed CMOS imager. A first set-up that will be used to perform SPR spectroscopy with angular modulation is shown in figure 7.1. In it, the incidence angle will be controlled with a resonant scanner fabricated with CMOS-MEMS technology, developed by the BioMEMS research group at ITESM [61]. This device performs angular modulation by

sweeping the incidence angle. A telecentric $f - \theta$ lens is used to create a flat imaging field in the 32×32 -pixel CMOS-ACS imager, with the change in height being equal to $y = f\theta$, where θ is the incidence angle at the lens and f is the focal distance.

Supposing a reflecting prism with an isosceles triangle profile with $\alpha = 100^\circ$, the incident angle at the prism and transmitted angle out of the prism are equal, and related to the incident angle at the SPR interface as:

$$\theta_{t2} = \sin^{-1} \left[\frac{n_d}{n_{air}} \sin \left(\theta_{iSPR} + \frac{\alpha - \pi}{2} \right) \right]. \quad (7.1)$$

The angle of incidence at the lens is given by:

$$\theta = \frac{5\pi}{18} - \theta_{t2}. \quad (7.2)$$

From the previous equation and taking the results from table 4.2, the changes of 0.01° in the SPR angle position result in an average change of 0.02° in the incident angle at the $f - \theta$ lens. With a pixel's pitch of $20 \mu\text{m}$ it is required a lens with focal length of:

$$f = \frac{y}{\theta} = \frac{20 \mu\text{m}}{0.35 \text{ mrad}} = 57.3 \text{ mm} \quad (7.3)$$

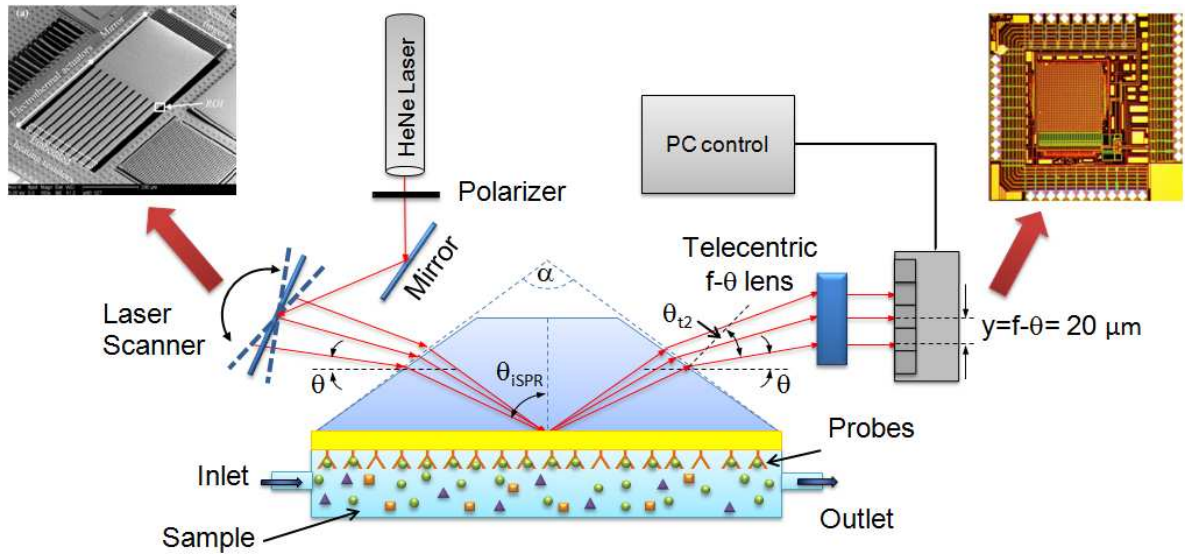


Figure 7.1: Proposed biosensing platform to perform SPR angular modulation.

The proposed set-up shown in figure 7.2 will be used to perform SPR imaging, where instead of focusing the beam at one spot, the diverging laser beam is collimated in order to cover a larger area in the biosensing surface. In this case, the laser scanner remains constant at 79.05° to excite SPR according to the COMSOL simulations.

The resulting output beam reaches the CMOS-ACS imager, producing a 2D image of the intensity profile. First a reference image is obtained at SPR conditions before

the sample introduction. Since the light arrives at the SPR angle, the spots where probes were immobilized are observed at the CMOS imager as dark spots. When the sample is introduced the intensity profile from the image changes, thus increasing the amount of reflected light to the CMOS imager. The concentration levels is estimated by subtracting the two images.

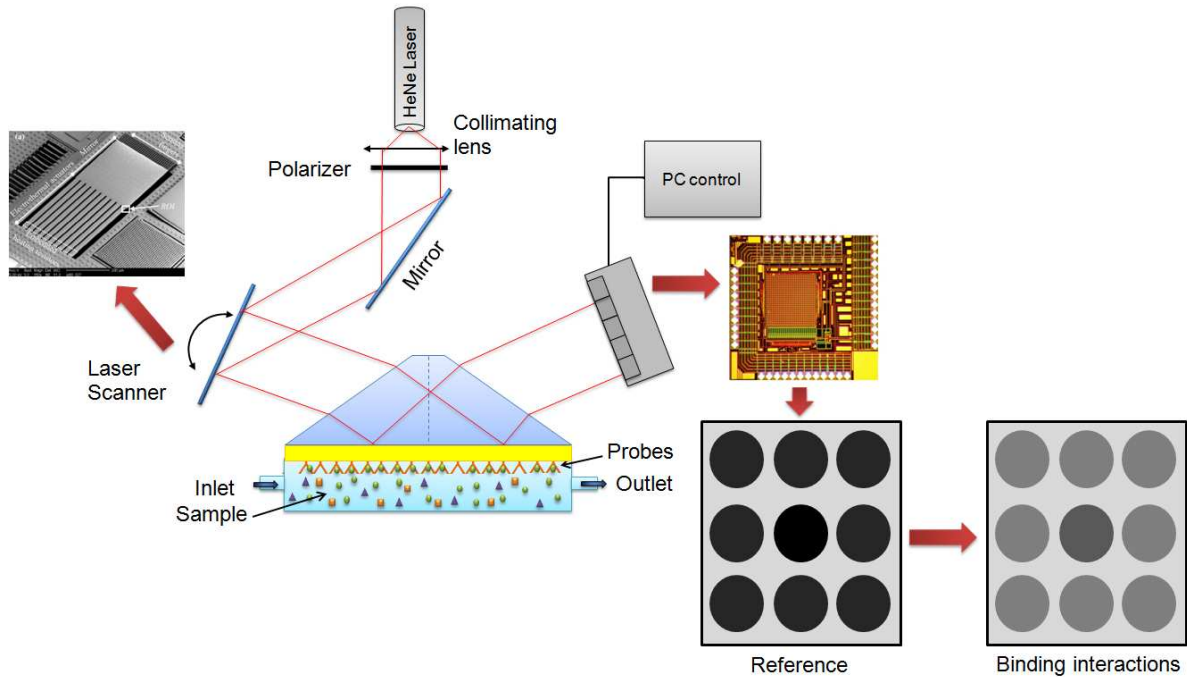


Figure 7.2: Proposed biosensing platform to perform SPR imaging.

7.1.2 Improvement to the CMOS-Imager

Additionally, the designed CMOS-ACS imager can be improved. First, the difference between the Silvaco photodiode model and the measured experimental data must be investigated, verifying the correct parameters according to the technology.

A second prototype and test card with additional characteristics will also be beneficial in improving the performance of the SPR application, some desired new features are:

- Add test modes and probes to facilitate characterization.
- Improve physical layout configuration of test card to facilitate the placement of the CMOS-ACS in a SPR-biosensing experimental array.
- Increase the resolution of the CMOS-ACS by increasing the number of pixels.
- Incorporation of advance reset techniques in order to reduce reset noise.

- Explore the option of the use of pixels with integrated ADC in order to directly obtain the digital output.
- Explore the possibility of column-parallel readout to increase speed.

Finally, at the long term, the work presented in this thesis is a first step towards the goal of developing a fully integrated SPR-biosensing platform incorporating light source, SPR interface, microfluidic channel, optical elements and CMOS imager.

Bibliography

- [1] S. Ray, G. Mehta, and S. Srivastava. “Label-free detection techniques for protein microarrays: Prospects, merits and challenges”. In: *Proteomics* 10.4 (2010), pp. 731–748.
- [2] B. Liedberg, C. Nylander, and I. Lundström. “Biosensing with surface plasmon resonance how it all started”. In: *Biosensors and Bioelectronics* 10.8 (1995), pp. i–ix.
- [3] T. Endo, K. Kerman, N. Nagatani, Y. Morita, Y. Takamura, and E. Tamiya. “Localized surface plasmon resonance based label-free optical biosensor for monitoring peptide nucleic acid-DNA hybridization”. In: vol. 1. 5th IEEE Conference on Nanotechnology. IEEE. 2005, pp. 332–335.
- [4] G. Krishnamoorthy, E.T. Carlen, J.G. Bomer, D. Wijnperlé, H.L. deBoer, A. van den Berg, and R.B.M. Schasfoort. “Electrokinetic label-free screening chip: a marriage of multiplexing and high throughput analysis using surface plasmon resonance imaging”. In: *Lab on a Chip* 10.8 (2010), pp. 986–990.
- [5] A.J. Thiel, A.G. Frutos, C.E. Jordan, M. Robert, and L.M. Smith. “In situ surface plasmon resonance imaging detection of DNA hybridization to oligonucleotide arrays on gold surfaces”. In: *Analytical Chemistry* 69.24 (1997), pp. 4948–4956.
- [6] B.J. Yakes, E. Papafragkou, S.M. Conrad, J.D. Neill, J.F. Ridpath, W. Burkhardt III, M. Kulka, and S.L. DeGrasse. “Surface plasmon resonance biosensor for detection of feline calicivirus, a surrogate for norovirus”. In: *International journal of food microbiology* (2013).
- [7] K. Pimková, M. Bocková, K. Hegnerová, J. Suttner, J. Čermák, J. Homola, and J.E. Dyr. “Surface plasmon resonance biosensor for the detection of VEGFR-1a protein marker of myelodysplastic syndromes”. In: *Analytical and Bioanalytical Chemistry* 402.1 (2012), pp. 381–387.
- [8] G. Koklu, J. Ghaye, R. Beuchat, G. De Micheli, Y. Leblebici, and S. Carrara. “Quantitative comparison of commercial CCD and custom-designed CMOS camera for biological applications”. In: *2012 IEEE International Symposium on Circuits and Systems (ISCAS)*. IEEE. 2012, pp. 2063–2066.
- [9] H.A. Joung, D.G. Hong, and M.G. Kim. “A high sensitivity chemiluminescence based CMOS image biosensor for the detection of human interleukin 5 (IL-5)”. In: *2012 IEEE Sensors*. IEEE. 2012, pp. 1–3.

- [10] D. Litwiller. “CCD vs. CMOS”. In: *Photonics Spectra* 35.1 (2001), pp. 154–158.
- [11] E. Ghafar-Zadeh, M. Sawan, and D. Therriault. “A 0.18- μm CMOS capacitive sensor Lab-on-Chip”. In: *Sensors and Actuators A: Physical* 141.2 (2008), pp. 454–462.
- [12] J. Homola. *Surface plasmon resonance based sensors*. Vol. 4. Springer, 2006.
- [13] P. Tabeling. *Introduction to microfluidics*. OUP Oxford, 2005.
- [14] E. Ouellet, C. Lausted, T. Lin, C.W.T. Yang, L. Hood, and E.T. Lagally. “Parallel microfluidic surface plasmon resonance imaging arrays”. In: *Lab on a Chip* 10.5 (2010), pp. 581–588.
- [15] R.B.M. Schasfoort and A.J. Tudos. *Handbook of surface plasmon resonance*. Royal Society of Chemistry Cambridge, UK, 2008.
- [16] B.A. Sexton, B.N. Feltis, and T.J. Davis. “Characterisation of gold surface plasmon resonance sensor substrates”. In: *Sensors and Actuators A: Physical* 141.2 (2008), pp. 471–475.
- [17] J. Homola. “Surface plasmon resonance sensors for detection of chemical and biological species”. In: *Chemical reviews* 108.2 (2008), p. 462.
- [18] G. Krishnamoorthy, E.T. Carlen, A. van den Berg, and R.B.M. Schasfoort. “Surface plasmon resonance imaging based multiplex biosensor: Integration of biomolecular screening, detection and kinetics estimation”. In: *Sensors and Actuators B: Chemical* 148.2 (2010), pp. 511–521.
- [19] S. Scarano, M. Mascini, A.P.F. Turner, and M. Minunni. “Surface plasmon resonance imaging for affinity-based biosensors”. In: *Biosensors and bioelectronics* 25.5 (2010), pp. 957–966.
- [20] S.A. Maier. *Plasmonics: fundamentals and applications*. Springer, 2007.
- [21] H. Raether. *Surface plasmons on smooth surfaces*. Springer, 1988.
- [22] B.E.A. Saleh, M.C. Teich, and B.E. Saleh. *Fundamentals of photonics*. Vol. 22. Wiley New York, 1991.
- [23] J. Ohta. *Smart CMOS image sensors and applications*. Vol. 129. CRC, 2007.
- [24] P.E. Allen and D.R. Holberg. *CMOS analog circuit design*. Holt, Rinehart and Winston New York, 1987.
- [25] K. Murari, R. Etienne-Cummings, N. Thakor, and G. Cauwenberghs. “Which photodiode to use: A comparison of cmos-compatible structures”. In: *IEEE Sensors Journal* 9.7 (2009), pp. 752–760.
- [26] S.U. Ay. *Large Format CMOS Image Sensors: Performance and Design*. VDM Publishing, 2008.
- [27] B.A. Fowler, M. Godfrey, J. Balicki, and J. Canfield. “Low-noise readout using active reset for CMOS APS”. In: *Electronic Imaging*. International Society for Optics and Photonics. 2000, pp. 126–135.

- [28] B. Pain, G. Yang, T.J. Cunningham, C. Wrigley, and B. Hancock. “An enhanced-performance CMOS imager with a flushed-reset photodiode pixel”. In: *IEEE Transactions on Electron Devices* 50.1 (2003), pp. 48–56.
- [29] J. Goy. “Etude, conception, et réalisation d’un capteur d’image APS en technologie standard CMOS pour des applications faible flux de type viseur d’étoiles”. PhD thesis. Institut National Polytechnique de Grenoble, 1992.
- [30] A. El Gamal, B.A. Fowler, H. Min, and X. Liu. “Modeling and estimation of FPN components in CMOS image sensors”. In: *Photonics West’98 Electronic Imaging*. International Society for Optics and Photonics. 1998, pp. 168–177.
- [31] T. Tam. “A CMOS active pixel sensor contact imager for cell detection in biosensing applications”. PhD thesis. University of Calgary, 2010.
- [32] J. Nakamura. *Image sensors and signal processing for digital still cameras*. CRC, 2005.
- [33] AMS. “0.35 um CMOS C35 Process Parameters”. In: *Eng 182 Rev 6.0, austriamicrosystems* (2008).
- [34] Z. Zhou, B. Pain, and E.R. Fossum. “Frame-transfer CMOS active pixel sensor with pixel binning”. In: *IEEE Transactions on Electron Devices* 44.10 (1997), pp. 1764–1768.
- [35] M.E. Dolega, C. Allier, S. Vinjimore-Kesavan, S. Gerbaud, F. Kermarrec, P. Marcoux, J.M. Dinten, X. Gidrol, and N. Picollet-DHahana. “Label-free analysis of prostate acini-like 3D structures by lensfree imaging”. In: *Biosensors and Bioelectronics* (2013).
- [36] D. Ho, M.O. Noor, U.J. Krull, G. Gulak, and R. Genov. “CMOS Tunable-Color Image Sensor With Dual-ADC Shot-Noise-Aware Dynamic Range Extension”. In: *IEEE Transactions on Circuits and Systems I: Regular papers* (2013).
- [37] A. Osman, J.H. Park, D. Dickensheets, J. Platisa, E. Culurciello, and V.A. Pieribone. “Design Constraints for Mobile, High-Speed Fluorescence Brain Imaging in Awake Animals”. In: *IEEE Transactions on Circuits and Systems* 6.5 (2012), pp. 446–453.
- [38] R.R. Singh, L. Leng, A. Guenther, and R. Genov. “A CMOS-Microfluidic Chemiluminescence Contact Imaging Microsystem”. In: *IEEE Journal of Solid-State Circuits* 47.11 (2012), pp. 2822–2833.
- [39] D.S. Daivasagaya, L. Yao, K.Y. Yung, M. Hajj-Hassan, M.C. Cheung, V.P. Chodavarapu, and F.V. Bright. “Contact CMOS imaging of gaseous oxygen sensor array”. In: *Sensors and Actuators B: Chemical* 157.2 (2011), pp. 408–416.
- [40] L. Yao, K.Y. Yung, V.P. Chodavarapu, and F.V. Bright. “CMOS imaging of temperature effects on pin-printed xerogel sensor microarrays”. In: *IEEE Transactions on Biomedical Circuits and Systems* 5.2 (2011), pp. 189–196.
- [41] Y.B. Shin, H.M. Kim, Y. Jung, and B.H. Chung. “A new palm-sized surface plasmon resonance (SPR) biosensor based on modulation of a light source by a rotating mirror”. In: *Sensors and Actuators B: Chemical* 150.1 (2010), pp. 1–6.

- [42] N.S. Johnston, R.A. Light, C.E. Stewart, M.G. Somekh, and M.C. Pitter. “CMOS modulated light cameras for sensitive surface plasmon resonance imaging”. In: *BiOS*. International Society for Optics and Photonics. 2010, 75770H–75770H.
- [43] COMSOL. *COMSOL Multiphysics*. www.comsol.com/products/multiphysics. 2008.
- [44] Y. Yang and P. Altermatt. “Simulation of optical properties of the Si/SiO₂/Al interface at the rear of industrially fabricated Si solar cells”. In: Proceedings of the COMSOL Conference. 2008.
- [45] G. Ghosh. “Dispersion-equation coefficients for the refractive index and birefringence of calcite and quartz crystals”. In: *Optics Communications* 163.1 (1999), pp. 95–102.
- [46] M. Bass, C. DeCusatis, J. Enoch, V. Lakshminarayanan, G. Li, C. MacDonald, V. Mahajan, and E. Van Stryland. *Handbook of optics, volume IV*. third. McGraw-Hill, 2009.
- [47] Y. Huang, A. Mason, A.J. Greiner, R.Y. Ofoli, and R.M. Worden. “Post-CMOS Compatible Microfabrication of a Multi-Analyte Bioelectrochemical Sensor Array Microsystem”. In: *2006. 5th IEEE Conference on Sensors*. IEEE. 2006, pp. 612–615.
- [48] P. Johnson and R. Christy. “Optical constants of the noble metals”. In: *Phys. Rev. B* 6.12 (1972), 43704379.
- [49] J. Rhee, D. Wang, N.J. Tao, and Y. Joo. “CMOS image sensor array for surface plasmon resonance spectroscopy”. In: *Society of Photo-Optical Instrumentation Engineers (SPIE) Conference Series*. Vol. 5301. 2004, pp. 34–41.
- [50] Silvaco Int. “Manual, ATLAS Users”. In: *Santa Clara, CA* (2006).
- [51] S.M. Sze and K.K. Ng. *Physics of semiconductor devices*. Wiley-interscience, 2006.
- [52] S. Diller, A. Fish, and O. Yadid-Pecht. “Advanced output chains for CMOS image sensors based on an active column sensor approach a detailed comparison”. In: *Sensors and Actuators A: Physical* 116.2 (2004), pp. 304–311.
- [53] D.A. Johns and K. Martin. *Analog integrated circuit design*. Wiley. com, 2008.
- [54] F. Dadouche, A. Alexandre, B. Granado, A. Pinna, and P. Garda. “A VHDL-AMS spectral model of photodetectors for active pixel sensors”. In: *Forum on Specification and Design Languages*. 2002, pp. 24–27.
- [55] R.H. Nixon, S.E. Kemeny, C.O. Staller, and E.R. Fossum. “128 x 128 CMOS photodiode-type active pixel sensor with on-chip timing, control, and signal chain electronics”. In: *IS&T/SPIE’s Symposium on Electronic Imaging: Science & Technology*. International Society for Optics and Photonics. 1995, pp. 117–123.
- [56] R.H. Nixon, S.E. Kemeny, B. Pain, C.O. Staller, and E.R. Fossum. “256 × 256 CMOS active pixel sensor camera-on-a-chip”. In: *IEEE Journal of Solid-State Circuits* 31.12 (1996), pp. 2046–2050.

- [57] B.P. Beecken and E.R. Fossum. “Determination of the conversion gain and the accuracy of its measurement for detector elements and arrays”. In: *Applied optics* 35.19 (1996), pp. 3471–3477.
- [58] D.J. Roulston, N.D. Arora, and S.G. Chamberlain. “Modeling and measurement of minority-carrier lifetime versus doping in diffused layers of n_i sup_i+i/sup_i-p silicon diodes”. In: *IEEE Transactions on Electron Devices* 29.2 (1982), pp. 284–291.
- [59] T. Chen, P.B. Catrysse, A. El Gamal, and B.A. Wandell. “How small should pixel size be?” In: *Electronic Imaging*. International Society for Optics and Photonics. 2000, pp. 451–459.
- [60] *Spectral response of silicon image sensors*. white paper. www.aphesa.com. 2009.
- [61] S. Camacho-León, P.J. Gilgunn, S.O. Martínez-Chapa, and G.K. Fedder. “A high-speed, bimodal, CMOS-MEMS resonant scanner driven by temperature-gradient actuators”. In: *SPIE MOEMS-MEMS*. International Society for Optics and Photonics. 2012, pp. 82520V–82520V.

Appendix A

Appendix A

A.1 Analysis of propagation of surface plasmons with Maxwell's equations

Starting from the fundamental Maxwell's equations:

$$\nabla \cdot \mathbf{D} = \rho, \quad (\text{A.1a})$$

$$\nabla \cdot \mathbf{B} = 0, \quad (\text{A.1b})$$

$$\nabla \times \mathbf{E} = -\frac{\partial \mathbf{B}}{\partial t}, \quad (\text{A.1c})$$

$$\nabla \times \mathbf{H} = \mathbf{J} + \frac{\partial \mathbf{D}}{\partial t}. \quad (\text{A.1d})$$

Where \mathbf{D} is the electric flux density, \mathbf{B} is the magnetic flux density, \mathbf{E} is the electric field, \mathbf{H} is the magnetic field, ρ is the charge density and \mathbf{J} is the current density. For linear, isotropic and nonmagnetic materials, the four field are related through the constitutive relations:

$$\mathbf{B} = \mu_0 \mathbf{H}, \quad (\text{A.2})$$

$$\mathbf{D} = \varepsilon_0 \varepsilon_r \mathbf{E}. \quad (\text{A.3})$$

Where $\mu_0 = 4\pi \times 10^{-7}$ H/m is the permeability of free space, $\varepsilon_0 = 8.85419 \times 10^{-12}$ F/m is the free space permittivity and ε_r is the relative permittivity of the material.

The propagation of a surface plasmon can be found by solving equations A.1 for the interface between a dielectric and a metal. Assuming the simpler case with no charges and current densities, combining equations A.1c and A.1d results in:

$$\nabla \times \nabla \times \mathbf{E} = -\frac{\partial}{\partial t}(\nabla \times \mathbf{B}), \quad (\text{A.4})$$

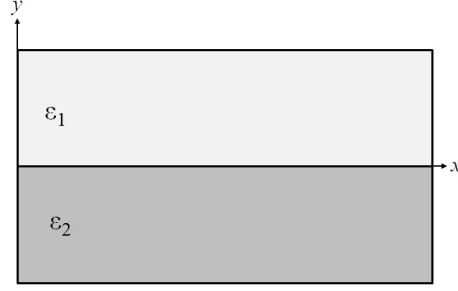


Figure A.1: Geometry of planar waveguide

$$\nabla \times \nabla \times \mathbf{E} = -\mu_0 \frac{\partial^2 \mathbf{D}}{\partial t^2}. \quad (\text{A.5})$$

Using the fact that with no charges $\nabla \cdot \mathbf{D} = 0$ and that,

$$\nabla \times \nabla \times \mathbf{E} = \nabla(\nabla \cdot \mathbf{E}) - \nabla^2 \mathbf{E}, \quad (\text{A.6})$$

$$\nabla \cdot (\varepsilon \mathbf{E}) = \mathbf{E} \cdot \nabla \varepsilon + \varepsilon \nabla \cdot \mathbf{E}. \quad (\text{A.7})$$

Equation A.5 can be expressed as:

$$\nabla \left(-\frac{1}{\varepsilon_r} \mathbf{E} \cdot \nabla \varepsilon \right) - \nabla^2 \mathbf{E} = -\mu_0 \varepsilon_0 \varepsilon_r \frac{\partial^2 \mathbf{E}}{\partial t^2}. \quad (\text{A.8})$$

For an invariant dielectric profile $\nabla \varepsilon = 0$ the wave equation is then given by:

$$\nabla^2 \mathbf{E} - \frac{\varepsilon_r}{c^2} \frac{\partial^2 \mathbf{E}}{\partial t^2} = 0. \quad (\text{A.9})$$

The next step is to solve equation A.9 for the different regions of constant ε and match the solution using the appropriate boundary conditions. For a time harmonic electric field defined as:

$$\mathbf{E}(\mathbf{r}, t) = \mathbf{E}(\mathbf{r}) \exp(-j\omega t). \quad (\text{A.10})$$

Where $\mathbf{r} = x, y, z$ is the position vector and ω is the angular frequency. Substituting A.10 into A.9 and with $k_0 = \omega/c = 2\pi/\lambda$ the known Helmholtz equation is obtained:

$$\nabla^2 \mathbf{E} + k_0^2 \varepsilon_r \mathbf{E} = 0. \quad (\text{A.11})$$

For a wave propagating in the x -axis in a planar waveguide as shown in figure A.1, with the interface at $y = 0$,

$$\mathbf{E}(x, y) = \mathbf{E}(y) \exp(-jk_x x). \quad (\text{A.12})$$

Combining equations A.11 and A.12 results in:

$$\frac{\partial^2 \mathbf{E}(y)}{\partial y^2} + (k_0^2 \varepsilon_r + \beta^2) \mathbf{E} = 0 \quad (\text{A.13})$$

For time harmonic dependence with $\frac{\partial}{\partial t} = -j\omega$, $\frac{\partial}{\partial x} = j\beta$ and $\frac{\partial}{\partial z} = 0$, the following set of equations is obtained:

$$\frac{\partial E_z}{\partial y} = j\omega \mu_0 H_x, \quad (\text{A.14a})$$

$$\frac{\partial E_x}{\partial y} - j\beta E_y = -j\omega\mu_0 H_z, \quad (\text{A.14b})$$

$$j\beta E_z = j\omega\mu_0 H_y, \quad (\text{A.14c})$$

$$\frac{\partial H_z}{\partial y} = -j\omega\varepsilon_0\varepsilon_r E_x, \quad (\text{A.14d})$$

$$\frac{\partial H_x}{\partial y} - j\beta H_y = -j\omega\varepsilon_0\varepsilon_r E_z, \quad (\text{A.14e})$$

$$j\beta H_z = j\omega\varepsilon_0\varepsilon_r E_y. \quad (\text{A.14f})$$

Two sets of solutions can be obtained for this system, transverse magnetic waves (TM-waves or p-polarization) and transverse electric waves (TE-waves or s-polarization). Defining the plane of incidence as the plane xy in figure A.1 for TM-waves only the electric field parallel to the plane of incidence and the magnetic field component perpendicular to the plane of incidence are not zero, that is the only existing fields are E_x , E_y and H_z . For TE-waves the only field components that exist are H_x , H_y and E_z . Solving for TM polarization:

$$E_x = -j \frac{1}{\omega\varepsilon_0\varepsilon_r} \frac{\partial H_z}{\partial y}, \quad (\text{A.15a})$$

$$E_x = -j \frac{\beta}{\omega\varepsilon_0\varepsilon_r} H_z, \quad (\text{A.15b})$$

Finally, arriving at the TM wave equation given by:

$$\frac{\partial^2 H_z}{\partial y^2} + (k_0^2\varepsilon_r - \beta^2)H_z = 0 \quad (\text{A.16})$$

Similarly, for TE waves:

$$\frac{\partial^2 E_z}{\partial y^2} + (k_0^2\varepsilon_r - \beta^2)E_z = 0. \quad (\text{A.17})$$

Going back to figure A.1, with ε_1 being the permittivity of the dielectric layer, ε_2 the permittivity of the metal, and considering equations A.15 and A.16 for $y > 0$:

$$H_z(y) = A_1 \exp(-k_{y,1}y + j\beta x) \quad (\text{A.18a})$$

$$E_x(y) = jA_1 \frac{k_{y,1}}{\omega\varepsilon_0\varepsilon_1} \exp(-k_{y,1}y + j\beta x) \quad (\text{A.18b})$$

$$E_y(y) = -A_1 \frac{\beta}{\omega\varepsilon_0\varepsilon_1} \exp(-k_{y,1}y + j\beta x) \quad (\text{A.18c})$$

for $y < 0$:

$$H_z(y) = A_2 \exp(-k_{y,2}y + j\beta x) \quad (\text{A.19a})$$

$$E_x(y) = jA_2 \frac{k_{y,2}}{\omega\varepsilon_0\varepsilon_2} \exp(-k_{y,2}y + j\beta x) \quad (\text{A.19b})$$

$$E_y(y) = -A_2 \frac{\beta}{\omega\varepsilon_0\varepsilon_2} \exp(-k_{y,1}y + j\beta x) \quad (\text{A.19c})$$

Where $k_{y,1}$ and $k_{y,2}$ are the components of the wave vector perpendicular to the interface. An analysis of the continuity conditions of the electric and magnetic fields at the interface require the amplitudes to be equal ($A_1 = A_2$), this implies that:

$$\frac{k_{y,1}}{k_{y,2}} = -\frac{\varepsilon_1}{\varepsilon_2} \quad (\text{A.20})$$

Following the sign convention used on equations A.18 and A.19 leads to one of the fundamental conditions to achieve surface plasmon resonance, to meet A.20 it is required that $\Re(\varepsilon_2) < 0$ and $\varepsilon_1 > 0$. This condition implies that for an evanescent waves to exist, the two mediums must have permittivity of opposite signs. Metals contain a large number of free electrons resulting in a angular frequency $\omega < \omega_p$, with ε_2 given by [15]:

$$\varepsilon_2(\omega) = 1 - \frac{\omega_p^2}{\omega^2}, \quad (\text{A.21})$$

$$\omega_p^2 = \sqrt{4\pi n_e e^2 / m_e}, \quad (\text{A.22})$$

where ω_p^2 is the plasma frequency, n_e is the free electron density, e is the electron charge and m_e is the electron mass. For $\omega < \omega_p^2$ no wave propagates in the metal, but provided that in a geometry such as figure A.1 with dielectric functions of opposite signs $k_{y,i}$ is imaginary, while k_x remains real. Thus an electromagnetic wave exists, propagating along the interface, with evanescent decay perpendicular to the interface. A similar analysis reveals that surface plasmons aren't possible for TE-waves.

The other fundamental result from equations A.18 and A.19 is the dispersion relation from surface plasmons, where the frequency/wavelength of the light is related to the interface's materials refractive index. By considering that H_z must be a solution of the wave equation for TM polarization A.16:

$$k_{y,1}^2 = \beta^2 - k_0^2 \varepsilon_1, \quad (\text{A.23a})$$

$$k_{y,2}^2 = \beta^2 - k_0^2 \varepsilon_2. \quad (\text{A.23b})$$

Combining this results with equation A.20 the fundamental equation describing the propagation of surface plasmons at a metal dielectric interface is obtained:

$$\beta = k_0 \sqrt{\frac{\varepsilon_1 \varepsilon_2}{\varepsilon_1 + \varepsilon_2}} \quad (\text{A.24})$$

Appendix B

Appendix B

B.1 32x32 CMOS-ACS pinout

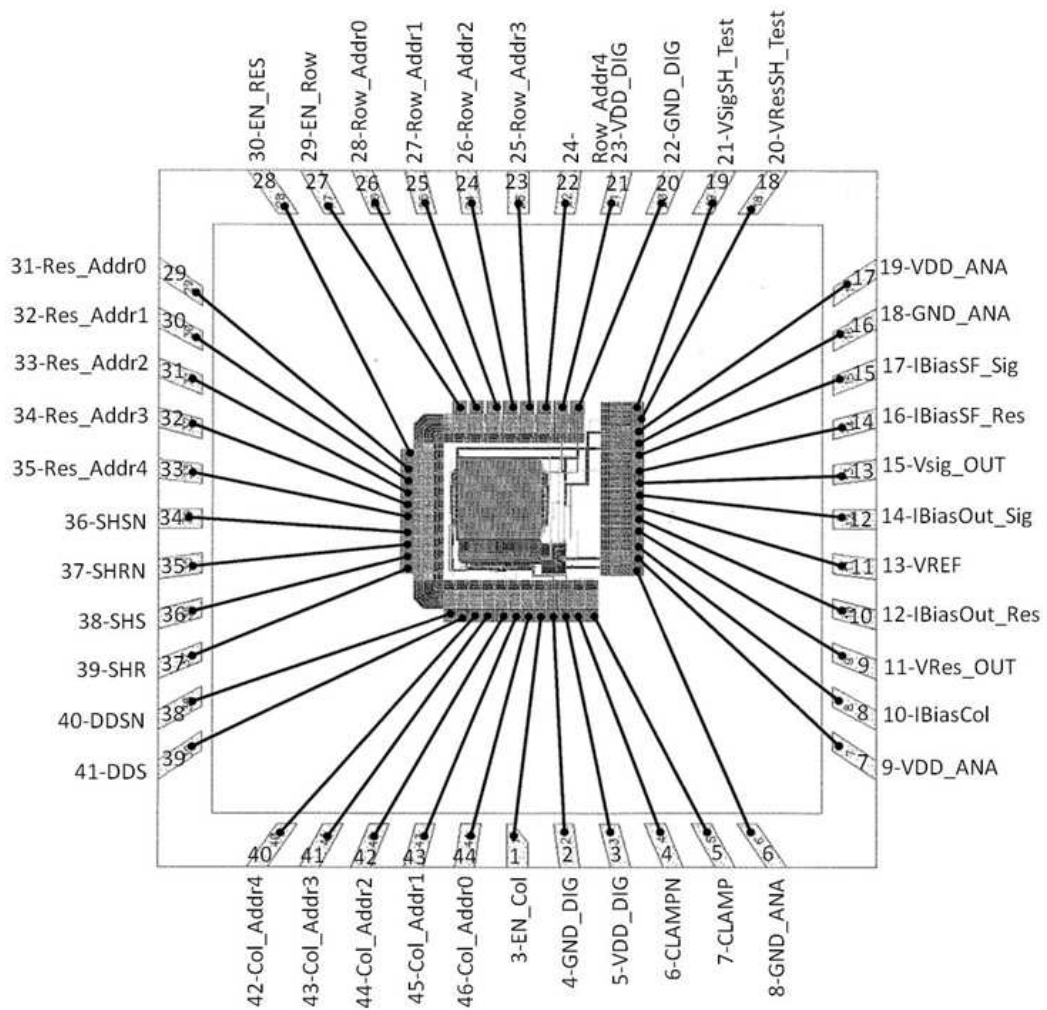


Figure B.1: 32x32 CMOS-ACS pinout.

Table B.1: CMOS-ACS pin description

Pin	Signal	Description
1	EN_COL	Enable column decoder
2	GND_D	Digital ground
3	VDD_D	Digital supply voltage
4	\overline{CLAMP}	Output circuit TG signal
5	CLAMP	Output circuit TG signal
6	GND_A	Analog ground
7	VDD_A	Analog supply voltage
8	BiasCol	Bias current to column Active Column Sensor circuits
9	VRes_OUT	Reset Voltage output
10	BiasOut_res	Bias current of output Op-amp in reset branch
11	Vref	Reference output voltage
12	BiasOut_res	Bias current of output Op-amp in signal branch
13	VSig_OUT	Voltage output after integration time
14	BiasSF_res	Bias column source follower reset branch
15	BiasSF_sig	Bias column source follower signal branch
16	GND_A	Analog ground
17	VDD_A	Analog supply voltage
18	VRes_Test	Reset voltage output of test pixel
19	VSig_Test	Signal voltage output of test pixel
20	GND_D	Digital ground
21	VDD_D	Digital supply voltage
22-26	ROW_ADD(4:0)	Row select address
27	EN_ROW	Enable Row Select decoder
28	EN_RES	Enable Row Reset decoder
29-33	RES_ADD(0:4)	Reset row address
34	\overline{SHS}	Complement sample and hold signal branch
35	\overline{SHR}	Complement sample and hold reset branch
36	SHS	Sample and hold signal branch
37	SHR	Sample and hold reset branch
38	\overline{DDS}	Complement Double Delta Sampling signal
39	DDS	Double Delta Sampling signal
40-44	COL_ADD(4:0)	Column address

Vita

Arnoldo Salazar Soto was born in Sonora, México, on June 9, 1978. He earned the Electronic Systems Engineering degree from ITESM, Monterrey Campus in 2001 and the M.S. in Optoelectronics from CICESE in 2009. He obtained the Ph.D. degree from the ITESM, Monterrey Campus in Information and Communications Technologies and from the Université de Grenoble the Ph.D. degree in Nano-Electronics and Nanotechnology in 2013. He made a research stay in Grenoble, France at the Laboratoire de Physique Subatomique et Cosmologie (LPSC) from September 2011 to October 2012. His research interests are CMOS image sensors, CMOS microelectronics, CMOS-MEMS, plasmonics and optical biosensors.

This doctoral dissertation was typed using L^AT_EX by Arnoldo Salazar Soto.